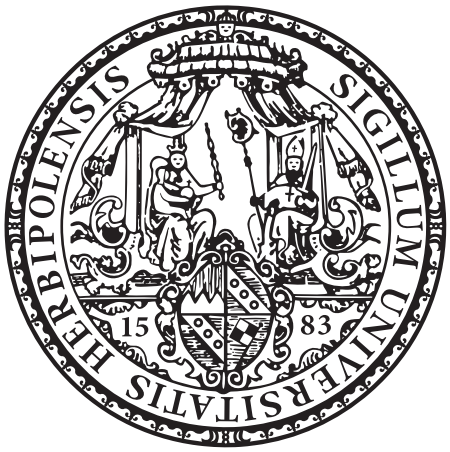

Surface Raman Spectroscopy on Ordered Metal Adsorbates on Semiconductor Substrates and Thin Intermetallic Films

Dissertation zur Erlangung des
naturwissenschaftlichen Doktorgrades
der Julius-Maximilians-Universität Würzburg

vorgelegt von

Benedikt Halbig
aus Bad Pyrmont

Würzburg 2019

Eingereicht am: 13.02.2019
bei der Fakultät für Physik und Astronomie.

1. Gutachter: Prof. Dr. Jean Geurts
2. Gutachter: Prof. Dr. Jörg Schäfer
3. Gutachter:
der Dissertation.

Vorsitzender: Prof. Dr. Björn Trauzettel

1. Prüfer: Prof. Dr. Jean Geurts
2. Prüfer: Prof. Dr. Jörg Schäfer
3. Prüfer: Prof. Dr. Giorgio Sangiovanni
im Promotionskolloquium.

Tag des Promotionskolloquiums: 22.05.2019

Doktorurkunde ausgehändigt am:

Abstract

Surface systems attract great scientific attention due to novel and exotic properties. The atomically structured surfaces lead to a reduced dimensionality which alters electronic correlations, vibrational properties, and their impact on each other. The emerging physical phenomena are not observed for related bulk materials. In this thesis, ordered (sub)monolayers of metal atoms (Au and Sn) on semiconductor substrates (Si(111) and Ge(111)) and ultrathin intermetallic films ($CePt_5$ and $LaPt_5$) on metal substrate (Pt(111)) are investigated by polarized *in situ* surface Raman spectroscopy. The surface Raman spectra exhibit features of specific elementary excitations like surface phonons and electronic excitations, which are suitable to gain fundamental insights into the surface systems.

The Au-induced surface reconstructions (5×2) and ($\sqrt{3} \times \sqrt{3}$) constitute quasi-one- and two-dimensional Au structures on the Si(111) substrate, respectively. The new reconstruction-related Raman peaks are analyzed with respect to their polarization and temperature behavior. The Raman results are combined with first-principles calculations to decide between different proposed structural models. The Au-(5×2)/Si(111) reconstruction is best described by the model of Kwon and Kang, while for Au-($\sqrt{3} \times \sqrt{3}$)/Si(111) the conjugate honeycomb-chained-trimer model is favored. The Sn-induced reconstructions with $\frac{1}{3}$ monolayer on Ge(111) and Si(111) are investigated to reveal their extraordinary temperature behavior. Specific surface phonon modes are identified that are predicted within the dynamical fluctuation model. Contrary to Sn/Si(111), the corresponding vibrational mode of Sn/Ge(111) exhibits a nearly harmonic character. The reversible structural phase transition of Sn/Ge(111) from ($\sqrt{3} \times \sqrt{3}$) to (3×3) is observed, while no phase transition is apparent for Sn/Si(111). Moreover, Raman spectra of the closely related systems Sn-($2\sqrt{3} \times 2\sqrt{3}$)/Si(111) and thin films of α-Sn as well as the clean semiconductor surfaces Si(111)-(7×7) and Ge(111)-c(2×8) are evaluated and compared.

The $CePt_5$/Pt(111) system hosts $4f$ electrons whose energy levels are modified by the crystal field and are relevant for a description of the observed Kondo physics. In contrast, isostructural $LaPt_5$/Pt(111) has no $4f$ electrons. For $CePt_5$/Pt(111), distinct Raman features due to electronic Raman scattering can be unambiguously related to transitions between the crystal-field states which are depth-dependent. This assignment is supported by comparison to $LaPt_5$/Pt(111) and group theoretical considerations. Furthermore, the vibrational properties of $CePt_5$ and $LaPt_5$ reveal interesting similarities but also striking differences like an unusual temperature shift of a vibration mode of $CePt_5$, which is related to the influence of $4f$ electrons.

Zusammenfassung

Oberflächensysteme sind durch ihre neuartigen Eigenschaften von großem wissenschaftlichen Interesse. Die reduzierten Dimensionen atomar-strukturierter Oberflächen ändern elektronische Korrelationen, vibronische Eigenschaften und deren gegenseitige Beeinflussung. Entsprechende physikalische Phänomene sind für Volumensysteme unbekannt. In dieser Arbeit werden geordnete Monolagen von Metallatomen (Au und Sn) auf Halbleitersubstraten (Si(111) und Ge(111)) und dünne intermetallische Filme ($CePt_5$ und $LaPt_5$) auf metallischem Substrat (Pt(111)) durch polarisierte *in situ* Oberflächen-Raman-Spektroskopie untersucht. Die Oberflächen-Raman-Spektren zeigen spezielle elementare Anregungen, wie Oberflächenphononen und elektronische Anregungen, die fundamentale Einsichten gewähren.

Die Au-induzierten Oberflächenrekonstruktionen (5×2) und ($\sqrt{3} \times \sqrt{3}$) bilden jeweils quasi-ein- und zwei-dimensionale Au-Strukturen auf Si(111). Die entstehenden rekonstruktionsbedingten Raman-Peaks werden hinsichtlich ihres Polarisations- und Temperaturverhaltens untersucht. Die Kombination der Raman-Ergebnisse mit *first-principles*-Berechnungen ermöglicht die Unterscheidung zwischen vorgeschlagenen Strukturmodellen. Au-(5×2)/Si(111) wird am besten durch das Modell von Kwon und Kang beschrieben, während für Au-($\sqrt{3}\times\sqrt{3}$)/Si(111) das *conjugate honeycomb-chained-trimer*-Modell bevorzugt wird. Die Sn-induzierten Rekonstruktionen mit $\frac{1}{3}$ Monolage auf Ge(111) und Si(111) werden aufgrund ihres außergewöhnlichen Temperaturverhaltens untersucht. Die durch das *dynamical fluctuation*-Modell vorhergesagten spezifischen Oberflächenphononen werden identifiziert, wobei die entsprechende Vibrationsmode von Sn/Ge(111), im Gegensatz zu Sn/Si(111), nahezu harmonischen Charakter zeigt. Der umkehrbare strukturelle Phasenübergang von ($\sqrt{3} \times \sqrt{3}$) zu (3×3) wird für Sn/Ge(111), jedoch nicht für Sn/Si(111), beobachtet. Außerdem werden Sn-($2\sqrt{3} \times 2\sqrt{3}$)/Si(111) und dünne α-Sn-Filme sowie Si(111)-(7×7) und Ge(111)-c(2×8) untersucht und verglichen.

$CePt_5$/Pt(111) enthält $4f$-Elektronen, deren Energieniveaus sich durch das Kristallfeld ändern und die zur Beschreibung der Kondo-Physik nötig sind. Strukturgleiches $LaPt_5$/Pt(111) hat hingegen keine $4f$-Elektronen. Für $CePt_5$/Pt(111) werden spezifische Raman-Signaturen durch elektronische Raman-Streuung eindeutig identifiziert und Übergängen zwischen tiefenabhängigen Kristallfeldzuständen zugeordnet. Der Vergleich mit $LaPt_5$/Pt(111) und Gruppentheorie stützt die Zuordnung. Die vibronischen Eigenschaften von $CePt_5$ and $LaPt_5$ zeigen neben Gemeinsamkeiten auch Unterschiede wie anormale Temperaturverschiebungen einer $CePt_5$-Vibrationsmode, die auf Wechselwirkungen mit $4f$-Elektronen zurückgehen.

Contents

1. Introduction

Surfaces are inherent consequences of the spatial limitations of real solids. Unlike infinitely extending ideal solids, the boundaries of real solids are adjoined to other phases of matter or vacuum. In this thesis, solids in their crystalline form, their surfaces, and surface modifications are of special interest. Here, these modifications are rearrangements of surface atoms with respect to the bulk lattice order as well as adsorption and intermixing with additional atoms of different species.

For both the bare crystalline surface and its modifications, the physical properties are considerably altered compared to the bulk region. Hence, it is inevitable to include and consider surfaces in experiments and realistic theoretical models in solid-state physics. Besides, selective tuning of physical effects is feasible by manipulation of the surface structure. Due to the confinement of the system to two-dimensional (2D) or even one-dimensional (1D) extensions, correlation effects between electrons gain more relevance at the surface [1]. This affects mobile, itinerant as well as immobile, localized electrons. Moreover, the dynamics of the atoms at the surface are altered with respect to the lattice vibrations of the bulk material. The electron and lattice system are interdependent and can interact via electron-phonon coupling. These circumstances give rise to various new physical effects, e.g., phase transitions, that are weak or suppressed for bulk crystals. Correlation effects and new emergent phenomena can be described by theories dealing with many-body physics [2].

From the experimental point of view, surface science started in the early 1960s [3]. The way was paved by developments in vacuum technology and new surface sensitive experimental techniques and led to a prospering research field. The obtained progress was also transferred to industrial applications. Pursuing the aim of surface utilization, surfaces can be used for special purposes of technological kind. The following examples of (future) prototypical devices are related to the surface systems analyzed in this thesis.

Well-known examples for the general application of surfaces are catalytic reactions. Technologically, an important subgroup of catalysts are materials containing rare-earth elements [4]. For instance, intermetallic compounds of Pt together with Ce and La are discussed as possible catalysts for application in sustainable fuel cells [5]. To reach a high activity of the oxygen reduction reaction, among other things the exact atomic configuration at the surface must be known and ensured (initially after preparation and after use) [6]. With respect to understanding microscopical chemical processes on the surface, it might be also interesting to consider the atomic dynamics.

Beyond recent technological issues for industrial purposes, there are surface systems of monolayers (MLs) of metal atoms adsorbed on semiconductor substrates [7]. A ML is considered as a complete layer of atoms whose thickness equals a single atom height. These adsorbate surfaces as well as the clean surfaces exhibit altered crystal structures to minimize the surface energy. These rearrangements are called surface reconstructions. For a special reconstruction of Au adatoms on Si substrate, a realization of an atomic scale memory was demonstrated [8]. The Au atoms build tracks, i.e., ordered parallel 1D chains, on the substrate through self-assembly. Onto these tracks additional Si atoms can be positioned realizing Boolean states of "0" and "1". The positioning as well as the repositioning process of Si atoms is feasible by scanning tunneling microscopy (STM). Compared to the highest storage densities achieved for magnetic hard discs, the density is increased by a factor of $\approx 2.5 \cdot 10^3$. Although the scanning speed is comparatively slow and the surface is extremely sensitive to contamination, these devices are an interesting contribution for the development of new devices for information storage on the atomic scale.

Adlayers on semiconductors may find a new field of application after prediction that it hosts a topological insulator. A possible realization involves a 2D surface reconstruction of Au atoms on Si substrate that is used as a template for a 2D topological insulator [9]. On top of the Au reconstruction another overlayer of a different species is applied. The layer exhibits insulating properties within the sheet, but the edge states enable dissipation-less electrical current. Moreover, the edge current is spin-polarized as required for spintronics applications. This is of special interest for the Si-based semiconductor industry, which wants to integrate these devices into their current technology [7,9].

For the introduction of applicable devices on atomic scales, like the above mentioned examples, analytic tools to probe the surfaces for quality are required. These techniques must be non-destructive, need to have good spatial resolution, and must be able to distinguish between different arrangements of atoms on the surface. Raman spectroscopy (RS) is an optical technique that meets the above mentioned requirements. If the focus is on surfaces, as it is here, a very sensitive experimental Raman setup in combination with a specialized procedure is needed to reveal the small contributions of the surface in the measured Raman intensity. Accordingly, the term surface Raman spectroscopy (SRS) is coined for this method that is applied in this work.

This thesis comprises the investigation of two main types of surface systems by SRS. These are MLs and sub-MLs of metal adatoms (Au and Sn) on semiconductor substrates (Si(111) and Ge(111)) as well as ultrathin films of rare-earth intermetallic compounds ($CePt_5$ and $LaPt_5$) on metal substrate (Pt(111)). The particular surface adsorbate systems and surface intermetallic systems, that are examined, are compiled in Tab. 1.1.

The aim of this thesis is to unveil the surface vibrational eigenmodes and crystal-

Table 1.1.: Overview over all considered surface systems of this thesis.

Surf. adsorbate systems		Surf. intermetallic systems
Au-ind. surf. reconstr.	Sn-ind. surf. reconstr.	
Au-(5×2)/Si(111)	Sn/Ge(111)	$CePt_5$/Pt(111)
Au-($\sqrt{3} \times \sqrt{3}$)/Si(111)	Sn/Si(111)	$LaPt_5$/Pt(111)
	Sn-($2\sqrt{3} \times 2\sqrt{3}$)/Si(111)	
	α-Sn film	
Clean surfaces: Si(111)-(7×7), Ge(111)-c(2×8)		

field excitations (CFEs) of these surface systems by evaluation of the surface Raman spectra. With this information, several key questions are addressed within the following topics: surface phonon properties including symmetry considerations, surface atomic structural configurations, electronic structure especially crystal field (CF) states, and structural phase transitions. For a comprehensive picture, the results of the Raman analysis are interpreted additionally by involving theoretical predictions and other experimental findings. Hence, this work aims to shed new light on surface systems and contributes to the understanding of their physical properties.

This thesis is organized as follows. Firstly, the concepts of surface phonons, that are observed in both surface systems, and CFs, whose excitations are observed in $CePt_5$, are introduced as detected by SRS. Other physical effects and concepts that are important for individual systems are described further down together with the experimental results. The mechanisms of Raman scattering and group theoretical considerations are explained afterwards, followed by the description of the experimental setup (see Ch. 2). The next chapter is dedicated to the semiconductor substrates with metals adsorbed that generate different reconstructions. For Au on Si(111) substrate, the (5×2) and ($\sqrt{3} \times \sqrt{3}$) reconstructions are investigated with respect to their vibrational properties and compared to first-principle calculations. In the following, samples with $\frac{1}{3}$ ML of Sn adatoms on Si(111) and Ge(111) substrates are observed and compared with existing theoretical and experimental results. Here, special focus is on temperature-dependent transitions of the atomic structure. Additionally, the clean semiconductor surfaces of Si(111) and Ge(111) as well as thicker layers and films of Sn are considered (see Ch. 3). The next chapter deals with thin films of $CePt_5$ and $LaPt_5$ on Pt(111) substrate. By comparison, Raman peaks originating from the CF are identified and their properties are investigated. Also the vibrational properties of both surface systems are studied (see Ch. 4). In the last chapter, a summary and an outlook are given (see Ch. 5).

2. Fundamentals

Initially, necessary fundamentals are provided as basis for the following considerations in this chapter. This includes essential physical phenomena as well as experimental setups, that were used to record the data of this thesis. As a starting point, surface phonons and CFEs as the relevant excitations in the surface systems are introduced.

2.1. Surface phonons

The atomic constituents of a crystal lattice can be displaced from their equilibrium positions, e.g., by thermal activation. These displacements occur in specific regular patterns. The resulting vibrations are quantized and called phonons. In general, bulk materials have $3N$ phonon modes, where N is the number of atoms in the primitive unit cell (UC) [10]. These modes are divided into three acoustical and $3(N-1)$ optical phonon modes. Optical modes exist only for crystals with polyatomic basis. For instance, the semiconductors Si and Ge with two atoms per primitive UC have six phonon modes with three acoustical and optical modes each. The wave-vector dependence of the phonon energy $\hbar\omega(\vec{k})$ ($\hbar$ is the reduced Planck constant, ω is the angular frequency, and $\vec{k}$ is the wave vector) represents the phonon dispersion. At the Γ point ($k = 0\,\text{Å}^{-1}$) of the Brillouin zone (BZ) only the optical phonons have non-vanishing energies. Phonons are considered as quasiparticles with spin $s = 0$ and therefore obey the Bose-Einstein statistics [11].

For phonon wave vectors in high-symmetry directions the branches can be labeled as longitudinal acoustic (LA), transversal acoustic (TA), longitudinal optic (LO), and transversal optic (TO). These phonon branches can be degenerated for special points of the BZ [12]. If two phonon branches are degenerate at a particular point in the BZ the labels are merged, e.g., the longitudinal-transversal optical (LTO) phonon of the semiconductors Si and Ge at the Γ point.

At surfaces, the energies of the phonon modes are altered due to rearrangements of the atomic structures, giving rise to a 2D surface unit cell (SUC). The emerging vibrational modes are denoted as surface phonons. This energy renormalization is mainly due to missing or modified bonds to neighboring atoms. Another reason is the static displacement of atoms in the topmost layers to minimize the required surface energy. A reduction of dangling bonds (DBs), i.e., unsaturated valences of a surface atom, is also achieved by reconstruction of the surface.

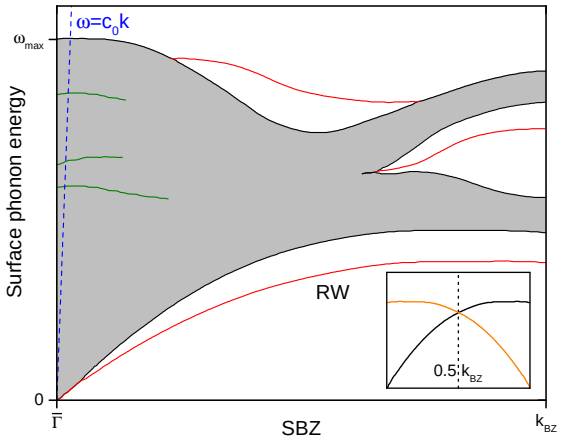

Figure 2.1.: Schematic depiction of a surface phonon dispersion in a 2D SBZ. Green and red lines indicate surface phonons, while the shaded areas are projections of the 3D bulk phonons. The inset shows the backfolding of a RW in case of doubling of the SUC. Data adapted from Ref. [10].

Similar to the BZ of the three-dimensional (3D) crystal, there is a 2D surface Brillouin zone (SBZ) for the surface region. High-symmetry points in the SBZ are marked by a bar on top, i.e., $\bar{\Gamma}$, in contrast to points of the bulk BZ. The phonon dispersion curves of the bulk crystal are projected onto the SBZ as schematically depicted by the shaded area in Fig. 2.1. In the shaded bulk area of the SBZ, gap regions can occur. In these gaps surface phonon modes can occur since they do not couple with bulk modes [10]. If surface phonons and bulk phonons subside, other mechanisms may prevent the surface phonons from fast decay into the bulk. This applies, for instance, for surface phonons at the $\bar{\Gamma}$ point. For the semiconductors Si and Ge, no gaps at the $\bar{\Gamma}$ point appear since the LA and the LO branches touch at the X point of the bulk BZ [13].

If the periodicity of the crystal is changed, this results in an altered UC, which also affects the BZ and gives rise to folding [14]. For instance, by expanding the real space lattice by a multiple, the reciprocal space lattice is shrinked by the inverse. Accordingly, the phonon dispersions are also folded to fit the new BZ. Hence, edges of the original BZ can be folded into the center of the shrinked BZ. This also holds for the SUC and the corresponding SBZ. In the case of acoustical phonons, a nonzero energy at the $\bar{\Gamma}$ point can arise by backfolding as can be seen in the inset of Fig. 2.1.

Rayleigh waves

Near surfaces, there are specific localized waves that are slightly different from the bulk acoustic waves. These waves are called Rayleigh waves (RWs). Their dispersion curves are very similar to bulk acoustic phonons with the difference that the phase velocity of the RW is reduced with respect to the bulk transversal

phase velocity. A RW is shown in Fig. 2.1 below the shaded bulk area. The ratio between both velocities is constant and depends on the material system. The atomic displacements of the RWs decay exponentially with distance from the surface with a damping constant proportional to the wave vector $\vec{k}$ [10,15]. RWs are therefore a sensitive probe for surface reconstructions due to their surface localization [10].

Experimental observation of surface phonons

Phonons located at the surface can be observed by several experimental techniques, apart from SRS [16] used in this thesis and introduced later (see Sec. 2.3.3). Some important and established tools are described briefly (see also, e.g., Refs. [17, 18]). These methods are capable of contributing complementary and additional information to SRS.

Optical measurement techniques, like reflectance anisotropy spectroscopy (RAS) and transmission infrared spectroscopy (TIRS), were successfully applied for the investigation of the vibrational properties of surface systems. In RAS, the sample surface is illuminated by polarized light of varying photon energy [19,20]. The difference between the reflectances for orthogonal polarizations is analyzed. Apart from that, in TIRS light in the infrared (IR) spectral range is used to excite phonon modes [21,22]. The sample needs to be very thin that the light can be transmitted through the sample.

In helium atom scattering (HAS) experiments, He atoms are scattered inelastically on the surface [23–25]. Their energy loss yields the phonon energy. Due to the large momentum transfer, the whole BZ can be scanned. If He atoms are exchanged with electrons or neutrons, the methods work equally and are called high-resolution electron energy loss spectroscopy (HREELS) or inelastic neutron scattering (INS), respectively [26–29]. HAS and HREELS have an energy resolution of $\approx$0.4 and $\approx$1 meV, respectively [30,31].

Theoretical calculation of surface phonons

The complete Hamiltonian of a crystal includes the electrons, the ions of the lattice, as well as their interaction. There are two main approximations to simplify the Hamiltonian which would be virtually unsolvable otherwise.

Calculations are eased by using the Born-Oppenheimer or adiabatic approximation. It states that the electrons in a crystal respond to perturbations much faster than the dynamics of the nuclei of the crystal lattice. This effect is related to the mass difference. It leads effectively to a decoupling of the electron and lattice system and a splitting of the Hamiltonian [32]. The new Hamiltonian for the ions of the lattice includes the impact of the electrons only as an averaged electronic potential [12].

Furthermore, for the theoretical description of lattice vibrations the harmonic approximation is often applied. It neglects terms in the Hamiltonian that are higher than second order. However, in real crystals these higher orders are found, leading to coupling between phonons and to thermal expansion of the crystal lattice [12].

This issue is further discussed in context with anharmonicity.

The theoretical determination of energies and elongation patterns of surface phonons is a demanding task, especially for big UCs containing many atoms. The phonon frequencies $\omega(\vec{k})$ can be determined in the framework of the harmonic approximation by the secular equation [32]:

$$\det \left| D_{ij}^{\alpha\beta}\left(\vec{k}\right) - \omega\left(\vec{k}\right) \right| = 0, \tag{2.1}$$

where $D_{ij}^{\alpha\beta}(\vec{k})$ is the dynamical matrix:

$$D_{ij}^{\alpha\beta}\left(\vec{k}\right) = \frac{1}{\sqrt{m_\alpha m_\beta}} \sum_{\vec{R}_{kl}} C_{ij}^{\alpha\beta}\left(\vec{R}_{kl}\right) e^{-i\vec{k}\cdot\vec{R}_{kl}}. \tag{2.2}$$

In Eq. (2.2), $C_{ij}^{\alpha\beta}(\vec{R}_{kl})$ are the elastic force constants and $\vec{R}_{kl} = \vec{R}_l - \vec{R}_k$ are the interatomic distances. The force constants specify the interaction between different ions and can be obtained by phenomenological models [10,12].

In a microscopic approach, the vibrational properties are usually treated by three different methods: the frozen-phonon technique, the molecular dynamics (MD) simulations, and the linear response formalism [32]. Here, the first two of these first-principles calculations are of special importance. Firstly, structural atomic models are needed as the basis of the calculations. To exclude unwanted effects, the substrate is described by an adequate amount of atomic layers and a saturation of DBs is ensured by H atoms on the back side [33].

According to the frozen-phonon approach, the atoms in the UC are excited so that they move with a distinct displacement pattern. Then, the total energy and the resulting atomic forces of the surface system are investigated and compared to the undistorted system. This facilitates the construction of the dynamical matrix (cf. Eq. (2.2)) [10,32]. With this method also the displacement pattern of the lattice atoms and its symmetry can be asserted [11]. The frozen-phonon results considered in this thesis rely on *ab initio* density-functional theory (DFT) calculations [33,34]. The main idea of DFT is to shift the focus from the wave function to the electron density in the ground state [35]. This density is determined by one-electron wave functions which satisfy the Kohn-Sham equation. To solve this equation several approximations, i.e., for the exchange-correlation (XC) potential, can be introduced. The DFT calculations presented here were performed within the local-density approximation (LDA) [36,37] and the generalized gradient approximation (GGA) (in the Perdew-Burke-Ernzerhof (PBE) formulation) [38,39].

Within MD simulations, a model simulation of the temporal development of the elongation pattern of the atoms, which move about their equilibrium positions, is performed for finite temperatures. Subsequently, the phonon frequencies are found by Fourier transformation of the velocity autocorrelation function [32].

Anharmonicity

Although neglected in the harmonic approximation, phonons cannot be considered as non-interacting particles. This results in phonon-phonon interactions that are enabled by higher-order terms (cubic order or higher) [11]. An effect is the decay of phonons which leads to a finite lifetime. A special case is the decay of an optical phonon at the BZ center into two acoustical phonons [40]. To ensure energy and momentum conservation, the sum of the energies of the acoustical phonons must equal the optical phonon energy and the momenta of the generated phonons need to be opposite. The decay process is accompanied by increasing broadening of the spectral peak with increasing temperature [41]. Through anharmonic effects, the quadratic potential, in which the lattice atoms move, becomes asymmetric giving rise to the already mentioned thermal expansion. The frequency of phonon modes will therefore usually decrease with increasing temperature [41].

2.2. Crystal-field excitations

A free atom or ion has spherical symmetry, i.e., no predominant orientation nor the energy levels of the electrons are altered through external effects in the absence of electric and magnetic fields. This changes if it is embedded into a crystal. Each neighboring atom contributes to a local electric field distribution that is called CF.

In the field-free case, the classification of energy levels of electrons in an atom or ion are based on quantum numbers. These principal quantum numbers are n ($n = 0, 1, 2, 3, \ldots$) for the principal quantum number, l ($0 \leq l \leq n-1$) for the orbital angular momentum quantum number, and s ($s = \frac{1}{2}$) is the spin quantum number. As examples might serve rare-earth elements, which typically have a partly filled $4f$ orbital, i.e., $4f^n$ with $n = 0-13$. A special case is the Ce^{3+} ion which has only one $4f$ electron. For $4f$ electrons, the quantum numbers J and M_J can be regarded as good quantum numbers and stay approximately valid if the ion is placed in a solid [42]. In the framework of the LS or Russel-Saunders coupling the total quantum numbers L and S are obtained by vectorally summing over l and s. The total angular momentum quantum number J results then by spin-orbit coupling (SOC). It is defined as vector sum $J = L + S$ and has $2J + 1$ possible values of M_J ($J \leq M_J \leq -J$, in integer steps), associated with the projection onto the principal axis. Electronic states are labeled by the spectroscopic notation ${}^{2S+1}L_J$, where S, L, and J are the quantum numbers as defined above. The expression $2S + 1$ gives the multiplicity of the system [43].

The CF acts on the energy levels, when the atom or ion is placed in a crystal. For rare-earth ions, it is generally assumed that the SOC outperforms the CF interaction as considered in the weak CF case [43,44]. The former degeneracy regarding M_J can be lifted by the CF. The CF splitting is a Stark splitting in the electric field of the surrounding atoms [43]. The actual characteristics of the splitting depend

largely on the symmetry of the CF. A transition of an electron of a CF state with J and M_J to a state with different J and M_J and higher energy is called CFE. Only certain CFEs are allowed according to selection rules (cf. Sec. 2.4).

Both, SOC and the CF do not break time reversal symmetry. Therefore, for systems with an odd number of electrons the Kramers theorem holds [42,45]. The resulting states are accordingly at least doubly degenerate. Energy levels with equal $\mid M_J \mid$ are energetically degenerate. For twofold Kramers degeneracy the states are called Kramers doublets. In principal, the Kramers doublet can be split by the Zeeman effect by applying an external magnetic field (see for instance Refs. [42,46]).

The influence of the CF on the electronic states is differently near surfaces due to the altered arrangement of the surrounding atoms. This affects the splitting induced by the symmetry of the environment as well as the energy separation between the states.

2.3. Raman scattering

The frequency of light might be changed if it is interacting with matter. The underlying mechanism of inelastic scattering on elementary excitations is named Raman effect. The energy loss or gain of the photon during Raman scattering is analyzed with the optical technique RS. If the frequency of the photon remains unchanged, the process of elastic scattering is called Rayleigh scattering.

The difference in energy $\hbar\omega$ and momentum $\hbar\vec{k}$ (ω is the angular frequency and $\vec{k}$ is the wave vector) between the incident photon ($\hbar\omega_i$, $\hbar\vec{k}_i$) and the scattered photon ($\hbar\omega_s$, $\hbar\vec{k}_s$) is transferred either to or from excitations ($\hbar\Omega_n$, $\hbar\vec{q}_n$) in the sample. These elementary excitations are, e.g., phonons, polaritons, plasmons (and coupled plasmon-phonon modes), single-electron, or hole excitations [47]. In this thesis, especially Raman processes involving phonons and single electron excitations are relevant, labeled vibrational and electronic Raman scattering, respectively. For the Raman scattering process energy as well as quasi-momentum conservation holds [48]:

$$\hbar\omega_s = \hbar\omega_i \pm \hbar\Omega_n, \tag{2.3}$$

$$\hbar\vec{k}_s = \hbar\vec{k}_i \pm \hbar\vec{q}_n. \tag{2.4}$$

The case, where the energy and the momentum of the scattered photon are reduced with respect to the incident photon, is called Stokes process. An excitation is generated. In turn, when the energy and the momentum of the photon are enhanced, an excitation is annihilated and this case is correspondingly named anti-Stokes process. Hence, the "+" and "−" signs in Eqs. (2.3) and (2.4) are attributed to the anti-Stokes and Stokes process, respectively. The Stokes Raman process is investigated in the majority of RS measurements.

Table 2.1.: Relations between commonly used spectroscopic units.

Wavenumber (cm^{-1})	Energy (meV)	Frequency (THz)
1	0.124	0.030
8.066	1	0.242
33.356	4.136	1

The energy $\hbar\Omega_n$ of the excitation in Eq. (2.3) is independent of the incident photon energy. A change of the excitation energy, i.e., a change of the wavelength of the incident laser beam, will not substantially alter the observed Raman spectrum and is therefore a good check if the origin of a peak is Raman scattering (see Sec. D). By this method, Raman signatures can be distinguished from other optical process, e.g., photoluminescence. The Raman measurements are conducted in quasi-backscattering geometry and so the wave vectors in Eq. (2.4) can be reduced to scalars. Since $k_i \approx -k_s$ holds, the transferred momentum $q_n \approx \pm 2k_i$ is quite small for laser lines in the visible spectral range, i.e., $q_n \ll k_{\mathrm{BZ}}$ applies, where k_{BZ} is the wave vector at the boundary of the BZ. Thus, in first-order RS only excitations in the vicinity of the center (Γ point) of the BZ are accessible [49]. This is schematically indicated by the broken line in Fig. 2.1. The line indicates the photon dispersion involving the velocity of light in vacuum c_0.

The Raman scattering process can be described classically in a macroscopic model. The polarization $\vec{P}(\omega_s)$ of the scattering medium is given by [47]:

$$\vec{P}\left(\omega_s\right) = \epsilon_0 \chi\left(\omega_i, \omega_s\right) \vec{E}_i\left(\omega_i\right), \tag{2.5}$$

where $\chi(\omega_i, \omega_s)$ is the generalized dielectric susceptibility tensor, $\vec{E}_i(\omega_i)$ is the electric field of the incident light wave, and ϵ_0 is the vacuum permittivity. Furthermore, the electric field can be described by:

$$\vec{E}_i(\omega_i) = \vec{E}_i^0 e^{i(\vec{k}_i \cdot \vec{r} - \omega_i t)}. \tag{2.6}$$

The dielectric susceptibility χ is connected to the dielectric permittivity by $\epsilon = 1 + \chi$. The dielectric susceptibility is modulated by the excitations resulting in scattered photons with shifted frequency. The exact form of the susceptibility is discussed separately for vibrational and electronic Raman scattering in Secs. 2.3.1 and 2.3.2, respectively.

In RS, the energy difference between incident and scattered light is denoted as Raman shift and is usually given in wavenumbers $\bar{\nu}_{\mathrm{RS}} = \frac{\nu_{\mathrm{RS}}}{c_0}$, where ν_{RS} is the frequency difference between the incident and the scattered photon. Wavenumbers, usually given in cm^{-1}, are related to other common spectroscopic units in Tab. 2.1.

Historically [50,51], inelastic light scattering was predicted by Smekal in 1923 [52]. The theory was further elaborated by Kramers and Heisenberg [53] and

separately by Dirac [54]. Experimentally, the effect was observed by Raman in liquids [55–57]. For this discovery the phenomenon was named Raman effect and he was awarded the Nobel Prize in physics in 1930 [51]. Nearly at the same time, Landsberg and Mandelstam independently observed the Raman effect in crystals (quartz and calcite) [58].

2.3.1. Vibrational Raman scattering

The mechanism of Raman scattering on phonons can be treated theoretically in two different models with the same result.

Macroscopic classical description

The dielectric susceptibility tensor $\chi(\omega)$ in Eq. (2.5) is modified by lattice vibrations, whose elongations can be expressed as [47]:

$$\vec{Q}_n = \vec{Q}_n^0 e^{i(\vec{q}_n \cdot \vec{r} - \Omega_n t)}. \tag{2.7}$$

The generalized dielectric susceptibility tensor can be therefore expressed in a Taylor expansion of the form [47]:

$$\chi_{\alpha,\beta}(\omega_i, \omega_s) = \chi^0_{\alpha,\beta}(\omega_i, \omega_s) + \sum_n \vec{Q}_n \left(\frac{\partial \chi_{\alpha,\beta}}{\partial \vec{Q}_n} \right)\Bigg|_0 (\omega_i, \omega_s) + \frac{1}{2} \sum_{n,n'} \vec{Q}_n \vec{Q}_{n'} \left(\frac{\partial^2 \chi_{\alpha,\beta}}{\partial \vec{Q}_n \partial \vec{Q}_{n'}} \right)\Bigg|_0 (\omega_i, \omega_s) + \dots . \tag{2.8}$$

In this equation the first term $\chi^0_{\alpha,\beta}(\omega_i, \omega_s)$ on the right-hand side stands for the static dielectric susceptibility. The second term denotes a one-phonon process, while the third term is for a process involving two phonons. Higher-order terms are not considered. Hence, the substitution of Eqs. (2.8) and (2.6) into Eq. (2.5) yields contributions to the polarization according to Eqs. (2.3) and (2.4).

The intensities of the Stokes and anti-Stokes spectra show temperature dependence according to the Bose-Einstein occupation factor n_{BE}. While the Stokes intensity is proportional to $n_{\mathrm{BE}} + 1$, the anti-Stokes intensity is proportional to n_{BE}. This connection results in an exponential intensity ratio [41,59]:

$$\frac{I_{aS}}{I_S} = \frac{n_{\mathrm{BE}}}{n_{\mathrm{BE}} + 1} = e^{-\frac{\hbar \Omega_n}{k_{\mathrm{B}} T}} \tag{2.9}$$

with

$$n_{\mathrm{BE}} = \left(e^{\frac{\hbar \Omega_n}{k_{\mathrm{B}} T}} - 1 \right)^{-1}, \tag{2.10}$$

where k_B is the Boltzmann constant. In principle, this ratio can be used to determine the temperature of a sample by RS. However, Eq. (2.9) just holds if the electronic transition matrix elements for the Stokes and anti-Stokes process are the same [60].

Following the theoretical calculation of surface phonons given in Sec. 2.1, the intensity of the vibrational Raman modes can be obtained by the Raman susceptibility tensor α_{ij}^m [33,61,62]:

$$\alpha_{ij}^m \propto \sum_{\kappa\beta} \frac{\partial \chi_{ij}}{\partial \tau_{\kappa\beta}} u_m(\kappa\beta), \tag{2.11}$$

where $\tau_{\kappa\beta}$ is the normal-mode displacement of atom κ in direction β, $u_m(\kappa\beta)$ are the corresponding eigenvectors, and χ_{ij} is the linear dielectric susceptibility as defined in Eq. (2.5). Other effects than vibrations are omitted due to limitations in computational resources [33]. With the Raman susceptibility α_{ij}^m the differential scattering efficiency can be defined as [34]:

$$\frac{dS^m}{d\Omega} = \frac{\omega_s^4}{(4\pi)^2 c_0^4} \mid \vec{e}_i \cdot \alpha_{ij}^m \cdot \vec{e}_s \mid^2 \frac{\hbar}{2\Omega_m} (n_m + 1), \tag{2.12}$$

with $\omega_s = \omega_i - \Omega_m$. The frequencies ω_i and ω_s as well as the polarization vectors $\vec{e}_i$ and $\vec{e}_s$ represent the scattered and incident photon, respectively, and Ω_m denotes the created phonon mode. Note the variation of the differential scattering efficiency with the forth power of the scattered frequency.

Microscopic quantum mechanical description

The vibrational Raman scattering is microscopically described by perturbation theory. It constitutes of three quantum mechanical processes building up the dielectric susceptibility [14,49]:

$$\chi_{\alpha,\beta}(\omega_i, \omega_s) \propto \sum_{e,e'} \frac{\langle 0|H_{\text{E-R},\beta}|e'\rangle \langle e'|H_{\text{E-L}}|e\rangle \langle e|H_{\text{E-R},\alpha}|0\rangle}{(E_{e'} - \hbar\omega_s)(E_e - \hbar\omega_i)}. \tag{2.13}$$

The indices α and β are the polarization directions of the incident and scattered light, respectively. The rightmost term in the numerator stands for the excitation of an electron from the ground state $|0\rangle$ to a virtual state $|e\rangle$ with energy E_e. The electron system is coupled via the Hamiltonian $H_{\text{E-R}}$ with the photon. The excited electron interacts with the crystal lattice and is transferred to the new virtual state $|e'\rangle$ with energy $E_{e'}$. This electron-phonon interaction is expressed as Hamiltonian $H_{\text{E-L}}$. The electron relaxes in the last step through emission of a photon into its initial ground state. The terms in the denominator indicate a resonance behavior if the energies of the virtual states are close to the photon energies. In case of (near) resonance, the Raman intensity can be greatly boosted. The process described by

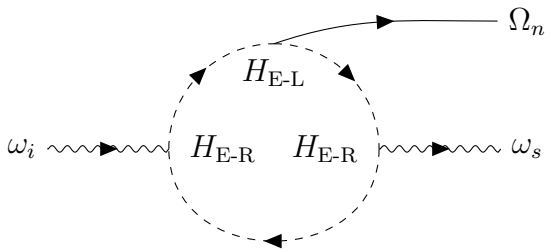

Figure 2.2.: Feynman diagram of the vibrational Stokes Raman process. The initial and final states as well as the vertices are labeled according to Eq. (2.13). Adapted from Ref. [59].

Eq. (2.13) can also be illustrated in a Feynman diagram. A typical one is depicted in Fig. 2.2.

By using Eq. (2.13), the cases of Stokes and anti-Stokes processes can be schematically represented in Fig. 2.3, which also includes the Rayleigh process.

In nonpolar crystals, like Si and Ge, the electron-phonon interaction of Eqs. (2.8) and (2.13) is restricted to deformation-potential scattering [12,47]. The bond lengths and angles are altered by the phonon leading to modifications of the electronic energies. In polar crystals, the vibrational displacements can additionally induce electric fields that give rise to Fröhlich scattering [12,47].

Relation to infrared absorption

Raman scattering of phonons is closely related to absorption of photons in the IR spectral range. The associated experimental method is called IR spectroscopy and is complementary to Raman spectroscopy [44]. In contrast to the visible photons in Raman scattering, photons with frequencies in the IR can interact directly with the crystal lattice and excite lattice vibrations [43]. Hence, only one photon is involved in IR absorption and it is considered as first-order process. Raman scattering is a second-order process since two photons and an intermediate state participate [44].

2.3.2. Electronic Raman scattering

Besides vibrational Raman scattering, inelastic scattering may also occur on electrons. Here, there will be a focus on electronic Raman scattering on CFEs, which arise due to lifted degeneracy of electronic states in the CF.

The quantum mechanical description of the dielectric susceptibility tensor of Eq. (2.5) for the electronic Raman scattering is given by [42]:

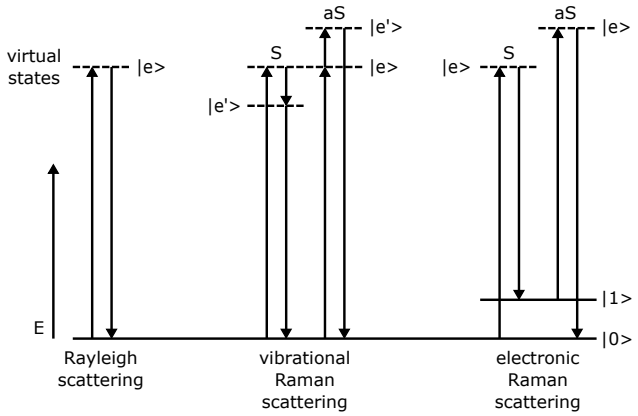

Figure 2.3.: Schematic representation of the vibrational and electronic Raman scattering process. For both processes, the Stokes (S) and anti-Stokes (aS) case is shown. The Rayleigh scattering mechanism is also depicted. The states are named according to the Eqs. (2.13) and (2.14). In this picture, the E axis denotes the energy of the electron system.

$$\chi_{\alpha,\beta}\left(\omega_i, \omega_s\right) \propto \sum_e \left(\frac{\langle 1|H_{\text{E-R},\alpha}|e\rangle \ \langle e|H_{\text{E-R},\beta}|0\rangle}{(E_e - \hbar\omega_i)} + \frac{\langle 1|H_{\text{E-R},\beta}|e\rangle \ \langle e|H_{\text{E-R},\alpha}|0\rangle}{(E_e + \hbar\omega_s)} \right). \quad (2.14)$$

This equation is different compared to Eq. (2.13) in the sense that the final electronic state $|1\rangle$ is not equal to the initial state $|0\rangle$. Thus, in this case the net energy transfer to the electron system gives rise to frequency shifts between incident and scattered photon. Here, only two processes are involved. Note that the term in the left denominator exhibits a similar resonance behavior as in Eq. (2.13). This tensor, in contrast to the vibrational case, is asymmetric but can be decomposed into a symmetric and antisymmetric part [42]. The resulting Stokes and anti-Stokes processes are also depicted in Fig. 2.3.

Unlike for vibrational Raman scattering, the temperature-dependent intensity development of electronic Raman scattering is much different. Distinct peaks due to electronic scattering usually require low temperatures to be observable in the Raman spectra (the actual temperature range depends on the material system). The reasons are variations in the electronic occupation and increasing phonon-induced decay of excited electronic states with increasing temperature [42]. Moreover, the ratio of Stokes and anti-Stokes intensity found for vibrational Raman scattering in Eq. (2.9) is not valid for electronic Raman scattering since no bosons are involved.

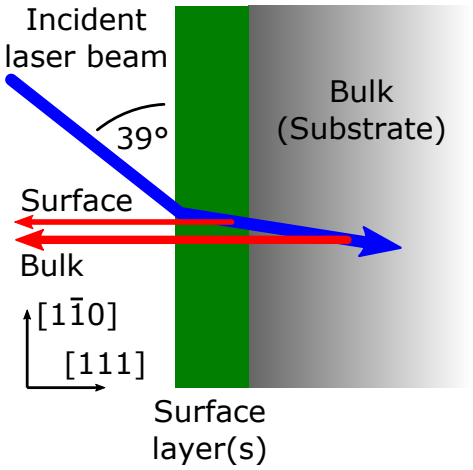

Figure 2.4.: Schematic illustration of the different contributions to the scattered light in SRS. The surface layers can consist of adsorbed atoms, new material compositions, or altered surface structures with respect to the bulk. Adapted from Ref. [65].

Another form of electronic Raman scattering can be observed as broad background for investigating metal surfaces, e.g., Pt. Light scatters inelastically on free electrons creating electron-hole pair excitations within the conduction band [63,64]. This background is typically too flat to interfere with distinct peaks related to other scattering mechanisms.

2.3.3. Surface Raman spectroscopy

Raman spectra of solids are always a superposition of contributions from the surface and the bulk as schematically indicated in Fig. 2.4. The scattered light attributed to the bulk prevails since the surface provides only an extremely small scattering region. Typically, the intensity contribution of the bulk exceeds the surface contribution by a factor $10^3 - 10^4$. The spectroscopic method that is specialized to collect Raman scattered light from the surface is termed SRS. If the surface is reconstructed or altered in another way, this gives rise to vibrational modes and electronic excitations that are specific for this surface.

An approved method to distinguish between contributions from the surface and the bulk is to compare the Raman spectrum of a sample with a specially prepared surface to a sample without treated surface. The difference between both spectra gives information about modifications of the surface. For the semiconductor samples, the aged and unreconstructed surface can be achieved by exposure to increased

pressures of $p \gtrsim 1 \cdot 10^{-8}$ mbar for several minutes or by usage of an unprepared and untreated surface. In the case of the intermetallics systems, the reference sample can be the substrate crystal without the intermetallic film.

SRS needs to be distinguished from surface-enhanced Raman scattering (SERS), that is usually used for the investigation of molecules, which are adsorbed on suitable metal substrates, that boost the Raman intensity by several orders [66,67].

2.4. Group theoretical analysis and selection rules

Symmetry is a very fundamental concept in physics. Considerations concerning symmetry can be treated qualitatively in the framework of group theory. In a mathematical sense, a group is defined as a quantity of elements and assigned operations which obey certain properties (closure, associativity, identity, and inverse element) [44].

Vibrational as well as electronic Raman scattering follows certain symmetry-governed principles. As a first step, it is necessary to know the symmetry of the static crystal. Then, the vibrational eigenmodes and electronic excitations can be determined which leads to selection rules for allowed Raman scattering processes.

Basic concepts and symmetry properties of crystals

Matter in crystalline form can be classified in terms of symmetry groups. The ideal infinite 3D crystal can be composed of elementary UCs. The UCs and also the crystal are invariant under certain symmetry operations. Depending on the symmetry, these operations are, among others, rotations, reflections, and inversions (cf. Sec. B) [44]. If only a single UC is considered, all symmetry operations projecting the UC onto itself define the applying so-called point group. Space groups are built by including translations, glide planes, and screw axes [44]. Point and space groups are closely related to crystal systems and Bravais lattices [43]. The number of different symmetry groups is finite and listed [68].

For each point group, the valid symmetry operations are sorted in classes, that are of equal number as the irreducible representations of the group. An irreducible representation can be, for instance, a matrix that cannot be transformed into block diagonal form [44]. Since these matrices are ambiguous, the trace of the representation is used. The trace, defined as the sum over the diagonal matrix elements, is invariant under transformations and is also called character. Furthermore, each irreducible representation has specific basis functions that can be generated from the space coordinates x, y, and z. In turn, these basis functions can be used to generate the matrices of the irreducible representations. The characters and basis functions are listed in character tables for each point group (see for instance Refs. [43,68] and Sec. B).

If half-integer angular momentum states, i.e., the electron spin $\frac{\hbar}{2}$, need to be

considered, point groups are extended to double groups [44]. The number of irreducible representations and symmetry classes rises. The double groups are listed analogously to the point groups (see for instance Ref. [68] and Sec. B).

At surfaces, the extension of the crystal is limited in one dimension resulting in a reduced symmetry. The symmetry group of a surface can be indicated either by a 2D space or point group or by a 3D group with reduced symmetry. The 2D space groups are tabulated in Ref. [69] and related to their 3D counterparts in Ref. [70]. Since the displacement vector of a moving atom can have a component normal to the surface plane and the surface can be buckled, it is convenient to use the 3D point group when surface phonons are involved. A compilation of all 2D and 3D symmetry groups which are relevant for this thesis are listed in Sec. A.

For 2D and 3D symmetry groups, the atoms building the UC are on specific Wyckoff positions. Each Wyckoff position obeys the symmetry operations of the site-symmetry group [44]. This site symmetry is equal or lower than that of the point or space group of the UC. The position is labeled by a number, indicating the multiplicity, and a consecutive letter. A list of Wyckoff positions of the 3D point groups can be found in Ref. [71].

Vibrational properties of crystals

The occupied Wyckoff positions in the UC can be utilized to determine the normal modes of the bulk material. A normal mode is connected to a vibrational displacement pattern that is conform with the site symmetry. Each position is associated with a set of irreducible representations of the point group of the crystal. The total number of normal modes is equal to $3N$ as explained in Sec. 2.1. There are several group theoretical methods for the determination of phonons near the Γ point, of which the nuclear site group analysis and its extension to crystals is of special interest here [71]. The total number of normal modes and its symmetry properties can be identified by the tables in Ref. [71]. In addition, there are several computer programs that can also obtain these information for verification and comparison (see for instance Ref. [72]).

The irreducible representations are labeled according to their dimensionality, which can be obtained by the character of the identity transformation. “A” and “B” are 1D, “E” are 2D, and “T” are 3D representations. If there is more than one representation with the same dimensionality an index of a consecutive number is appended. A special situation occurs for a point group with an inversion operation. Then, the representations are divided into even and odd parity, denoted as “g” (gerade) and “u” (ungerade), respectively.

The considerations so far only regard the Γ point of the BZ. For phonon branches away from the Γ point, i.e., other high symmetry points, the symmetry might be reduced.

Vibrational displacement pattern of normal modes

For the normal modes found for a specific crystal, the atomic displacements compatible with the point group can be obtained. The displacement vectors must also be invariant under the applying symmetry operations. The vibrational pattern of the normal modes can be found via projection operator algebra [44]:

$$\hat{P}^{\Gamma_n} = \frac{l_n}{h} \sum_R \chi^{\Gamma_n}(R)\, \hat{P}_R. \tag{2.15}$$

In Eq. (2.15), $\hat{P}^{\Gamma_n}$ is the projection operator, l_n is the dimensionality of the irreducible representation, and $h = \sum_n l_n^2$ is the order of the point group. The product of the character $\chi^{\Gamma_n}(R)$ and the symmetry operator $\hat{P}_R$ is summed over all symmetry operations R of the point group. For the implementation of Eq. (2.15), the operators are applied to an arbitrary displacement of one atom that is chosen to be presumably correct. Through the symmetry transformations and the summation, contributions that are not conform with symmetry are canceled out. The result are the displacement vectors for the considered atom and the atoms belonging to the same Wyckoff position for the specific irreducible representation.

Crystal field properties of crystals

The energy levels of electrons in a crystal are also labeled by irreducible representations of the double point group. For the differentiation with vibrational normal modes, the representations are all indicated by Γ and an consecutive index number. Even and odd parity is marked by a "+" and "−", respectively. The number of irreducible representations for a double group exceeds the representations for point groups for vibrational modes.

Selection rules for Raman spectroscopy

The observation of scattered light in Raman experiments depends on two conditions: the symmetry properties of the excitation must enable Raman scattering and the chosen experimental measurement conditions considering the polarization directions of the incident and scattered light must allow the observation. Both requirements must be fulfilled simultaneously. They are discussed in the following.

In general, a matrix element of the form $\langle\psi_f|\mathcal{O}|\psi_i\rangle$ can be evaluated, whether it vanishes or not, in the framework of group theory. The transition between ψ_i and ψ_f, which are the initial and final states, respectively, is coupled by the operator $\mathcal{O}$. The states as well as the operator transform according to specific representations of the symmetry group and are invariant under the applicable symmetry operations [44]. The direct product of the irreducible representations of each participating component is used to determine if the result is vanishing or non-vanishing [43]:

$$\langle\psi_f|\mathcal{O}|\psi_i\rangle \longrightarrow \Gamma_i \otimes \Gamma_{\mathcal{O}} \otimes \Gamma_f = \sum_n c_{ifn}\Gamma_n. \tag{2.16}$$

The direct product reveals all representations that are contained. Technically, the characters for all symmetry operation classes are multiplied separately. Subsequently, the resulting reducible representation can be decomposed into a sum of irreducible representations [44]. The matrix element can only be nonzero, if the direct product includes the totally symmetric irreducible representation, i.e., the A_{1g} representation. In other words, the matrix element in Eq. (2.16) only does not vanish if the direct product contains a component that transforms like a scalar constant [43,44]. Note that the totally symmetric irreducible representation will only appear in a direct product of an irreducible representation with itself [43].

The considerations of Eq. (2.16) can be applied to vibrational transitions as in vibrational RS. The crystal lattice undergoes a transition from a ground state to an excited state. The initial state is considered as fully symmetric and the operator transforms like the change of the susceptibility of Eq. (2.8), i.e., like a symmetric second-rank tensor. Therefore, a normal mode is Raman active, if the excited normal mode also transforms as a symmetric second-rank tensor. The Raman-active modes have quadratic basis functions. In contrast, modes that transform like vectors are called IR active. If the UC of a crystal has an inversion center, the modes can be exclusively either Raman or IR active [44]. Modes that are not Raman nor IR active are called silent modes.

In the case of electronic RS, e.g., of CFEs in materials containing rare-earth elements, selection rules for quadrupole interaction (comparable to a subsequent series of two dipole transitions) apply [73]. Hence, generally only electronic transitions with $\Delta J = 0, \pm 1, \pm 2$ and $\Delta M_J = 0, \pm 1, \pm 2$ are allowed [42,74]. The selection rules between electronic states are tabulated for each double point group for the common main crystal axes [42,75]. Furthermore, parity must be conserved in electronic Raman scattering. The parity of an electronic state is defined as $(-1)^l$ for crystals with inversion symmetry [42,44]. The parity changes in the direct products according to [68]:

$$\Gamma_i^{\pm} \otimes \Gamma_f^{\pm} = \sum_n c_{ifn} \Gamma_n^{+}, \tag{2.17}$$

$$\Gamma_i^{\pm} \otimes \Gamma_f^{\mp} = \sum_n c_{ifn} \Gamma_n^{-}. \tag{2.18}$$

Since for dipole transitions the parity of the states must be opposite, electronic Raman scattering on a $4f^n$ state involves an intermediate electronic configuration like $4f^{n-1}5d$ [73]. The predictions of Eq. (2.16) are not only valid for the electronic transitions of Eq. (2.13) but also for the electronic transitions of Eq. (2.14).

The partial derivative of the dielectric susceptibility in Eq. (2.8) is a third-rank tensor. For scattering on phonons, this derivative together with the normalized vector $\hat{Q}_n^0$ in the direction of the phonon displacement defines the Raman tensor $\mathcal{R}$

[12]:

$$\mathcal{R} = \sum_n \left(\frac{\partial \chi_{\alpha,\beta}}{\partial \vec{Q}_n} \right)\Bigg|_0 \hat{Q}_n^0. \tag{2.19}$$

Hence, $\mathcal{R}$ is a second-rank tensor that transforms like the irreducible representation of the phonon $\vec{Q}_n$ defined in Eq. (2.7) [43]. It can be constructed by the basis function of the applicable irreducible representation. The Raman tensor has the general form:

$$\mathcal{R} = \begin{pmatrix} xx & xy & xz \\ yx & yy & yz \\ zx & zy & zz \end{pmatrix}. \tag{2.20}$$

The tensors are tabulated for each point group for the common main crystal axes (see for instance Refs. [59,61,76]). Note that the Raman tensor is not unique in the sense that entries in the tensor can be shifted to other connected tensors in accordance with symmetry. For scattering from other crystal faces, the Raman tensor $\mathcal{R}$ has to be rotated accordingly.

With the aid of the Raman tensor $\mathcal{R}$, the intensity I_{RS} of Stokes scattering can be determined with the polarization vectors $\vec{e}_i$ and $\vec{e}_s$, which denote the polarization directions of the incident and scattered light, respectively [12]:

$$I_{\mathrm{RS}} \propto \left| \vec{e}_i \cdot \mathcal{R} \cdot \vec{e}_s \right|^2. \tag{2.21}$$

Whether the intensity I_{RS} vanishes or not, can be controlled by the externally tunable polarization directions. Note the similarity with Eq. (2.12). To sum up, a vibrational or electronic excitation can be observed in RS if symmetry considerations prove it to be Raman active and the adjusted polarization elements in the experiment allow a detection. In the next section, the experimentally achievable polarization configurations are explained in detail.

2.5. Experimental Raman and preparation setup

The SRS setup consists of two main parts. The optical part includes all devices that are necessary to perform the optical Raman measurements. The ultrahigh vacuum (UHV) part comprises the vacuum chambers for the preparation of the samples and the storage during the measurements. Hence, after preparation the samples can be measured *in situ* without exposition to atmosphere. In the following, the latest state of the setup is described.

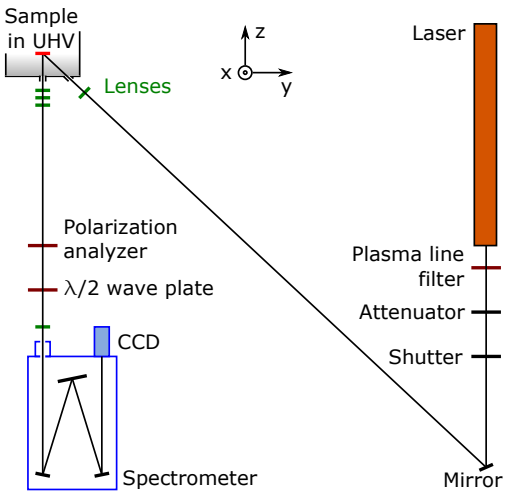

Figure 2.5.: Schematic top view of the optical Raman setup. The laser beam is focused onto the sample, which is in the UHV chamber. The scattered light is then analyzed by a polarization analyzer and the spectrometer.

2.5.1. Optical Raman setup

The optical path of the experiment is depicted schematically from a top view in Fig. 2.5. The samples are excited by an Ar^+ ion gas laser (Coherent Innova 90) with the laser lines 488.0 nm (≅2.54 eV) and 514.5 nm (≅2.41 eV) with laser powers of 100 – 300 mW, which is measured with a power meter. The Brewster windows terminating the laser tube polarize the beam vertically. The laser beam first passes a wavelength-specific clean-up filter (Semrock MaxLine) that suppresses plasma lines and can subsequently be attenuated by neutral-density filters. It is then focused on the sample in the UHV chamber with an achromatic lens with a focal length of 250 mm. The use of achromatic lenses ensures equal optical properties for light of different wavelengths in the relevant spectral range. All utilized lenses have antireflection coatings. The spot on the sample has a diameter in the range of 100 µm which equals a power density of ≈1250 W/cm^2 at 100 mW. The power density needs to be low enough to prevent uncontrolled sample heating in the region of the laser spot. The direct reflex from the sample is blocked by a beam trap.

The scattered light from the sample is collected and collimated by a lens system of three achromates with an aperture of f/3 (see Fig. 2.6). The lens system includes a diaphragm in an intermediate focal plane for stray-light suppression. The collimated beam is passing several optical elements. Laser-line filters block the strong elastically scattered laser light. Either an ultrasteep long-pass edge filter (Semrock RazorEdge) or two Bragg notch filters (OptiGrate BragGrate) are employed. All filters are

wavelength-specific and are characterized by edges that are as steep and close to the laser wavelength as possible (see Sec. G). The edge filter allows measurements of the Stokes spectrum down to $35\,\mathrm{cm}^{-1}$. In contrast, with Bragg notch filters Stokes and anti-Stokes spectra down to $|25\,\mathrm{cm}^{-1}|$ can be recorded simultaneously. An advantage of the edge filter over the Bragg notch filter is its very high transmission throughput. The beam can be analyzed by a linear polarization analyzer. The last achromat focuses the beam onto the entrance slit of the spectrometer.

The single grating spectrometer (Spex 1000M) in Czerny-Turner design has a focal length of 1.0 m and an aperture of f/8. The entrance slit width is usually set to 100 µm. Inside the spectrometer, a blazed holographic grating with a groove density of 1500/mm is installed. The highest efficiency of the grating is achieved if the polarization of the incident light is parallel to the grooves and it drops for perpendicular orientation. Therefore, an achromatic $\lambda/2$ wave plate in front of the spectrometer is used to obtain the same efficiency of the grating for both polarization configurations. For perpendicular (i.e., horizontal) alignment, the polarization of the beam is rotated by the $\lambda/2$ wave plate by 90°, while it passes the plate unaltered for parallel orientation. On the exit, the spectrometer is equipped with a Si-based charge coupled device (CCD) detector (Andor iDus DU401A). The chip has a (1024 × 127) pixel array with a pixel size of 26 µm × 26 µm. The vertical range of illuminated pixels is specified and binned to improve the signal-to-noise ratio. The CCD detector is Peltier-cooled to 193 K and has a quantum efficiency of ≈85 % at this temperature in the relevant spectral range.

The Raman spectra are recorded by a self-written automated program with integrated background correction. For the background measurements the shutter blocks the laser beam while a spectrum is registered as it would be in normal operation mode. Typical integration times are three accumulations with 300 s each. For special purposes integration times can be varied. The frequency axis of the Raman spectra is calibrated by second-order polynomial fitting of measured plasma lines to tabulated frequencies of Ar^+ transition lines. To obtain spectra with plasma lines, the clean-up filter is removed from the laser beam while leaving the remaining setup unchanged (see Sec. E). The reference values for the plasma lines are taken from Ref. [77]. In some cases, the Raman spectra are smoothed by the Savitzky-Golay algorithm and in cases, where the laser edge leaks through the filters, a manual background correction can be applied.

The spectral resolution (full width at half maximum (FWHM)) of the Raman setup is approximately $2\,\mathrm{cm}^{-1}$. This can be seen as closest separation between two features that can be resolved as distinct peaks. However, peak positions can be determined more precisely due to fitting of the Raman spectra. Usually Voigt profiles are used, which are a convolution of a Gaussian and a Lorentzian profile [78]. The Gaussian resembles the slit function of the spectrometer, while the Lorentzian characterizes the physical line shape. Therefore, a spectral peak position accuracy of $\approx 0.1\,\mathrm{cm}^{-1}$ can be achieved after fitting procedures.

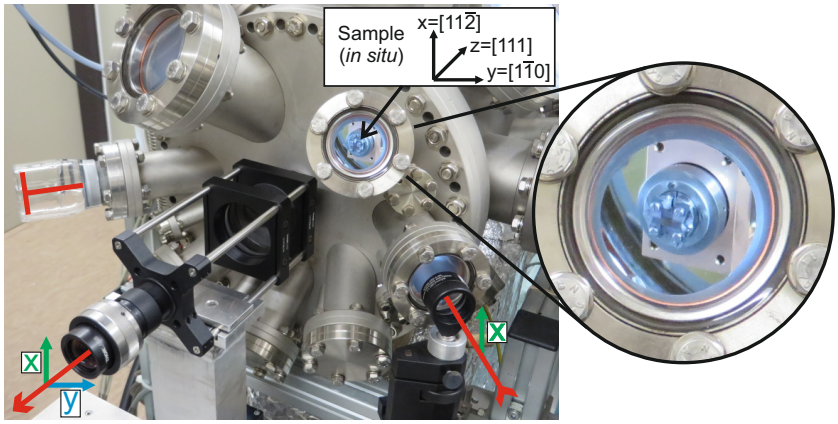

Figure 2.6.: Optical UHV Raman chamber with indications of the polarization properties of the incident and scattered laser light. The inset depicts the crystal axis orientations of the sample in the Raman chamber. The labels illustrate the Porto notation of Eq. (2.22) as used in the measurements.

The Raman measurements are conducted in quasi-backscattering geometry. The inclination of the incident laser beam with respect to the normal of the (111) sample surface is 39° (see Figs. 2.4 and 2.6). The relevant angle is reduced according to Snell's law due to refraction towards the surface normal direction since the refractive index of the sample holds $n > 1$. The refractive indices of the sample substrates Si, Ge, and Pt at 488 nm are 4.37, 4.24, and 1.94, respectively [79]. Therefore, the deviation from the ideal backscattering geometry, where incident beam and surface normal are parallel, is only small.

The polarization configurations of the Raman spectra are denoted according to the Porto notation [47,80]:

$$\vec{k}_i\,(\vec{e}_i\vec{e}_s)\,\vec{k}_s. \tag{2.22}$$

The propagation and polarization vectors of the incident and scattered light are defined as in Eqs. (2.4) and (2.21). The vector normal to the (111) surface is denoted as z direction. Furthermore, the polarization of the laser beam is labeled as x direction and accordingly holds $x \perp y$. The x and y directions are usually chosen to be parallel to the crystal axes. For (111) surfaces this yields $x \parallel [11\bar{2}]$ and $y \parallel [1\bar{1}0]$. The polarization analyzer in front of the spectrometer selects either the x or y polarization. So there are two possible polarization configurations: $z(xx)\bar{z}$ and $z(xy)\bar{z}$. If no polarization analyzer and $\lambda/2$ wave plate are used, the spectra are labeled as $z(xu)\bar{z}$ with $u = x + y$, where u stands for unpolarized. The used polarization configurations are also indicated in Fig. 2.6.

Additionally, a HeNe gas laser with 632.8 nm (≅1.96 eV) and a laser power of

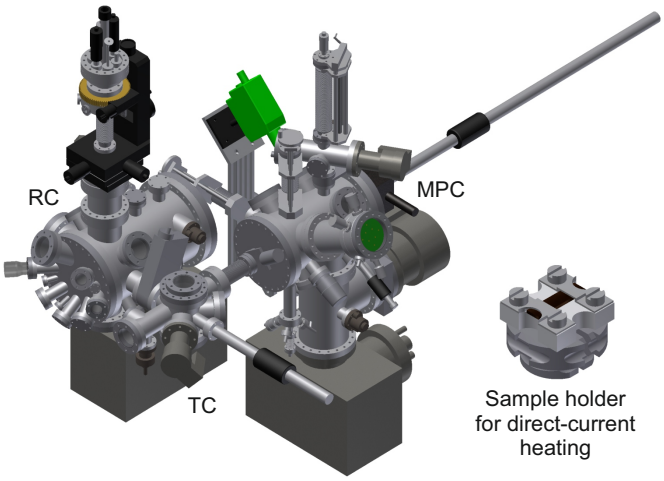

Figure 2.7.: Experimental UHV setup consisting of the Raman chamber (RC), the mobile preparation chamber (MPC), and the transfer chamber (TC). On the right, a sample holder for the direct-current heating of the semiconductor samples is displayed.

19 mW can be integrated into the optical setup.

2.5.2. Ultrahigh vacuum preparation setup

The UHV complex connects three different chambers. It is illustrated in Fig. 2.7. The Raman chamber is connected through the transfer chamber with the mobile preparation chamber. The mobile preparation chamber is part of the Forschergruppe FOR1162 and is detachable. Thus, it is transportable to other measurement facilities and ensures similar preparation conditions within the group of involved research teams.

The base pressure in all UHV chambers is $p < 1 \cdot 10^{-10}$ mbar measured with hot filament ion pressure gauges. According to an approximation for a dosage of one Langmuir, the time until the sample surface is covered again with adsorbates accounts to several hours [15]. Thus, the surfaces of the samples are not affected during the Raman measurements. To achieve the low pressures, turbomolecular pumps with membrane rough pumps and ion getter pumps with included Ti sublimation pumps are employed and additionally all chambers are baked out.

The mobile preparation chamber is equipped with several components for preparation. The samples can be heated by direct-current heating or alternatively by electron bombardment of an e-beam filament. To use direct current, a power supply (TDK-Lambda Genesys) capable of delivering 12.5 A and 750 W is employed. In the case of e-beam heating, electrons are emitted by the hot filament and accelerated by high voltage onto the sample. Direct-current heating is preferred over e-beam

heating from the front side since it avoids the contamination of the surface. The sample temperature is contactlessly controlled by a pyrometer. For the semiconductor substrates a special pyrometer (LumaSense Impac IS 12-Si) for silicon wafers is used. It can measure temperatures of 670 – 1570 K. As a calibration parameter, the material-specific emissivity is set to 67 % for Si and 58 % for Ge [81,82]. The temperature of the Pt substrate is measured by a conventional pyrometer. For the removal of the topmost atomic layers, a sputter gun for sputtering with Ar^+ ions is installed. The accelerated ions bombard the surface excavating the surface atoms. For providing the atoms to be deposited on the sample surface, an e-beam evaporator (Omicron Focus EFM3) is used to deposit the atoms on the sample surface. The barrel of the evaporator can be loaded with one evaporant element species at a time (Au, Ce, La, or Sn). A suitable barrel material is chosen according to the evaporant. The flux is controlled by a water-cooled quartz crystal microbalance. The quartz crystal is stimulated to oscillations whose frequency decreases if adatoms are attached to its surface. Thereby, the deposited amount can be measured exactly. After preparation, the surface reconstructions can be checked for quality by low-energy electron diffraction (LEED). To observe LEED patterns, electrons of well-defined energy ($E \lesssim 100\,\mathrm{eV}$) are scattered elastically on the surface. The resulting diffraction spots are very sensitive to the surface reconstruction, due to the small penetration depth of the electrons. The interference pattern depends on the electron energy and can be visualized on a phosphorous screen [15]. The recorded LEED patterns are edited to reveal all structures.

To prepare the semiconductor samples, a sample holder that allows electrical current flow through the sample is used (see Fig. 2.7). To achieve this, the basic bayonet-like sample holder is split in two electrically separated Mo contacts. They are stabilized by an electrically insulating sapphire crystal. Sapphire is a good choice since it has a good heat conductivity at low temperatures while being insulating [83]. The semiconductor samples are fixed on the crystal by Ta clamps and positioned so that its edge regions are connected to the Mo contacts. The intermetallic systems are prepared on a single Pt crystal which is connected to a transferable bayonet-like sample holder. All sample holders can be moved by transfer sticks through all chambers. The samples on its holders are initially transferred into the vacuum chamber via the load lock of the mobile preparation chamber without breaking the UHV.

In the Raman chamber the optical measurements are performed (see Fig. 2.6). Therefore, the sample can be positioned to ensure the required orientation and placing for the incident laser beam. The laser beam is directed into the chamber through a chamber window. Scattered light and the direct reflection are coupled out in the same way.

The Raman chamber has a continuous-flow cryostat inset that enables cooling of the samples. In addition to measurements at room temperature (RT, $T \approx 300\,\mathrm{K}$), the samples can be cooled to low temperatures (LT, $T \approx 20 – 40\,\mathrm{K}$). The cryostat

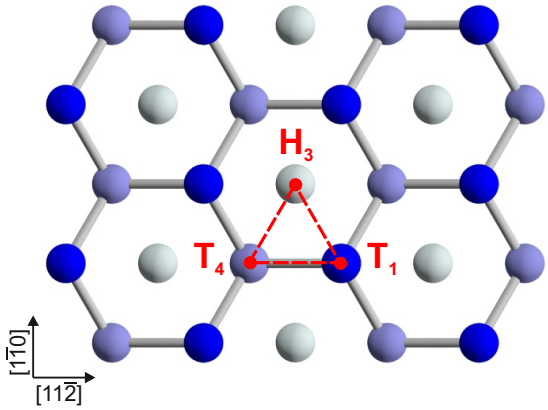

Figure 2.8.: Indications of the surface positions T_4, H_3, and T_1 on a (111) surface of a crystal with diamond structure.

temperature is controlled by a Pt100 resistive sensor in 4-wire connection. The cryostat has a manipulator which allows translational movements in all directions. Furthermore, samples are rotatable around two axes. This chamber is equipped with a separate LEED.

If no UHV conditions are required, a small cold-finger cryostat can be used. It has easy access for loading with samples and can be cooled with liquid N_2. The cryostat is evacuated by a turbomolecular pump with a membrane rough pump.

2.6. Nomenclatures

In this thesis several commonly accepted nomenclatures are used, apart from the already explained ones.

Surfaces and its orientation are indicated by the Miller indices "hkl". It is differentiated between planes indicated by round brackets, i.e., (hkl), and directions indicated by squared brackets, i.e., [hkl] [84].

On top of (111) surfaces of a crystal with diamond structure there are special positions that are preferentially occupied or serve as reference [85]. A surface structure with marked positions is given in Fig. 2.8. An atom on a T_4 position is located atop the surface in the middle of three substrate atoms. Whereas the H_3 adatoms sit in the middle of a hexagon formed by atoms of the first and second substrate layer. The T_1 adatoms are vertically above the first layer atoms.

Surface reconstructions are labeled in accordance with the Wood notation. This notation reflects the length ratio of the reconstructed SUC with respect to the intrinsic unreconstructed UC [10,84]. The resulting description for a clean-surface

reconstruction can be given as [10]:

$$\text{S(hkl)-}\kappa \left(\frac{|\vec{a}_1'|}{|\vec{a}_1|} \times \frac{|\vec{a}_2'|}{|\vec{a}_2|} \right) R\varphi. \tag{2.23}$$

This notation starts with the chemical composition "S" of the substrate by appending the already introduced Miller indices of the surface. The following κ is replaced by a "c" for centered SUCs, and is usually omitted for primitive SUCs. The ratios in brackets give the relation of the unit vectors $\vec{a}_1'$ and $\vec{a}_2'$ of the surface to the corresponding vectors $\vec{a}_1$ and $\vec{a}_2$ of the substrate. If the SUC is rotated against the substrate UC, the angle φ between $\vec{a}_1'$ and $\vec{a}_1$ is specified by the notation $R\varphi$. This information is sometimes left out for brevity.

For adsorbate-induced reconstructions, the notation of Eq. (2.23) is slightly altered to:

$$\text{A-}\kappa \left(\frac{|\vec{a}_1'|}{|\vec{a}_1|} \times \frac{|\vec{a}_2'|}{|\vec{a}_2|} \right) R\varphi/\text{S(hkl)}. \tag{2.24}$$

With the atomic species of the adsorbate given in "A", the meanings are same as before. In cases where the reconstruction plays a circumstantial role, the notation can be recast to:

$$\text{A/S(hkl)}. \tag{2.25}$$

This short version is applied to the surface adsorbate systems as well as to the surface intermetallic systems. In the latter case "A" is replaced by the intermetallic compound.

3. Surface adsorbate systems

In this chapter, the semiconductors Si(111) and Ge(111) with surface coverages of Au and Sn in the (sub-)ML regime are investigated. Furthermore, the reconstructions of the clean semiconductor surfaces are examined. The phase diagrams for the Au/Si(111), Sn/Ge(111), and Sn/Si(111) systems are presented to show the variety of possible surface reconstructions and to motivate the preparation conditions for the desired reconstructions.

The Au-reconstructed Si(111) surfaces as well as the Si(111)-(7×7) surface were investigated in close cooperation with the department Nanostrukturen of the Leibniz-Institut für Analytische Wissenschaften - ISAS - e.V. in Berlin. These surface systems were thus additionally studied with a different Raman setup yielding further confirmation of the reproducibility. Furthermore, calculations regarding the Au-reconstructed Si(111) surfaces were performed by S. Sanna and coworkers from the Institut für Theoretische Physik at the Justus-Liebig-Universität in Gießen. The DFT calculations were performed as implemented in the Vienna *ab initio* simulation package (VASP) [86,87]. Most parts of the results presented in this chapter are published in Refs. [33,34,88].

3.1. Bulk semiconductors Si(111) and Ge(111)

The bulk region of the samples dominates the recorded Raman spectra and therefore also determines the relevant frequency range.

Si and Ge are isovalent and crystallize both in the diamond structure. This structure consists of two face centered cubic (FCC) lattices of which one is diagonally shifted by $\frac{a}{4}$ in [111] direction, with a being the cubic lattice constant. It belongs to the point group O_h [12]. In Fig. 3.1, a UC is depicted together with a (111) plane. The (111) plane separates the UC diagonally and exhibits a hexagonal surface structure that belongs to the surface space group $p3m1$ (corresponding to the 3D point group C_{3v}) [10]. Due to this similarities, the Raman spectra of Si(111) and Ge(111) are closely related and will be described together.

The most intense peaks in the Raman spectra of both are at 520 and 300 cm^{-1} for Si [89,90] and Ge [91], respectively. This can be observed in Fig. 3.2. The deviation in frequency is a result of the mass difference and the different atomic distances. These peaks are attributed to the LTO phonon, which is degenerate at the Γ point of the BZ. This degeneracy is due to the absence of LO-related

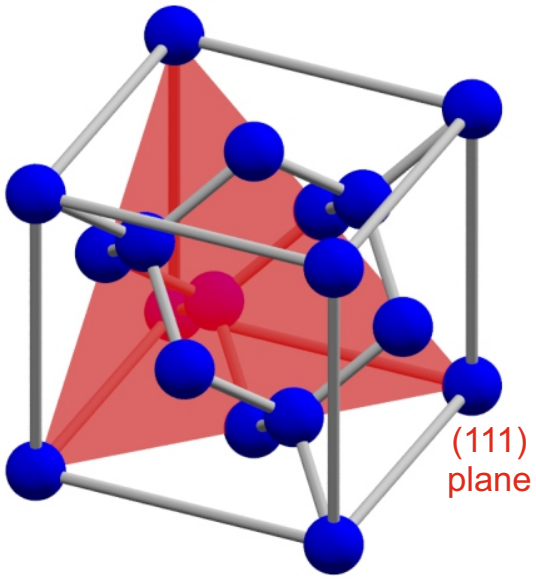

Figure 3.1.: The bulk UC of the diamond structure with indication of the relevant (111)-oriented plane. The semiconductors Si and Ge crystallize in the diamond structure.

electric fields in non-polar crystals with diamond structure [12]. This first-order peaks strongly exceeds the vertical scale, because it is about a factor 10^2 more intense than the surrounding structures. The selection rules for the LTO phonon mode at the (111) surface can be predicted by utilizing Eq. (2.21). To apply this equation, the three Raman tensors for the degenerate T mode of O_h must be rotated [92]. The explicit calculation yields that the two TO modes are observable in both polarization configurations $z(xx)\bar{z}$ and $z(xy)\bar{z}$. In a configuration with $z(xx)\bar{z}$ polarization the LO mode is additionally observed, while in a $z(xy)\bar{z}$ spectrum it is not [12]. Under the assumption of comparable entries in the Raman tensors, the intensity will drop in the $z(xy)\bar{z}$ spectrum by $\frac{1}{3}$, as is indicated by the LTO onsets in Fig. 3.2 for Si(111) and Ge(111).

Apart from the first-order LTO structures, there are many overtone and combination modes. The most prominent one is attributed to the second-order transversal acoustic (2TA) phonon peaks which are centered at 300 and 163 cm^{-1} for Si and Ge, respectively. These Raman signatures have an extremely broad structure and resemble the phonon density of states (PDOS) [13,91,93]. The center is assigned to the X point of the BZ and hence denoted as 2TA(X) [89–91]. This peak also gains weight from the closely located Σ point. The intensity declines to the left and right side to the L and W points, respectively. The actual shape of the 2TA is slightly different between Si(111) and Ge(111) and also depends on the exciting laser wavelength [94,95] (see Sec. D). As expected for second-order peaks, the intensity

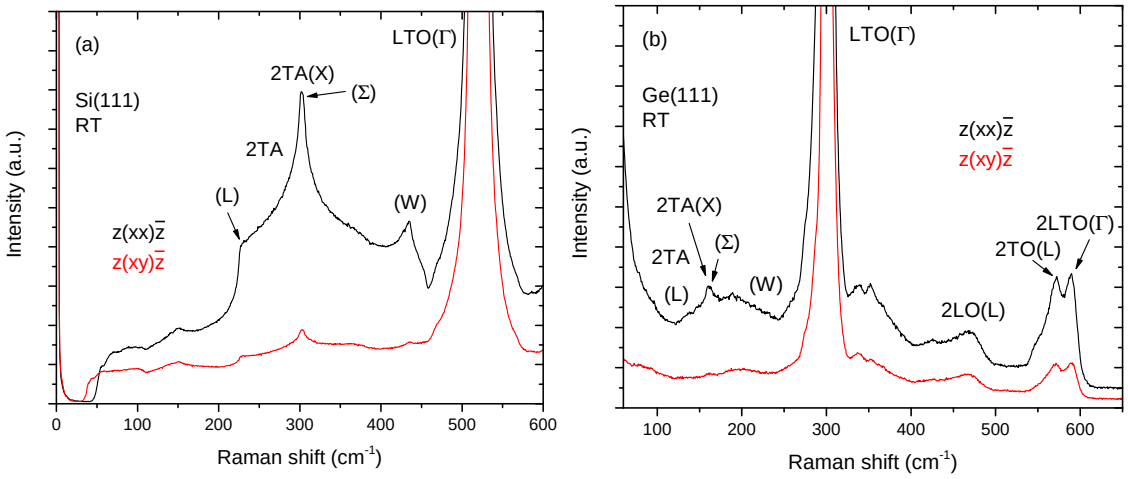

Figure 3.2.: Raman spectra of the bulk semiconductors (a) Si(111) and (b) Ge(111). The spectra are shown for the polarization configurations $z(xx)\bar{z}$ and $z(xy)\bar{z}$ for RT. The labels indicate the origin of the vibrational structures and the corresponding positions in the BZ.

considerably declines in the $z(xy)\bar{z}$ spectrum.

Above the LTO phonon, there are further Raman features. These peaks are shown for Ge(111) in Fig. 3.2(b) due to the shrinked spectrum compared to Si(111). The peak labeled 2LTO originates from a second-order process including the LTO phonon at the Γ point. The other two features are from other high symmetry point of the BZ [91]. Note that at the L point the degeneracy of the optical branches at Γ is lifted and therefore two peaks are observed. Closely below the peaks from the L point, there are furthermore features that are related to the X point. Other peaks are due to combination modes, i.e., the combination of acoustic and optical phonons. The vibrational modes observed for Si(111) above the LTO phonon are very similar to the ones of Ge(111).

The Raman scattering efficiency differs from Si to Ge. The first-order Raman intensity of Si(111) at RT is higher by a factor of ≈12 than that of Ge for a laser wavelength of 488 nm (see also Ref. [96]).

The Raman spectra in Fig. 3.2(a) are plotted down to $0\,\mathrm{cm}^{-1}$ to illustrate the effect of the edge filter. Between the strongly attenuated laser line at 0 and $\approx 50\,\mathrm{cm}^{-1}$ the intensity vanishes and prevents the observation of modes in that region.

If the Si(111) and Ge(111) samples are cooled to LT, the 2TA structure will drop in both polarization configurations (see Sec. C). This is due to the fact, that the second-order intensity is much more temperature dependent than the first-order scattering. While at a given temperature for first-order processes the Raman intensity is proportional to $(n_{\mathrm{BE}}(\omega) + 1)$, the second-order intensity is proportional

to $(n_{\mathrm{BE}}(\frac{\omega}{2})+1)$ at the same temperature [61,97]. Furthermore, the FWHM of the LTO phonon will also decrease with temperature.

3.2. Clean semiconductor surfaces

The reconstructions of the clean surfaces of the semiconductors Si(111) and Ge(111), obtained after high temperature annealing, are Si(111)-(7×7) and Ge(111)-c(2×8), respectively [10,98,99]. The vibrational properties of both are of interest since the reconstruction introduces a lot of new modes with respect to the unreconstructed surfaces. Secondly, these surfaces are pre-stages for the adsorbate systems explained in the following and must therefore be distinguished in the Raman spectra. Although the Raman investigation of the Si(111)-(7×7) reconstruction by SRS took mainly place prior to the work of this thesis [100], it will be briefly discussed based on LT Raman spectra that were recorded later within this thesis.

3.2.1. Preparation of Si(111)-(7×7) and Ge(111)-c(2×8)

All samples are prepared in the mobile preparation chamber. Therefore, the considered surface systems are all prepared under similar conditions.

Highly doped semiconductor samples of Si(111) (n-type, dopant P, $\rho = 0.009-0.011\,\Omega\,\mathrm{cm}$) and Ge(111) (p-type, dopant B, $\rho = 0.05-1.3\,\Omega\,\mathrm{cm}$) are used as substrates, enabling heating by direct current. The samples are cut into rectangular pieces ($10.0\,\mathrm{mm} \times 2.5\,\mathrm{mm}$) and polished on the front side. A miscut of considerably less than $\pm 1°$ with respect to the ideal (111) surface is assumed. The Si(111) and Ge(111) substrates are cleaned *ex situ* by boiling in acetone and methanol or ultrasonic cleaning in acetone for several minutes. Afterwards the samples are loaded into the UHV chamber and degassed *in situ* for several hours at $T \approx 900\,\mathrm{K}$. During this procedure the pressure is below $p < 1 \cdot 10^{-9}\,\mathrm{mbar}$.

The Si(111) samples are heated several times in a flash annealing procedure to obtain the clean Si(111)-(7×7) reconstruction (see also Sec. F). Flash annealing comprises the fast heating to $T = 1550\,\mathrm{K}$ for 10 s, followed by a rapid temperature decline to $T = 1200\,\mathrm{K}$. The sample is then cooled slowly to RT.

To get the clean Ge(111)-c(2×8) reconstruction, the preparation of Ge(111) is different from the one of Si(111). The GeO_2 layer on the surface cannot completely removed by thermal heating due to stronger binding to the substrate than SiO_2 [101]. Therefore, the surface is sputtered by Ar^+ ions ($E = 1\,\mathrm{keV}$, $p \approx 1-2 \cdot 10^{-6}\,\mathrm{mbar}$) for 20 min and subsequently annealed at $T = 1100\,\mathrm{K}$ for ≈30 s with a slow cooling rate to RT (see also Sec. F). This procedure is repeated several times.

Both sample reconstructions are inspected after preparation to show a clear LEED pattern.

3.2.2. Raman spectroscopy results for Si(111)-(7×7)

The clean Si(111)-(7×7) surface shows a very complex surface reconstruction in contrast to the (1×1) reconstruction of the unreconstructed Si(111). Hence, the SUC is considerably enlarged. For the atomic structure the dimer-adatom-stacking fault (DAS) model by Takayanagi *et al.* is widely accepted [102].

It is interesting to note that the surface is metallic at RT, although the bulk is semiconducting [103,104]. This is due to the fact that the SUC contains an odd number of electrons. At low temperatures of some K, correlation effects become relevant and open an energy gap accompanied with a drop of the electronic conductance [104].

Atomic surface structure and LEED pattern of Si(111)-(7×7)

The SUC of the Si(111)-(7×7) reconstruction consists of two inequivalent triangular subcells as shown in Fig. 3.3(a). They differ in their stacking sequences and are accordingly termed faulted and unfaulted half. In contrast to the unfaulted subcell whose subjacent layers show a regular pattern, for the faulted half the topmost bilayer is reflected which results in a different orientation to the lower bilayers. Therefore, the fourth layer atoms are not visible in the faulted half in the topview of Fig. 3.3(a). Characteristic for this reconstruction are the circular corner holes centered around a DB in each corner of the rhomb. Between the corners dimerized Si atoms are located along the cell boundaries. Atop the first complete surface layer (complete aside from the corner holes) there are 12 adatoms, half of them near the corners of the subcells and the other half near the middle of the edges. Additionally, six restatoms are located in the first layer. The atoms in the corner hole, the Si adatoms, and the Si restatoms all have DBs. However, the amount of 19 DBs of the Si(111)-(7×7) surface is considerably lower than the 49 DBs of the unreconstructed Si(111) surface [100].

The Si(111)-(7×7) surface reconstruction belongs to the point group C_{3v} [105]. The SUC is invariant under rotations of 120° around the corner hole. Furthermore, there are three vertical reflection planes all crossing the corner hole position.

A typical LEED pattern of the Si(111)-(7×7) surface is shown in Fig. 3.3(b). Together with surface-induced LEED spots, the spots of the (1×1) surface, which stems from the topmost bulklike layers of the substrate, are clearly resolved. Between the (1×1) spots there are six equidistant spots that divide the distance into seven parts. The observed spot pattern varies with electron energy. Clearly separated and resolved (7×7) spots indicate a good surface quality. A low background intensity is a further evidence for a well-ordered surface.

Surface Raman spectra of Si(111)-(7×7)

Due to the surface reconstruction, new Raman peaks appear in the Raman spectra in contrast to the unreconstructed surface. In Fig. 3.4, the polarization-dependent spectra of the Si(111)-(7×7) reconstruction for $z(xx)\bar{z}$ and $z(xy)\bar{z}$ polarization

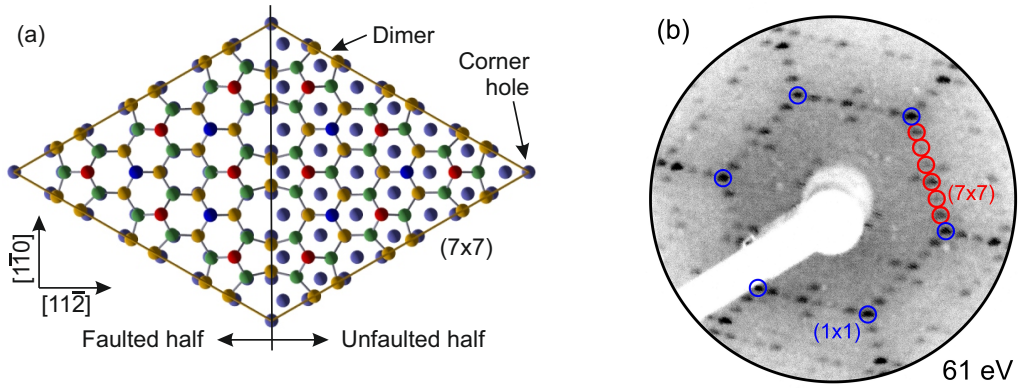

Figure 3.3.: Depiction of (a) the atomic surface structure and (b) the LEED pattern of the Si(111)-(7×7) surface reconstruction. Red colored Si atoms are atop of the first complete layer. The restatoms are marked in blue. The LEED pattern was recorded at RT and with an electron energy of 61 eV. Structural data adapted from Ref. [106].

configuration are shown for LT. Additionally, the spectra of the unreconstructed Si(111) surface are also shown for reference (see also Fig. 3.2(a) for comparison).

The first peak in Fig. 3.4 that can be clearly attributed to the Si(111)-(7×7) surface is observed at 62.4 cm^{-1}. It appears only in $z(xx)\bar{z}$ polarization and was identified with a backfolded RW by HAS [107]. The RW is folded by in-plane and out-of-plane reciprocal vectors in the sagittal plane. Due to the backfolding the RW has a frequency at the $\bar{\Gamma}$ point of the SBZ that is high enough to be detected by SRS. A further peak centered at 99.2 cm^{-1} fits also very well in the scenario of backfolded RWs. In accordance with the HAS measurements it is attributed to a second folding of the RW. These experimental results are also in good agreement with theoretical calculations. In a MD study, an oscillation with a rigid-body in-plane translation elongation pattern with a frequency of ≈60 cm^{-1} was predicted and is associated with the measured RW [105]. Furthermore, there is a calculated rigid-body rotation mode at 80 cm^{-1} that might be identified with the mode at 99.2 cm^{-1} in the Raman spectra. In Ref. [108], similar values for the RWs (60 – 100 cm^{-1}) were found by total-energy calculations.

The vibrational modes above approximately 100 cm^{-1} are considered to be of optical character [100]. A prominent group of three peaks is found in the Raman spectra with $z(xx)\bar{z}$ polarization located at 117.6, 130.0, and 141.0 cm^{-1}. According to calculations, the Raman intensity of this group can be mainly attributed to an in-plane wagging mode of the adatoms and atoms in the first layer (≈120 cm^{-1} [105] as well as 113 and 137 cm^{-1} [108]). Above the group of three peaks there is another double group that is observable in both polarization configurations. These modes are at 179.5 and 189.4 cm^{-1} and only appear in the LT spectra. At higher

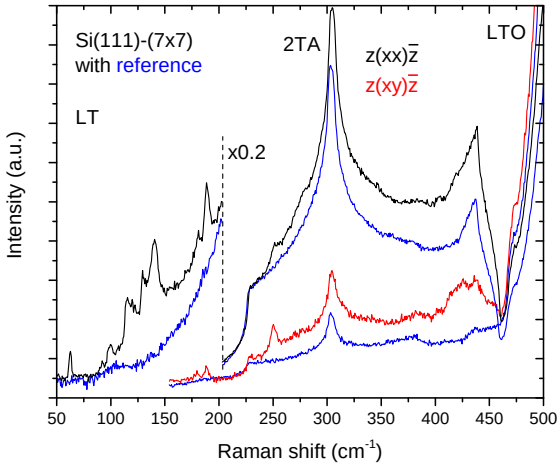

Figure 3.4.: Raman spectra of the Si(111)-(7×7) surface reconstruction at LT. Both polarization configurations are shown together with the unreconstructed reference surface of Si(111). Note the additional Raman peaks that are induced by the surface reconstruction.

frequencies, a peak at 252.6 cm^{-1} in the $z(xx)\bar{z}$ spectrum is clearly visible, but is much more distinctive in the $z(xy)\bar{z}$ spectrum. Only a small bump in the Raman spectrum with parallel polarization configuration points to a mode at 277.1 cm^{-1}, which is ascribed together with the previous peak at 252.6 cm^{-1} to a mode mainly located at the adatoms [109]. The frequency range 220 – 280 cm^{-1} in the MD calculations of Ref. [109] depends on the localization of the adatoms near a corner hole or near edge-center sites. Furthermore, both a HREELS experiment and theoretical investigations found also modes at ≈240 cm^{-1} that are attributed to adatom movement [24,105]. The modes with the highest frequencies are found in the region of the 2TA(W) of bulk Si(111). A broad feature is located at 421.4 cm^{-1} that is clearly observed in $z(xy)\bar{z}$ polarization. The eigenmode at 421.4 cm^{-1} is considered as collective mode in which the adatoms as well as the layers underneath take part. The calculated frequency of 417 cm^{-1} of Ref. [109] agrees well with the experimental value. It is followed by a weak feature at ≈455 cm^{-1} that is allusively observed in the $z(xy)\bar{z}$ Raman spectrum but is not clearly resolved. All Raman peaks together with theoretical results are summarized in Tab. 3.1.

Similar surface Raman spectra were presented in Ref. [100] (for RT and LT) and Ref. [110] (for $T = 120\,\mathrm{K}$). However, in the Raman spectra shown here additional modes are observed in comparison with the previously presented data. The peaks at 99.2, 179.5, and 189.4 cm^{-1} were not found in previous Raman measurements. This is most likely due to the lower temperature of the spectra shown in Fig. 3.4. This holds especially for the double peak (179.5 and 189.4 cm^{-1}) that is also not observed in recent RT Raman measurements. The peak at 460.6 cm^{-1} described in Ref. [110] is attributed to the weak feature at ≈455 cm^{-1}. All other Raman peaks

Table 3.1.: Vibrational peak frequencies (in cm^{-1}) of the Si(111)-(7×7) reconstruction. The SRS results for LT and $z(xx)\bar{z}$ polarization configuration are presented in this thesis. The other SRS data (Col. 1 – 2) for RT are adapted from Ref. [100] and for $T = 120\,K$ from Ref. [110]. The theoretical results are taken from Refs. [105,108,109]. The assignments are listed in the last column.

SRS			Theory	Assignment
RT	120 K	LT		
62.5	61.1	62.4	60 – 100	RW
		99.2		
115.3	114.9	117.6	110 – 140	In-plane wagging modes
130.0	129.1	130.0		
136.1	136.5	141.0		
		179.5		
		189.4		
250.9	250.9	252.6	220 – 280	Localized at adatomic sites
	270.4	277.1		
420.0	424	421.4	400 – 460	Collective modes
	460.6			

are in very good agreement. This is also true for their polarization configurations. The frequency differences of some cm^{-1} can be attributed to the different Raman setups that were used and to different excitation wavelength. This results sometimes in unusual frequency shifts with temperature, which are considered as artifact in this context. These additional Raman data are attached to Tab. 3.1.

3.2.3. Raman spectroscopy results for Ge(111)-c(2×8)

The clean Ge(111)-c(2×8) surface is, compared to the Si(111)-(7×7) surface, less complex and has a smaller SUC. The widely accepted structural model was proposed by Becker *et al.* based on STM measurements [111,112]. Prior to exact structural determination, the SUC and periodicity was determined to be c(2×8) by LEED investigation [98].

In addition to the structural surface configuration, the vibrational properties of the surface atoms were subject of theoretical and experimental investigations. Theoretically, the vibrational properties of Ge(111)-c(2×8) were investigated in a first-principles MD study which is based on local density functional calculations [113]. The calculations are performed for the $\bar{\Gamma}$ point of the SBZ and another high symmetry point. Furthermore, HAS measurements revealed several phonon modes

and their dispersion [30]. However, RS measurements do not exist for the this surface reconstruction.

Previously, a different crystal surface plane of Ge, i.e., the Ge(001) surface, was also investigated by SRS [114]. For this surface, several surface reconstructions occur in dependence of the temperature. At LT, a c(4×2) reconstruction appears, while at RT the reconstruction is changed to p(2×1)/c(4×2). In contrast to the ordered first one, the latter remains disordered due to the coexistence of two reconstructions. The reconstructions are crucially influenced by buckled Ge dimers on the surface, that are antiferromagnetically ordered and execute thermally driven flip-flop motions. The Raman spectra changed upon cooling and revealed thus the expected phase transition. Furthermore, the Raman spectra were compared to calculations of the phonon frequencies for p(2×1) as well as to corresponding displacement pattern. However, for the p(2×1) reconstruction only non-decaying surface phonon states at the SBZ boundaries were predicted and were therefore not accessible with SRS [110]. The required mechanism for backfolding was discovered in the dimer motion. The frequency of the dimer motion also explained different observations in experimental techniques with different time resolutions. This aspect will be resumed in Sec. 3.4.

Atomic surface structure and LEED pattern of Ge(111)-c(2×8)

The surface structure of Ge(111)-c(2×8) is characterized by two additional Ge adatoms per primitive SUC as depicted in Fig. 3.5(a). These adatoms are on T_4 positions. Furthermore, there are two so-called restatoms, which are part of the first layer but are shifted with respect to their bulk positions. Also Ge atoms in lower layers are displaced to new equilibrium positions [113]. The adatoms saturate DBs at the surface. In Fig. 3.5(a), the primitive SUC as well as the c(2×8) SUC are marked. Note that the number of enclosed atoms by the SUCs differs by a factor of 2.

Theoretical as well as experimental results revealed that the adatoms and the restatoms are not equivalent [115,116]. This is not apparent in the structural model shown in Fig. 3.5(a). The inequality of the Ge atoms concerns their structural and electronic properties. This implies that the Ge(111)-c(2×8) reconstruction has no point symmetry operations, i.e., especially no mirror planes, and prevents the application of group theoretical considerations. Which, in turn, does not mean that the Raman modes show no polarization properties. A fascinating question in this context is: how distinct must a distortion of the atomic lattice or the electronic states be to influence the symmetry properties and the vibrational properties considerably? The discussion below will readopt to this question.

The LEED pattern of Ge(111)-c(2×8), as shown in Fig. 3.5(b), is a superimposition of three c(2×8) domains. The LEED spots between the (1×1) spots can be attributed to different domains, like schematically indicated by the differently colored circles (green, red, and yellow). This identification can be repeated for all

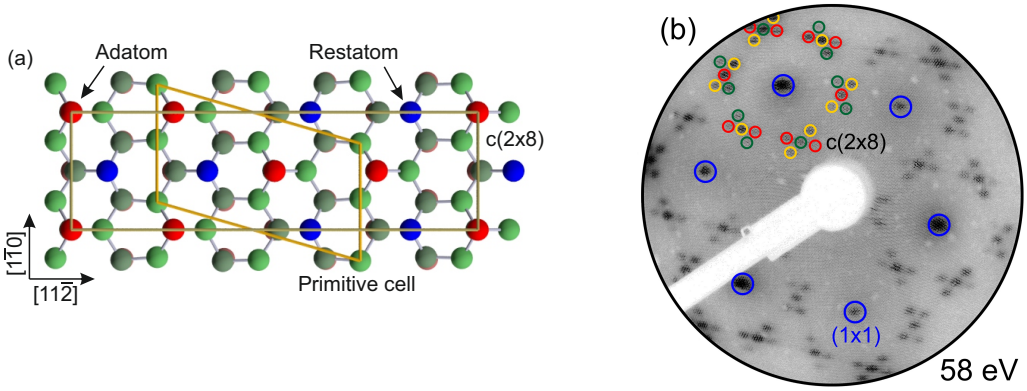

Figure 3.5.: Depiction of (a) the atomic surface structure and (b) the LEED pattern of the Ge(111)-c(2×8) surface reconstruction. The LEED pattern was recorded at RT and with an electron energy of 58 eV. The spots marked by green, red, and yellow circles indicate the three different domains. Structural data adapted from Ref. [113].

spot configurations that are shaped like a St. Andrew's cross. The surface domain bases are rotated by 120° with respect to each other.

Surface Raman spectra of Ge(111)-c(2×8)

In Fig. 3.6, the Raman spectra of Ge(111)-c(2×8) are depicted for both polarization configurations $z(xx)\bar{z}$ and $z(xy)\bar{z}$ at RT. Included are reference spectra of unreconstructed Ge(111) for comparison. Although new Raman peaks appear due to the reconstructed surface, the essential features of bulk Ge(111) are still observable (see also Fig. 3.2(b) for comparison). The shaded area in Fig. 3.6 marks the surface intensity that originates from the reconstructed surface. The difference between both spectra is shown in Fig. 3.7 for LT. Due to the lower temperature the width of the peaks reduces and some features are better resolved.

In Fig. 3.7, the most distinctive feature in the surface Raman spectra of Ge(111)-c(2×8) at LT is the peak at 121.7 cm^{-1}. It is strongly parallel polarized since only a small hump is visible in the $z(xy)\bar{z}$ spectrum. Due to the small FWHM value, a flat phonon dispersion in the vicinity of the $\bar{\Gamma}$ point of the SBZ is expected. This is in line with HAS experiments, which observed an optical vibrational mode with a flat dispersion at that frequency [30]. Moreover, the MD calculations ascribed this peak to vibrations of the Ge adatoms, although the measured intensity does not fully coincide with the calculated PDOS [113]. Since all three methods agree very well on the existence and frequency of this peak, this makes the peak at ≈120 cm^{-1} to the best documented and prominent one of Ge(111)-c(2×8). Besides, the spectra are naturally split in the following into parts below and above this peak. In Tab. 3.2, the SRS data for RT and LT are compiled with the results of the MD calculations and HAS measurements.

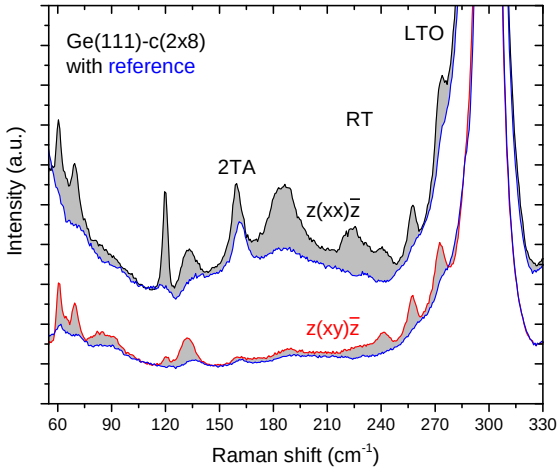

Figure 3.6.: Raman spectra of Ge(111)-c(2×8) at RT for the polarization configurations $z(xx)\bar{z}$ and $z(xy)\bar{z}$. The spectra of the unreconstructed Ge(111) surface is shown as a reference in blue. The shaded area is attributed to reconstruction-induced changes and yields the surface intensity.

Turning to the spectral region below 120 cm^{-1}, one sees a series of closely occurring peaks down to about 60 cm^{-1}. With the aid of HAS it is possible to relate these peaks to RWs. The RWs must be backfolded to be observable in SRS (cf. Sec. 2.1). Lobo *et al.* applied a backfolding into a (2×2) periodicity, which results in two RWs [30]. The one with lower frequency is the outcome of folding by in-plane and out-of-plane reciprocal vectors and hence doubly degenerate, while the other one with higher frequency is only folded out-of-plane. Focusing on the four most distinct Raman peaks, the SRS data can be interpreted accordingly. The peaks at 61.6 and 83.6 cm^{-1} are identified with the two RWs mentioned above. Therefore, both peaks are labeled as RW in Fig. 3.7. Note their appearance in different polarization configurations which might be a sign for different origin. The MD calculations predicted a mode, originating from adatoms as well as from restatoms, at the same frequency as the lower RW. Furthermore, a mode that results from restatom movement is predicted at ≈100 cm^{-1}, which might be the counterpart for the higher RW. For the latter RW, the agreement is not as good as for the first mode. The most intense mode in that region is located at 69.9 cm^{-1} and is marked by $*$ in Fig. 3.7. It is associated with a feature of unknown origin appearing in HAS, that is located between the two RWs. Additionally, there are further small Raman peaks observed at 64.9 and 77.3 cm^{-1} that have no equivalents in HAS measurements or MD calculations. Although the frequency of 77.3 cm^{-1} matches better with the mode labeled with $*$ in HAS (see Tab. 3.2), an assignment as made above seems more probable due to intensity considerations. Also, the higher RW is superimposed with a broad background. This results in a RT frequency value which is higher

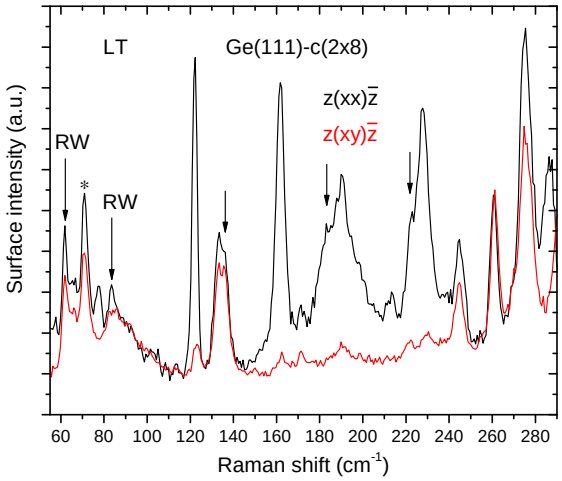

Figure 3.7.: Surface Raman spectra of Ge(111)-c(2×8) at LT for polarization configurations $z(xx)\bar{z}$ and $z(xy)\bar{z}$. The arrows indicate double peak structures. For further labels see explanation in the text.

than that at LT and this unusual temperature shift is thus an artifact due to this background. In HAS, two further low-frequency vibrational modes were observed. However, they are in a frequency range that is not accessible by SRS.

Above 120 cm^{-1} a double peak structure appears at ≈135 cm^{-1} as indicated by an arrow in Fig. 3.7. In the $z(xy)\bar{z}$ spectrum the two maxima at 132.1 and 135.4 cm^{-1} are clearly resolved. The latter one matches quite well with MD predictions and is ascribed to adatom movement on the surface. The appearance of two close-lying peaks might be a result of the inequivalence of the Ge adatoms discussed earlier. Neither of the two peaks was observed in HAS. The modes observed at 161.3 and 189.7 cm^{-1} together with the already mentioned peak at 121.7 cm^{-1} are all identified as optical surface phonons by HAS. While the mode at 161.3 cm^{-1} can be related to an adatom mode predicted by theory, the peak at 189.7 cm^{-1} results from restatoms and other atoms in that layer. In low-frequency vicinity of the latter peak there is a shoulder appearing at 182.4 cm^{-1}. Its existence is supported by inspection of the $z(xy)\bar{z}$ spectrum. For another double peak at 221.5 and 227.6 cm^{-1}, as also distinguished in the $z(xy)\bar{z}$ spectrum, only the first one finds a counterpart in the PDOS calculated for the restatoms. The range above ≈200 cm^{-1} are not accessible for HAS. The distinct Raman peak at 244.1 cm^{-1} is observed in the Raman spectra with both polarization configurations.

At the low-frequency edge of the LTO phonon of bulk Ge(111) there are intense Raman peaks at 260.2, 274.8, and 285.7 cm^{-1}. Interestingly, the former two are observed in both polarization configurations, while the latter one is only observed in the spectrum with parallel polarization. As mentioned in Sec. 3.1, the degenerate LTO phonon splits toward the BZ edges, e.g., the X and L point of the BZ, into a

Table 3.2.: Vibrational peak frequencies (in cm^{-1}) of the Ge(111)-c(2×8) reconstruction. The SRS results for RT and LT are tabulated for $z(xx)\bar{z}$ polarization configuration. The theoretical results from MD simulations are based on local density functional calculations (MD-LDF) [113]. The listed frequencies are attributed to contributions from the adatoms (AA) and from the restatoms and atoms in the first complete layer (RA). The data from HAS are also given for RT and $T = 170\,K$, which yields similar results [30]. The mode types according to HAS are labeled as optical surface phonon (O) and backfolded RW. The mode marked by $*$ is identically indicated in Fig. 3.7.

SRS		MD-LDF		HAS	
RT	LT	AA	RA		Type
				35	
				44	
60.2	61.6	62	62	64	RW
64.4	64.9				
69.7	69.9	76	74	78	$*$
74.5	77.3				
88.2	83.6		101	89	RW
119.7	121.7	122		120	O
131.7	132.1				
135.6	135.4	135			
159.4	161.3	152		159	O
	171.5				
181.7	182.4				
187.9	189.7		189	186	O
	211.9				
219.3	221.5		221		
224.8	227.6				
239.5	244.1				
257.1	260.2				
272.3	274.8		276		
282.9	285.7				

LO and TO branch. Therefore, the Raman peaks appearing on the edge of the LTO phonon might be due to reconstruction-induced backfolding of bulklike phonon modes located near the surface [117,118]. The LO branch in bulk Ge declines indeed by ≈30 cm^{-1} at the X point with respect to the Γ point as observed by INS [119]. Similar, but less pronounced features are also observed in the surface Raman spectra of Si(111)-(7×7) (see Fig. 3.4).

The small peaks at ≈170 and ≈210 cm^{-1} are not clearly observed in the RT spectra and are therefore omitted for RT. However, the first one is an actual peak as can be seen in the $z(xy)\bar{z}$ spectrum at LT.

As pointed out above, the SUC of the Ge(111)-c(2×8) surface has no mirror planes. If one assumes hypothetically that the symmetry is not disturbed, the Ge(111)-c(2×8) reconstruction would belong to the 3D point group C_s (for further details see Sec. 3.3.3). Thus, Raman peaks would be only observed in $z(xx)\bar{z}$ or in $z(xy)\bar{z}$ polarization configuration. By keeping this in mind and reevaluating the surface Raman peaks found in the spectra of Fig. 3.7, one sees exclusively peaks in $z(xx)\bar{z}$ or in both polarization configurations. No peak is solely observed in $z(xy)\bar{z}$ polarization. The absence of peaks with pure $z(xy)\bar{z}$ configuration is not a definite criterion for exclusion of a mirror plane, but the assumed point group might be actually not applicable with respect to the mentioned results. However, the polarization properties of the peaks are very distinct and might be a hint that there are other hidden symmetries. A further evaluation is beyond the scope of this thesis.

3.3. Au-induced surface reconstructions on Si(111)

When Au is deposited on the Si(111) surface, several reconstructions and its mixtures can occur, depending on the temperature treatment and coverage [120]. This is depicted in the phase diagram for the Au/Si(111) system in Fig. 3.8. The denoted temperature specifies the annealing temperature after Au deposition. The reconstruction remains stable during the subsequent cooling to RT. If there are only small amounts of Au on the surface ($\theta_{Au} \lesssim 0.02$ ML), the (7×7) reconstruction of the clean Si(111) surface persists. For a Au coverage of $\theta_{Au} \simeq 0.65$ ML, the Au-(5×2)/Si(111) reconstruction is formed (see Sec. 3.3.3). This reconstruction is found without admixtures only in a small region in the phase diagram. If the Au coverage is decreasing or increasing, the (5×2) reconstruction is mixed with (7×7) and ($\sqrt{3} \times \sqrt{3}$) contributions, respectively. The sole Au-($\sqrt{3} \times \sqrt{3}$)/Si(111) reconstruction appears for $\theta_{Au} \simeq 1.00$ ML and higher coverages (see Sec. 3.3.4). If the substrate is heated above ≈1050 K for a coverage of ≈0.65 ML, the Au-induced reconstruction disappears and the (1×1) reconstruction of the bulk substrate reappears. For coverages above and below, the (1×1) surface becomes observable already at lower temperatures of ≈975 K. Finally, it should be mentioned that for

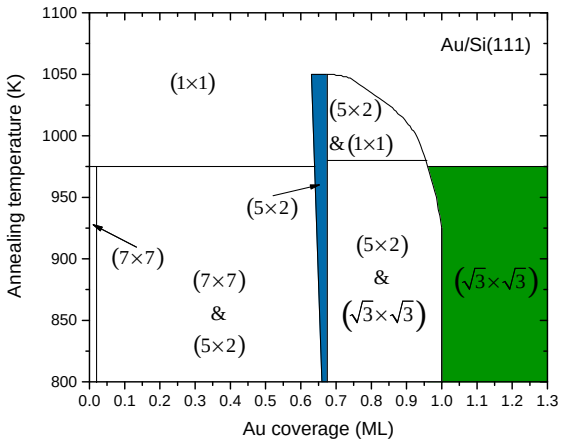

Figure 3.8.: Phase diagram of the surface adsorbate system Au/Si(111). With varying Au coverages and annealing temperatures different phases are obtained. The adsorbate reconstructions considered here are marked by different colors. Data adapted from Ref. [120].

Au coverages higher than 1 ML a (6×6) reconstruction was also reported [121–123].

The Au-(5×2)/Si(111) reconstruction generates quasi-1D Au chains, while the Au-($\sqrt{3} \times \sqrt{3}$)/Si(111) reconstruction forms a 2D pattern of Au trimers. The prefix "quasi" indicates that the chains are not strictly confined to 1D since they couple to higher dimensions, e.g., via the substrate [124]. Due to the confinement, interactions between the electrons become more relevant. These electronic correlations are considered in the next section with respect to the Au-reconstructed surfaces.

For many years, both reconstructions were investigated experimentally and theoretically as well as in joint studies. The Au-(5×2)/Si(111) surface was examined with special focus on its atomic and electronic structure for instance in Refs. [19,125–132]. More recently, new results of the effects of additional Si atoms on the Au chains were reported [133]. Also, the Au-($\sqrt{3} \times \sqrt{3}$)/Si(111) surface was investigated with the same respects, e.g., in Refs. [123,134–139]. Many of the previously mentioned reports treat the question of electronic correlations and related effects in these surface reconstructions. Therefore, this aspect is briefly addressed in the following section. The subsequent sections deal with the preparation of both reconstructions (5×2) and ($\sqrt{3} \times \sqrt{3}$) and their vibration-mode analysis.

3.3.1. Electronic correlations

In all solids, electrons interact with each other. However, the impact of this interaction is strongly system-dependent. Systems, in which these electron-electron interactions are relevant for a correct modeling of physical properties, are called correlated electron systems. The term for the Coulomb repulsion between electrons

that is part of the Hamiltonian of the Schrödinger equation cannot be disregarded and is inhibiting a direct solution [35].

On the other hand, when correlations are neglectable, a description by a one-electron picture is justified. Thus, an ensemble of non-interacting fermions can be considered within the ideal Fermi gas model [35]. Although this model provides some insights, it needs to be extended to include interactions. As a rule of thumb, an electronic system can be considered as correlated, if the Coulomb repulsion energy exceeds the kinetic energy of the electrons [140]. There are various approximations that take account of interactions. By considering specific interaction terms while neglecting others, these models highlight different effects in solids. Some relevant models are discussed briefly.

In the interacting case, a 3D system of fermions can be generally regarded as a Fermi liquid. Quasiparticles, i.e., modified electrons, with similar properties like bare electrons emerge while the effects of the interaction are absorbed into parameters like an effective electron mass. Most metals can be described as Fermi liquids. When interaction needs to be considered, an improved approximation is the Hartree-Fock model that is solved self-consistently. Here, an electron in the mean potential of all surrounding electrons and furthermore exchange contributions are considered. Some problems in the Hartree-Fock approximation can be circumvented by including screening of Coulomb interaction [35]. For numerical calculations, a very successful approach is DFT which is also capable of involving interactions (cf. Sec. 2.1). A special model is the Hubbard model which consists of electrons in a lattice (mainly 2D and 1D), which are allowed to hop between lattice sites (hopping matrix element t), but experience a repulsion if two electrons occupy the same site (Coulomb repulsion U). By varying the relative weight of the parameters t and U, a metal-insulator transition and other phenomena can be observed. Several extensions were introduced for the Hubbard model, e.g., models with more bands [35].

When the extension of a solid are reduced, correlation effects between electrons become more relevant. This can be understood in an intuitive picture with moving balls, where the balls are more likely to collide, if the dimensionality is lower than 3D [1]. For electron ensembles confined to 1D, the Fermi liquid properties break down and the system is better described as Tomonaga-Luttinger liquid (TLL). A characteristic phenomenon is that an excitation splits into two quasiparticles. They separately carry spin and charge of the electron (spin-charge separation) and have different group velocities [1,35]. For surface adsorbate systems, such a TLL behavior was found for the 1D Au chains generated on Ge(001) substrate [141].

The Fermi surface is an important concept in solid state physics and is strongly affected by changes in the dimensionality. It is defined as the constant energy surface in the reciprocal space that marks the maximum energy (Fermi energy E_F) up to which electron states are occupied in the ground state. In a conceptual picture for conduction electrons, the spherical Fermi surface in 3D is transformed to

a cylindrical surface in 2D and to two plates in 1D [142]. In 1D, only wave vectors with $\pm k_F$ are possible. Therefore, for ideal 1D conditions perfect Fermi surface nesting is realized [143].

A 1D chain of metal atoms would be in principle metallic since there is one electron per SUC resulting in a half-filled band. However, due to the so-called Peierls instability these systems become insulating below a specific temperature. This metal-insulator transition is evoked by a static periodic lattice distortion (PLD) which leads to a doubling of the SUC. The PLD is connected to a modulation of the charge density to a charge-density wave (CDW) [143]. This opens a gap at E_F which causes a lowering and raising of the energy of the occupied and unoccupied electron states, respectively [144]. The formation of the CDW and PLD is favored if the energy lowering of the electronic states exceeds the energy needed for the lattice distortion. The picture above describes electron-phonon interaction and is also connected with a Kohn anomaly [143]. This is an illustrative example for the interplay between the electron and lattice system that was introductory mentioned. For 2D systems, CDWs and PLDs can also appear, but are less pronounced [143]. In principle, the appearance of a Peierls instability and TLL physics exclude each other [141].

For the 1D Au chains of the Au-(5×2)/Si(111) reconstruction, metallic behavior is observed for temperatures from RT down to 20 K by IR spectroscopy [131]. Additionally, the spectroscopic results are combined with DFT calculations and reveal a half-filled electron band. Although the Au-(5×2)/Si(111) reconstruction exhibits (quasi-)1D Au chains, observation of TLL physics is unlikely which is in line with the fact that there is no phase transition reported [144]. The 2D Au pattern of the Au-($\sqrt{3} \times \sqrt{3}$)/Si(111) surface is also metallic due to a half-filled surface band [145].

Types of electrons like the ones considered above, that can move nearly free through a solid, are considered as itinerant and delocalized. They can contribute to electric current. Apart from itinerant electrons there are also localized electrons. Examples for localized electrons might be the $4f$ electrons of the rare-earth elements (see Sec. 2.2). Electronic correlations can occur for both types of electrons.

3.3.2. Preparation of Au reconstructions on Si(111)

Onto the clean Si(111)-(7×7) surface, the required amount of Au is deposited to get the desired reconstruction. For the Au-(5×2)/Si(111) reconstruction, ≈1.5 ML of Au are deposited, while the substrate is held at 950 K. Annealing at $T = 1050$ K ensures desorption of excess Au atoms and self-assembly.

Instead, the Au-($\sqrt{3}\times\sqrt{3}$)/Si(111) reconstruction is formed at higher Au coverages on the Si(111)-(7×7) surface. Therefore, Au coverages of 1.0 ML and above are deposited onto the substrate that is heated to 800 K. The samples are annealed subsequently at $T = 900$ K, which also allows excess Au atoms to desorb.

Both reconstructions are prepared from a similar starting point, i.e., similar Au deposition, but differ in the necessary annealing temperature, that decides which reconstruction is established.

Finally, the quality of each reconstruction is checked by LEED. Through the analysis of the LEED patterns a mixing of the reconstructions can be excluded.

3.3.3. Raman spectroscopy results for Au-(5×2)/Si(111)

The chain-like atomic structure of the Au atoms on the Si(111) surface, forming a (5×2) reconstruction, was under debate for a long time, despite numerous experimental and theoretical investigations, and was recently enriched by new proposals [128]. There were several models suggested possessing quasi-1D Au chains. A model for a Au coverage of 0.6 ML was suggested by Erwin, Barke, and Himpsel and is therefore called Erwin-Barke-Himpsel (EBH) model [126]. This model is the result of a first-principles study and its predictions are in accordance with STM and angle-resolved photoemission spectroscopy (ARPES) measurements. A different model with also 0.6 ML was proposed by Abukawa and Nishigaya based on reflection high-energy electron diffraction (RHEED) measurements [127]. The resulting Abukawa-Nishigaya (AN) model features Y-shaped Au structures and Si adatoms and is thereby designed to explain STM observations. But due to energetic instabilities in DFT simulations in combination with incongruity with RAS results, it was dismissed by Hogan *et al.* [19]. Furthermore, Seino and Bechstedt also rejected the AN model because of instabilities in *ab initio* calculations [129]. A further model, developed by Kwon and Kang with a Au coverage of 0.7 ML was proposed for better agreement with STM images [128]. The so-called Kwon-Kang (KK) model is energetically more stable than the EBH model with an energy gain of 0.92 eV per (5×2) SUC. The KK model was favored in a surface x-ray diffraction (XRD) study [130] as well as by DFT calculations for core-level shifts in x-ray photoemission spectroscopy (XPS) [146] and for spectra in RAS [132].

Therefore, the subsequent analysis of the surface Raman spectra of the Au-(5×2)/Si(111) reconstruction focuses only on the EBH and KK model. With the aid of first-principles calculations, the experimental vibrational eigenmodes are compared to the predictions of both models to obtain the favored one [34]. The emphasis of Ref. [34] is on surface Raman spectra at RT which are recorded with an excitation wavelength of 660 nm. To enrich the discussion, additional surface Raman spectra are presented here that are obtained at LT and with a different wavelength of 488 nm.

Atomic surface structures and LEED pattern of Au-(5×2)/Si(111)

According to the atomic structure of the EBH model, shown in Fig. 3.9(a), the Au atoms are assembled in two chains in $[1\bar{1}0]$ direction. One chain consists of single Au atoms in a row, while the other one is a dimerized double Au row. Between the Au

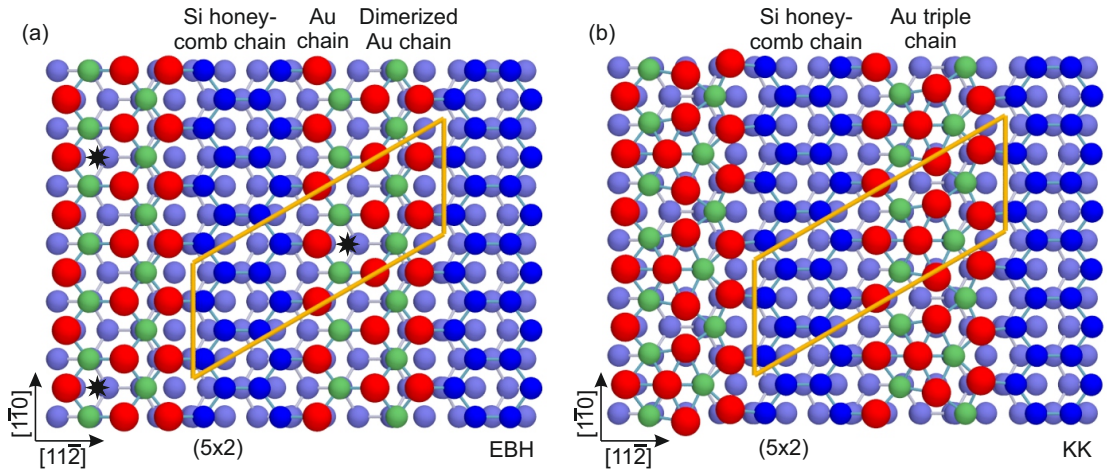

Figure 3.9.: Atomic surface structure models of the Au-(5×2)/Si(111) surface. Depicted are the (a) EBH and (b) KK model. In both figures, Au atoms are colored in red and Si atoms are marked in green and blue. For the EBH model the black stars indicate additonal Si adatoms that are responsible for doubling of the SUC to a (5×2) periodicity. Structural data adapted from Ref. [34].

rows, a Si honeycomb chain is located. The structure, as it is shown in Fig. 3.9(a), has only a (5×1) periodicity, whereas experimental results yield a (5×2) periodicity, e.g., in LEED [147]. This problem is overcome by additional Si adatoms between the Au rows in a (5×4) pattern, which were experimentally confirmed for this reconstruction [126]. Nearest-neighbor Au atoms of the double chain are slightly moved towards the Si adatoms which induces an antiferromagnetically ordered tilt of the Au dimers. Overall, this results in the desired (5×2) periodicity. This slight tilt is not considered in the calculations and is therefore also omitted in Fig. 3.9(a).

The KK model is largely similar to the EBH model, but has one additional Au atom in the (5×2) SUC. It is depicted in Fig. 3.9(b). With the additional Au atom, it is more appropriate to consider the Au rows as a Au triple chain. The Si honeycomb chain persists like in the previous model. In contrast to the EBH model, the KK model exhibits an intrinsic (5×2) periodicity. In Ref. [128], the impact of additional Si adatoms on the surface is also considered. These Si adatoms are believed to be present in small amounts (coverage of ≈0.025 ML) even at well prepared surfaces [132,133,148,149]. It was found that the surface is split into parts with no Si adatoms and parts with a coverage of ≈0.05 ML.

In Fig. 3.10, a typical LEED pattern of the Au-(5×2)/Si(111) reconstruction is shown. The distances between the (1×1) spots are divided into five parts by superstructure spots. However, not all groups of intermediate spots appear equally.

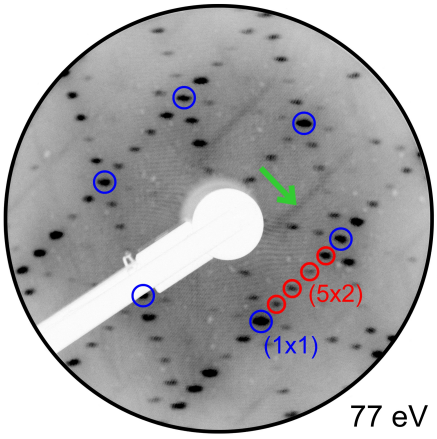

Figure 3.10.: LEED pattern of the Au-(5×2)/Si(111) surface at RT. The LEED pattern was recorded with an electron energy of 77 eV. Note the green arrow indicating streaks that are responsible for the doubling of the surface periodicity.

Furthermore, there are streaky features, mainly in one direction, that are responsible for the doubling of the periodicity as indicated by a green arrow in the LEED pattern. Both observations are consistent with the assumption of three domains, which are rotated by 120° with respect to each other and are present in different abundance. Since these streaks and intermediate spots are observed primarily in one direction, it is assumed that one domain predominates. Nevertheless, there are small contributions from the other domains.

Symmetry properties of Au-(5×2)/Si(111)

The Au-(5×2)/Si(111) surface reconstruction is highly anisotropic with respect to the main crystal directions $[1\bar{1}0]$ and $[11\bar{2}]$. This strongly affects the symmetry group of the surface since the only symmetry operation is a glide plane. These glide planes are reflections on mirror planes combined with translations [44]. Therefore, the Au-(5×2)/Si(111) reconstruction belongs to the 2D space group $p1g1$, which corresponds to the 3D point group C_s. This group has two nondegenerate irreducible representations A′ and A″, which gives rise to two Raman tensors [17]:

$$\mathcal{R}^1_{\mathrm{A}'} = \begin{pmatrix} a & 0 \\ 0 & b \end{pmatrix}, \tag{3.1}$$

$$\mathcal{R}^1_{\mathrm{A}''} = \begin{pmatrix} 0 & c \\ c & 0 \end{pmatrix}. \tag{3.2}$$

In contrast to the Raman tensor given in Eq. (2.20), the Raman tensors here are already reduced in z direction due to the restriction to the surface. This has no

influence on the predicted polarization properties and Eq. (2.21) is still applicable. Thus, modes that transform according to A′ are observable in parallel polarization configuration $z(xx)\bar{z}$. On the other hand, modes with A″ symmetry are detectable in crossed polarization configuration $z(xy)\bar{z}$.

Surface Raman spectra of Au-(5×2)/Si(111)

The unpolarized surface Raman spectrum of Au-(5×2)/Si(111) at LT is shown in Fig. 3.11(a). The reconstruction-induced Raman intensity is decomposed by fitting with Voigt profiles. The polarization properties of the peaks can be extracted from the polarized surface Raman spectra of Fig. 3.11(b). Both figures are therefore discussed together. Note that all Raman peaks of the $z(xu)\bar{z}$ spectrum find counterparts in the separately recorded polarized spectra ($z(xx)\bar{z}$ and $z(xy)\bar{z}$). The Au chains are oriented in y direction in the Raman experiments and the polarization of the incident laser light is perpendicular to the Au chain direction.

The first peak in the Raman spectra is located at 48.2 cm^{-1} and is observed in $z(xx)\bar{z}$ and $z(xy)\bar{z}$ configuration. The symmetry properties are thus specified as A′ and A″. At 60.4 cm^{-1}, there is another rather broad peak that has a small low-frequency shoulder centered at 55.1 cm^{-1}. The main peak is more prominent in $z(xy)\bar{z}$ polarization, while the shoulder is resolved in both configurations. The following mode at 69.0 cm^{-1} is mainly observed in $z(xy)\bar{z}$ and has therefore A″ symmetry. A further peak structure can be clearly distinguished as consisting of two peaks at 76.2 and 81.0 cm^{-1}. The adjacent peak, only observed in $z(xy)\bar{z}$ polarization, is located at 89.6 cm^{-1}. At higher frequencies, the peaks at 102.0 and 115.1 cm^{-1} as well as the smaller peak at 129.0 cm^{-1}, which can be clearly identified in the $z(xx)\bar{z}$ spectrum, are all only observed in parallel polarization configuration. After a dip in the Raman intensity at about 140 cm^{-1}, a group of four prominent peaks appears. The first one at 150.1 cm^{-1} is in the edge of the following broad peak at 165.3 cm^{-1}. While the polarization configuration of the first peak is hard to discriminate (presumably A′), the second one seems to be Raman active in both configurations. The most intense double peak is observed with maxima at 180.2 and 185.4 cm^{-1}. The first one is observed in both configurations, while the second one only appears in the $z(xy)\bar{z}$ Raman spectrum.

The inset in Fig. 3.11(a) shows a mode that appears at the high-frequency edge of the 2TA(X) of the Si(111) substrate. The peak is located at 335.8 cm^{-1} and is observed in both polarization configurations $z(xx)\bar{z}$ and $z(xy)\bar{z}$. The dip at about 300 cm^{-1} results from small intensity differences between the Raman spectra of the reconstructed and unreconstructed samples at the 2TA(X) structure of bulk Si. All peaks and their polarization properties are tabulated in Tab. 3.3.

Further surface Raman spectra of Au-(5×2)/Si(111) for RT and different excitation wavelengths are given in Refs. [34,88] of the author's publications. The obtained vibrational surface modes are listed together with the LT values in Tab. 3.3. The results presented in this thesis for $z(xx)\bar{z}$ and $z(xy)\bar{z}$ polarization are comparable

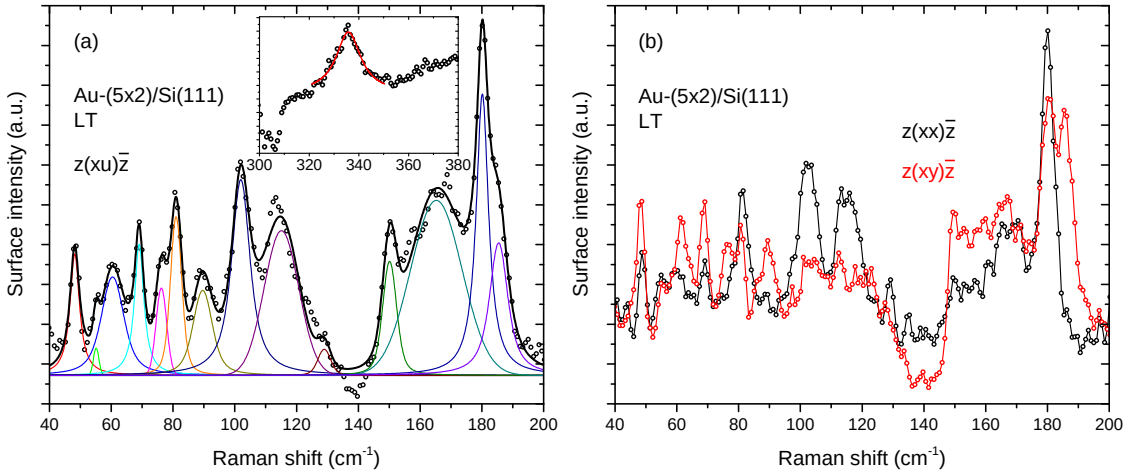

Figure 3.11.: Surface Raman spectrum of Au-(5×2)/Si(111) at LT for (a) $z(xu)\bar{z}$ polarization configuration and (b) for the polarization configurations $z(xx)\bar{z}$ and $z(xy)\bar{z}$. The $z(xu)\bar{z}$ spectrum is fitted with Voigt profiles to identify its constituent peaks. The inset shows a higher-frequent Raman mode recorded with the same parameters.

to the Raman spectra labeled with $z(yy)\bar{z}$ and $z(yx)\bar{z}$ in Ref. [34], respectively. A major difference between the LT and both RT Raman measurements are that many more peaks appear for LT. If the polarization properties of the modes are initially neglected, all RT vibrational eigenmodes find its counterparts in the LT spectra. The frequency values are in good agreement. The small discrepancies result from the different sample temperatures and to some extent from the different Raman setups with varying excitation wavelengths. Since at RT the peaks are generally broader, this naturally explains the occurrence of some additional weak peaks at LT, especially the ones located at edges of stronger peaks. Others might be affected by highly temperature-dependent Raman response. By comparing the Raman intensities in both polarization configurations, i.e., the surface phonon symmetry, the discrepancies between the spectra at different temperatures are larger. Except for one mode, the attributions to symmetry representations are not concordant. A reason for this might be the fact that the samples have different relative contributions of the three different possible domains and the RT spectra additionally were recorded with different laser wavelengths.

The surface Raman spectra with parallel polarization configuration presented in Ref. [34] show only Raman intensities if the polarization of the incident laser light is perpendicular to the Au chains. In contrast, for parallel polarization configuration whose polarization is also parallel to the chains there are no considerable Raman signals found. This contradicts the simplistic picture of Au chains as dipole antennas.

Table 3.3.: Vibrational peak frequencies (in cm^{-1}) of the Au-(5×2)/Si(111) reconstruction. The unpolarized SRS results for LT are presented in Fig. 3.11 of this thesis. The other SRS data (Col. 3 – 5) for RT are adapted from Ref. [34] together with the polarization symmetry and from Ref. [88], both of the author's publications. The results of the DFT calculations for the KK model are listed for comparison (see text and also Ref. [34]).

SRS					DFT	
$z(xu)\bar{z}$	Sym.		Sym.	$z(xu)\bar{z}$		Sym.
LT		RT		RT	KK	
		29	A″			
48.2	A′, A″	51	A′, A″	51	48	A′, A″
55.1	A′, A″				55	A′
60.4	A″	61	A′	61		
69.0	A″	69	A′			
76.2	A″				75	A″
81.0	A′, A″				81	A′
89.6	A″				88	A″
102.0	A′	106	A″	104	98	A′
115.1	A′				115	A′
129.0	A′			124	130	A′
150.1	A′					
165.3	A′, A″			168		
180.2	A′, A″					
185.4	A″					
335.8	A′, A″			333		

In general, ideal dipole antennas interact only with electromagnetic waves that are polarized parallel to their orientation and also only emit light with this polarization. Such a behavior was found by IR spectroscopy on the Au-(5×2)/Si(111) surface, where the transmittance decreases for polarization parallel to the Au chains [131]. Therefore, the Au chains cannot be considered as simple antennas with respect to the Raman mechanism upon irradiation with visible light. Apart from the aim of structural determination, the following theoretical calculations will also contribute to solve this discrepancy by qualitative considerations.

Comparison with first-principles calculations for Au-(5×2)/Si(111)

Theoretical calculations are necessary to decide whether the SRS data suits better with the EBH or KK model [34]. The calculations were performed within the DFT. To evaluate Eq. (2.12), the PBE formulation of the GGA was used. A

$(4 \times 12 \times 1)$ k-point mesh and a plane-wave cutoff energy of 500 eV were applied. Each calculated mode was artificially broadened with a Lorentzian function with a FWHM of 5 cm^{-1}. This eases the comparison of the calculated Raman spectra with the measured ones.

However, the comparison of experimental with theoretical results requires caution. For instance, the correct excitation energy needs to be chosen as well as band gap corrections of the DFT calculations are necessary. To allow for the underestimated band gap in Si, the electronic transition energy eigenvalues need to be shifted by 0.5 eV to higher energies. Technically, the experimental Raman spectra are compared to theoretical spectra calculated for exciting photons with an energy of 0.5 eV less [150]. Hence, for an experimental excitation with photons of 2.54 eV ($\cong$488 nm) the calculated spectra for 2 eV are used [33]. Furthermore, quasiparticles and excitonic effects were not considered in the calculations [34,150]. Another important factor are defects that are undoubtedly present at the experimental samples, but are usually not considered in calculations.

The calculated spectra discussed initially are adjusted to an excitation wavelength of 660 nm as used for recording of the Raman spectra at RT in Ref. [34]. The calculated Raman spectra are labeled according to the x and y direction that are defined like the directions in the experiments. Here, the spectra for the polarization configurations (xx), (yy), and (xy) are considered (cf. Eq. (2.22)). For the KK model, the calculations reveal eigenmodes at 56, 63, 71, and 78 cm^{-1} for polarization configuration (xx) that is perpendicular to the Au chains, i.e., A′ symmetry. All modes are mainly localized at the Au atoms. For crossed polarizations and parallel polarizations that are also parallel to the chains, no considerable Raman intensity was found [34]. In contrast to the KK model, the calculated Raman spectra of the EBH model show a much higher intensity for the polarization configuration (yy), that is parallel to the Au chains, than the other polarizations. Because of this, the RT Raman spectra are considered to support the KK model best. Yet, for the crossed polarization configurations neither of both models agree well with the measured spectra. The choice of the KK model is also in agreement with other experimental results as mentioned above.

For a different excitation laser wavelength, only the mode intensities vary in the calculations. The eigenfrequencies of the modes do not change. Therefore, the LT Raman spectra must be compared to calculated spectra for an effective excitation wavelength of 488 nm. The calculated Raman spectra for both models are shown in Fig. 3.12. By comparison of the calculated spectra for the KK model with the ones for a different wavelength in Ref. [34], one finds the intensity ratios between the polarization configurations essentially preserved. Instead, the ratios for the EBH model for (xx) and (yy) become comparable, while the spectra for (yy) prevail in Ref. [34].

In Fig. 3.12, the experimental LT Raman spectra are additionally included for comparison. The data can only be compared in the range $40-160\,\mathrm{cm}^{-1}$. Therefore,

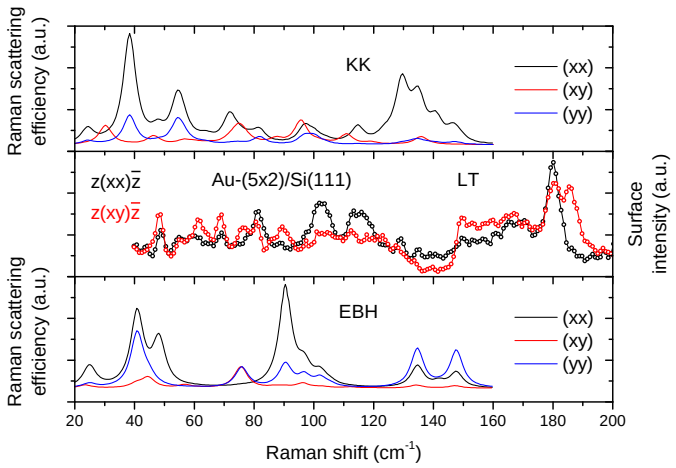

Figure 3.12.: Comparison of the calculated Raman scattering efficiency and the $z(xx)\bar{z}$ and $z(xy)\bar{z}$ surface Raman spectrum of Au-(5×2)/Si(111) at LT. The results for the structural models KK and EBH are depicted for polarization configurations (xx), (xy), and (yy). Calculation results are kindly provided by S. Sanna (cf. Ref. [34]).

the group of peaks above ≈140 cm^{-1} is not fully covered by the calculations. In the theoretical KK spectrum, a small hump at 48 cm^{-1} appears in the (xx) spectrum and a bit lower in the (xy) spectrum. A corresponding peak is observed in the experimental $z(xx)\bar{z}$ spectrum at 48.2 cm^{-1} and it seems that its associated peak in $z(xy)\bar{z}$ is also slightly shifted to lower frequencies. A more intense feature at 55 cm^{-1} can also easily attributed to an experimental peak at 55.1 cm^{-1}, but the intensities and polarization do not agree well. The next peak that finds a close counterpart is located at 75 cm^{-1} in the (xy) spectrum. Moreover, the polarization configuration is identical with the experimental Raman peak at 76.2 cm^{-1}. The frequency value of the calculated mode at 81 cm^{-1} is conform with an experimental Raman features at 81.0 cm^{-1}. A very small hump at 88 cm^{-1} in the (xy) spectrum, but still more intense than in parallel polarizations, is identified with the measured peak at 89.6 cm^{-1} with the same symmetry configuration. In the spectral region 90 – 120 cm^{-1}, two peaks in (xx) polarization configuration at 98 and 115 cm^{-1} are attributed to the two prominent measured Raman peaks at similar frequencies (102.0 and 115.1 cm^{-1}). However, the calculated spectra suggest more intensity in the (xy) configuration in that spectral range, which is not observed experimentally. The intense peak located at 130 cm^{-1} finds its counterpart in the much weaker measured peak at 129.0 cm^{-1}. The following cascade of calculated modes is not observed, but there is an adjacent feature (experimentally observed at ≈135 cm^{-1} in $z(xx)\bar{z}$) that is eligible even it is almost below the noise level. Now turning to the EBH model, the intense peaks in the (xx) spectrum appear in regions

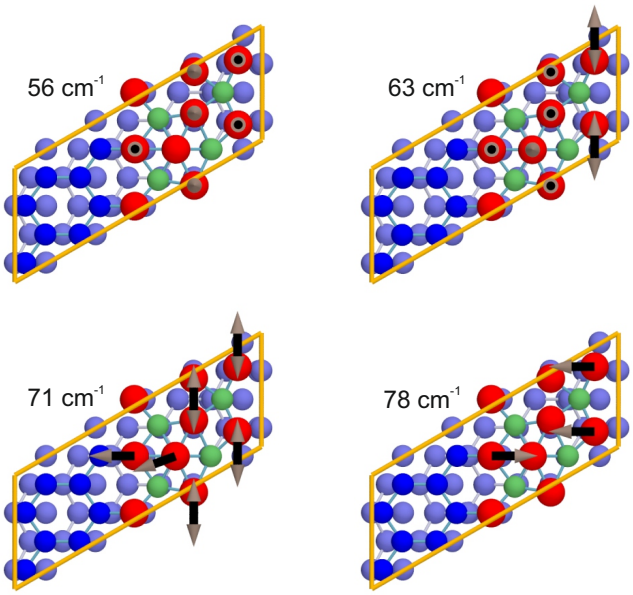

Figure 3.13.: Displacement patterns for the KK model of the Au-(5×2)/Si(111) surface system. Depicted are the most dominant phonon modes with frequencies of 56, 63, 71, and 78 cm^{-1}. Arrows with single heads indicate rigid translations, while arrows with double heads picture dimerization motions. Adapted from Ref. [34].

where predominantly Raman intensity in crossed polarization or no polarization is measured at all. Furthermore, the considerable intensity in the $z(xy)\bar{z}$ spectrum is not well described by the calculated scattering efficiency that almost vanishes in the (xy) spectrum, beside the peak at $\approx$75 cm^{-1}. Apart from this, the frequencies of the experimental Raman peaks at 48.2, 76.2, and 89.6 cm^{-1} find calculated equivalents that agree quite well. A drawback is, though, that the polarization configurations do not match. This detailed comparison leads to the conclusion that the KK model describes the SRS data overall better, even if there are some discrepancies. This result is also found for the RT Raman data. The relevant described modes of the KK model are included in Tab. 3.3 for comparison. The (yy) spectra of both models are shown for completeness, but cannot be compared to the LT SRS data.

Despite the many similarities, there are discrepancies between the calculations and the experiments that might have several reasons. The Si adatoms are neglected in the theoretical calculations of the EBH structural model which certainly influences the Raman spectra to some degree. This also holds for the KK model. Since the samples usually host more than one domain, especially the experimentally observed polarization properties of the Raman peaks might be altered. Moreover, multiple domains induce domain boundaries which enable the emergence of new surface

phonon modes. Unlike in STM measurements for instance, due to the relatively large laser spot in SRS no defect-free single domain area of the sample is selectable. The Raman spectra are therefore averages over a sample area with many variations. Additionally, there are the fundamental issues in the calculations that are already mentioned. Furthermore, on the basis of the theoretical results and the LT spectra, a phase transition seems unlikely, which is in accordance with literature.

Another outcome of the calculations are the eigenvectors of the vibrational modes. The corresponding displacement patterns of the vibrational eigenmodes are obtained within the frozen-phonon approach [34]. They are depicted for the preferred KK model in Fig. 3.13. The mode eigenvectors are independent of the excitation wavelength and reflect the mode symmetry. All illustrated modes are mainly localized at the Au atoms. For the modes with frequencies 56 and 78 cm^{-1}, the orientation of the displacement patterns of the Au atoms are primarily perpendicular to the Au chain direction. The displacement vectors for the first mode are oriented normal to the surface plane, while they are oriented in the surface plane for the latter mode. The other modes at 63 and 71 cm^{-1} exhibit perpendicular as well as in-plane displacements.

3.3.4. Raman spectroscopy results for Au-($\sqrt{3} \times \sqrt{3}$)/Si(111)

The Au-($\sqrt{3}\times\sqrt{3}$)/Si(111) reconstruction is different in many respects from the so far discussed Au-(5×2)/Si(111) surface. Instead of chain-like structures, the Au adatoms on the surface generate a 2D pattern that exhibits a SUC with a $(\sqrt{3} \times \sqrt{3})R30°$ periodicity. For the Au-($\sqrt{3}\times\sqrt{3}$)/Si(111) reconstruction, several structural models were considered to explain the experimental results [139]. Chester and Gustafsson proposed a model based on results from medium-energy ion scattering (MEIS) and Monte Carlo simulations [134,135]. It is labeled as twisted-trimer (TT) model, because three Au atoms form a trimer on the surface. Another model suggested by Ding *et al.* is referred to as conjugate honeycomb-chained-trimer (CHCT) model [136]. The structure, which is similar to the TT model, was derived from DFT calculations within the LDA. In combination with ARPES measurements, Zhang *et al.* developed the honeycomb-chained-trimer (HCT) model [137]. This model also has Au trimers, but they are connected to each other. The TT, CHCT, and HCT models all have a Au coverage of 1.0 ML. The main difference between these models is the orientation and size of the Au trimers. As fourth model, the H_3-missing-top-layer (H_3-MTL) model by Kadohira *et al.* has a lower coverage of $\frac{2}{3}$ ML and was tested by first-principles calculations [138]. The atomic structure of this model is much different since the Au adatoms on H_3 positions form hexagonal rings without a Au atom at the center. All these four models involve Si trimers that are generated by Si atoms in the first layer. Due to its low Au coverage, the H_3-MTL model does not match with experimentally obtained coverages and is thus dismissed, although it is a stable structure [33,138]. The HCT model is also rejected

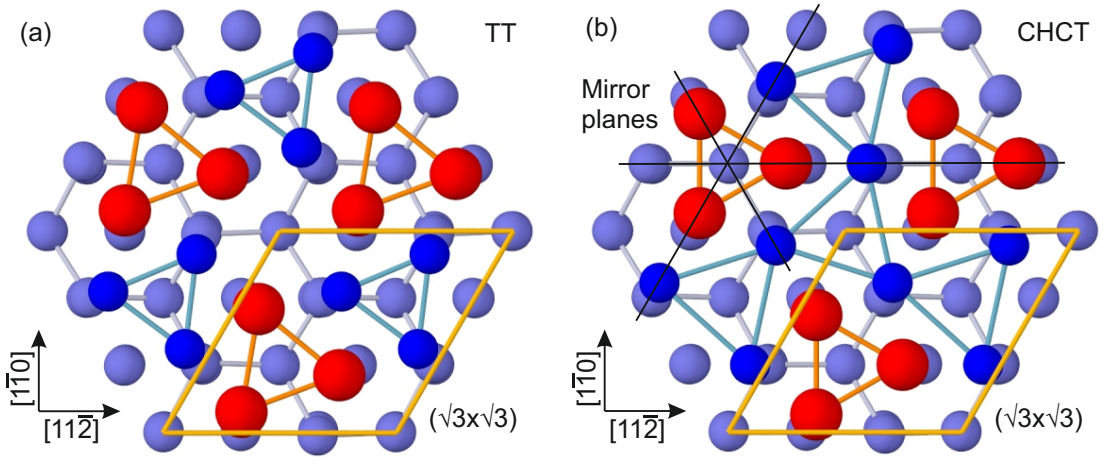

Figure 3.14.: Atomic surface structure models of the Au-($\sqrt{3} \times \sqrt{3}$)/Si(111) surface. Depicted are the (a) TT and (b) CHCT model. In both figures, Au atoms are colored in red and Si atoms are marked in blue. The mirror planes of the CHCT model are marked. Structural data adapted from Ref. [33].

since it is energetically located on a saddlepoint and therefore relaxes to the TT or CHCT model [33,139].

Hence, the following analysis of the surface Raman spectra of the Au-($\sqrt{3} \times \sqrt{3}$)/Si(111) reconstruction concentrates only on the TT and CHCT model. The experimental vibrational eigenmodes of the reconstruction are compared to first-principles calculations for both models to determine the most likely one [33].

Atomic surface structures and LEED pattern of Au-($\sqrt{3} \times \sqrt{3}$)/Si(111)

Both the TT and CHCT model have Au trimers whose Au atoms are located near H_3 positions. Both structural models are shown in Fig. 3.14. The Au atoms are on equal heights and thus the trimers are planar atop the surface with no corrugation. Like the Au atoms, Si atoms also form trimers in the top layer in both models. The crucial difference between both models is that the Au and Si trimers are oriented differently to the substrate and to each other. Thereby, the CHCT model has mirror planes, while the TT model has none. Additionally, the trimers of both models differ in size.

A typical LEED pattern of the Au-($\sqrt{3}\times\sqrt{3}$)/Si(111) surface is shown in Fig. 3.15. The extra spots in the LEED pattern form a rhomb like the (1×1) spots. The ratio between the sizes of the ($\sqrt{3} \times \sqrt{3}$) and the (1×1) rhomb yields a factor of $\sqrt{3}$. Furthermore, the shrinkage is combined with a rotation by 30°. This justifies the notation as $(\sqrt{3} \times \sqrt{3})R30°$.

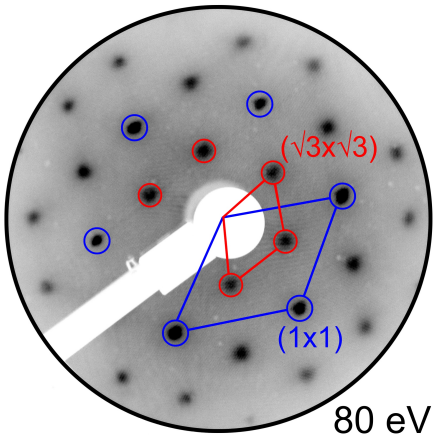

Figure 3.15.: LEED pattern of the Au-($\sqrt{3}\times\sqrt{3}$)/Si(111) surface at RT. The LEED pattern was recorded with an electron energy of 80 eV.

The LEED pattern of Au-($\sqrt{3}\times\sqrt{3}$)/Si(111) is clearly distinguishable from the one of Au-(5×2)/Si(111) (see Fig. 3.10), enabling a clear discrimination of the surface reconstruction. Thus, it allows the assessment of the purity of the reconstruction and an unambiguous assignment of the Raman spectra.

Symmetry properties of Au-($\sqrt{3}\times\sqrt{3}$)/Si(111)

The TT and CHCT model are associated with different 2D space groups. Due to the mirror planes, the CHCT structure belongs to $p31m$ (corresponding to the 3D point group C_{3v}), while the TT structure obeys only symmetry operations of $p3$ (corresponding to C_3). Dornisch *et al.* found by XRD that the Au-($\sqrt{3}\times\sqrt{3}$)/Si(111) surface belongs to the $p31m$ group and that the Au atoms lie on mirror planes [151].

The impact of the symmetry properties of the point groups C_{3v} and C_3 on the Raman spectra is similar and therefore it is sufficient to consider the first group. Note that the group C_{3v} appeared already in context of the Si(111)-(7×7) reconstruction. The point group C_{3v} has two nondegenerate modes, labeled A_1 and A_2, and a doubly degenerate mode, labeled E. Modes with A_2 symmetry are silent and thus are not optically observable. All other modes are Raman active. The relevant Raman tensors for the experimental spectra are given by [17]:

$$\mathcal{R}^1_{A_1} = \begin{pmatrix} a & 0 \\ 0 & b \end{pmatrix}, \tag{3.3}$$

$$\mathcal{R}^1_{E} = \begin{pmatrix} 0 & c \\ c & 0 \end{pmatrix}, \tag{3.4}$$

$$\mathcal{R}^2_{E} = \begin{pmatrix} -c & 0 \\ 0 & c \end{pmatrix}. \tag{3.5}$$

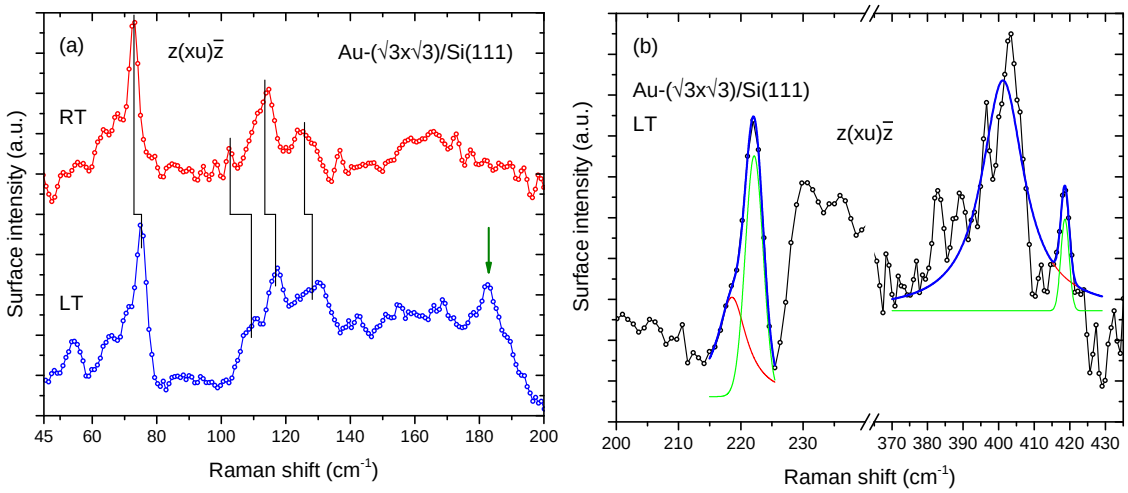

Figure 3.16.: Surface Raman spectra of the Au-($\sqrt{3} \times \sqrt{3}$)/Si(111) surface for $z(xu)\bar{z}$ polarization configuration for (a) RT and LT and (b) at higher frequencies for LT. The modes at higher frequencies are fitted with Voigt profiles.

With the help of these Raman tensors and Eq. (2.21), it is found that A_1 modes are only observable in polarization configuration $z(xx)\bar{z}$. In contrast, E modes appear simultaneously in $z(xx)\bar{z}$ and $z(xy)\bar{z}$ spectra due to the two Raman tensors.

Surface Raman spectra of Au-($\sqrt{3} \times \sqrt{3}$)/Si(111)

The surface Raman spectra of the Au-($\sqrt{3} \times \sqrt{3}$)/Si(111) reconstruction can be divided into the low-frequency part below $\approx$200 cm^{-1} and isolated groups of modes appearing at higher frequencies.

The unpolarized Raman spectra of the lower frequency part are shown in Fig. 3.16(a) for RT and LT. The most prominent and dominant peak is observed at 72.9 cm^{-1} at RT and at 75.2 cm^{-1} at LT. The comparison of these two peaks as well as the whole spectra at both temperatures reveals close correspondence. Therefore, it is sufficient to describe the LT spectrum in the following. The peak at 75.2 cm^{-1} is accompanied by a low-frequency shoulder at 70.8 cm^{-1} and a further separated peak at 65.7 cm^{-1}. The mode located at 54.0 cm^{-1} is clearly resolved in the LT spectrum, while it is much broader in the RT spectrum resulting in an apparent unusual temperature shift. A characteristic structure is the group of three peaks whose individual members are located at 109.3, 116.8, and 128.2 cm^{-1}. Below and above the group there are rather broad features that are hardly distinguishable. Below, one peak is centered at 89.6 cm^{-1}, while the spectra above consists of peaks at 142.3, 154.8, and 168.7 cm^{-1}. A clear difference between the LT and RT spectra is a peak at 182.9 cm^{-1} in LT that is marked by a green arrow in Fig. 3.16(a). A

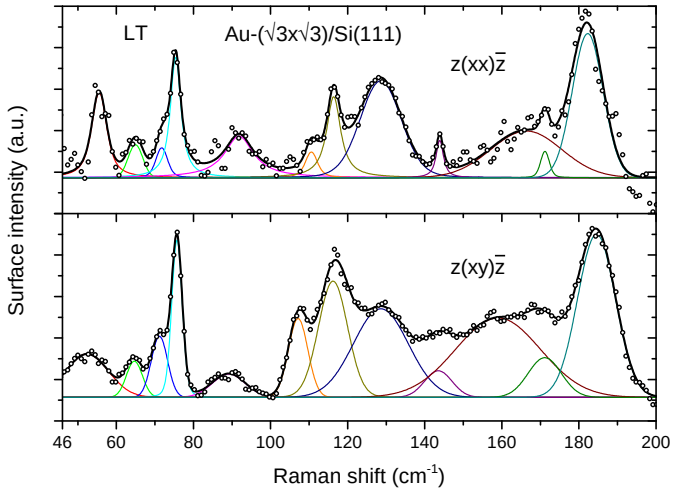

Figure 3.17.: Surface Raman spectra of the Au-($\sqrt{3} \times \sqrt{3}$)/Si(111) reconstruction fitted with Voigt profiles. Both polarization configurations $z(xx)\bar{z}$ and $z(xy)\bar{z}$ are shown for LT.

counterpart for this LT peak is not found in the corresponding RT spectrum. Apart from the last mode, the similarities of the Raman spectra give no reason to see indications for a phase transition upon cooling from RT to LT.

Apart from the eigenmodes described above, there are two double groups of modes at higher frequencies. In the unpolarized LT spectrum in Fig. 3.16(b), the first prominent peak is observed at 222.1 cm^{-1} with a low-frequency shoulder at 218.6 cm^{-1}. The existence of these peaks is evident in the surface Raman spectra as it is further supported by RT Raman data. However, in the spectra with the bulk contribution of the Si(111) substrate the peaks are hard to discriminate, since they lie in the steep edge towards the 2TA(W). The second group of peaks consists of a broad peak at 401.2 cm^{-1} and a narrow one at 418.6 cm^{-1}. This assembly is also found in the RT Raman spectra.

Additional information about the peaks below ≈200 cm^{-1} is gained by the inspection of the polarized LT spectra in Fig. 3.17. All Raman peaks observed in the polarized spectra find equivalents in the separately recorded LT spectrum in Fig. 3.16(a). By comparison of the intensities of the $z(xx)\bar{z}$ and $z(xy)\bar{z}$ Raman spectra, the prominent peak at 75.2 cm^{-1} can be labeled as E mode since it is observed in both polarization configurations. All other modes in the spectra are E modes, except the mode at 128.2 cm^{-1}. This latter mode is more pronounced in the $z(xx)\bar{z}$ spectrum (in relation to the adjacent peaks of the triple group) than it is in the $z(xy)\bar{z}$ spectrum. Therefore, it is identified as mode with A_1 symmetry. The situation changes for the eigenmodes with higher frequencies. The majority has A_1 character, while only the mode at 222.1 cm^{-1} is E-like.

A further mode was observed at 25 cm^{-1} in a RT Raman spectrum recorded with

Table 3.4.: Vibrational peak frequencies (in cm^{-1}) of the Au-($\sqrt{3} \times \sqrt{3}$)/Si(111) reconstruction. The unpolarized SRS results are presented for RT and LT together with the symmetry properties of the modes. The additional SRS data (Col. 4) at RT are taken from Ref. [33] of the author's publications. The theoretical results according to DFT-GGA calculations are tabulated for the CHCT and TT model [33]. For the calculated modes the frequency (F), the normalized Raman scattering efficiency (I), the mode symmetry (S), and the localization (L) are listed. The latter is differentiated in modes localized at the Au adatom layer (Au), the Si layer (Si), and in between (Mix.). Modes with vanishing intensity or no surface localization are not shown.

SRS				Theory							
				CHCT				TT			
RT	LT	Sym.	RT	F	I	S	L	F	I	S	L
				17	0.759	E	Au	16	0.093	E	Au
			25	33	0.001	A	Au	33	0.387	A	Au
55.2	54.0	E	46	45	0.253	A	Au	49	0.196	E	Mix.
62.7	65.7	E	62	55	0.013	E	Mix.	51	1.000	A	Au
67.9	70.8	E	69					55	0.267	E	Au
72.9	75.2	E	73	64	1.000	E	Mix.	76	0.031	E	Au
86.5	89.6	E	85	89	0.354	E	Si	85	0.307	A	Au
102.7	109.3	E	104	97	0.038	A	Mix.	109	0.224	A	Au
113.5	116.8	E	114	102	0.215	E	Au				
125.8	128.2	A_1	125	127	0.063	A	Au	151	0.065	E	Si
136.7	142.3	E	141	153	0.013	A	Mix.	157	0.002	A	Mix.
	154.8	E	170	160	0.127	A	Si	159	0.016	A	Si
165.1	168.7	E		165	0.114	E	Mix.	162	0.012	A	Mix.
	182.9	E		198	0.620	A	Mix.	198	0.073	A	Mix.
								200	0.133	E	Mix.
								205	0.037	E	Si
								209	0.040	E	Mix.
								209	0.095	A	Mix.
217.1	218.6	A_1	217	205		E	Si				
220.8	222.1	E	221	221		E	Mix.	242		A	
397.2	401.2	A_1	397	400		A	Si				
414.4	418.6	A_1	414	417		A	Si	413		A	

Table 3.5.: Formation energy (in eV/SUC) of the TT model of the Au-($\sqrt{3} \times \sqrt{3}$)/Si(111) surface with respect to the CHCT model, which acts as a reference. The values are calculated with LDA and GGA, in each case for two different lattice constants. Equilibrium lattice constants are labeled by (eq) and experimental lattice constants are denoted as (exp). Data adapted from Ref. [33].

Structural model	$\text{LDA}^{(\text{eq})}$	$\text{GGA}^{(\text{eq})}$	$\text{LDA}^{(\text{exp})}$	$\text{GGA}^{(\text{exp})}$
TT	unstable	0.085	unstable	0.022
CHCT	$\equiv 0$	$\equiv 0$	$\equiv 0$	$\equiv 0$

a different Raman setup as described in Ref. [33] of the author's publications. A determination of the polarization configuration of this mode was not possible. All modes described so far are tabulated together with their polarization properties in Tab. 3.4.

In Ref. [88] of the author's publications, additional SRS data of the Au-($\sqrt{3} \times \sqrt{3}$)/Si(111) surface that were recorded with a separate setup are shown for RT. There, the presented spectrum below about 200 cm^{-1} is quite similar to the one in Fig. 3.16(a). However, the modes at higher frequencies (397 and 414 cm^{-1}) in Fig. 3.16(b) were not observed in Ref. [88]. As pointed out there, this is due to the surface orientation of the used substrates. This point is picked up again in Sec. 3.3.5.

Comparison with first-principles calculations for Au-($\sqrt{3} \times \sqrt{3}$)/Si(111)

On the basis of a comparison of the SRS data and theoretical calculations, a favored structural model can be chosen. For this reason, the Raman spectra for both models (TT and CHCT model) were obtained by *ab initio* DFT calculations [33]. To estimate possible deviations of the DFT calculations, they were performed for the XC functionals LDA and GGA (in the PBE formulation) as well as for equilibrium and experimental lattice constants. A $(12 \times 12 \times 1)$ k-point mesh and a plane-wave cutoff energy of 500 eV were used. As can be seen in Tab. 3.5, the CHCT structure is the most stable one for both XC functionals. In contrast, the TT model has an elevated formation energy per SUC (85 and 22 meV for equilibrium and experimental lattice constant, respectively), but is stable in the GGA. Within the LDA, the TT model is not stable. Moreover, differences between the functionals can be evaluated for each model. Between the DFT-LDA and DFT-GGA, the vibrational mode frequencies deviate by several cm^{-1} in most cases. The maximum of 9 cm^{-1} can be considered as the error of these calculations. In the following only calculations for the experimental lattice constant are used.

The calculated vibrational mode frequencies for both structural models within the DFT-GGA are included in Tab. 3.4. Together with the frequencies, the normalized

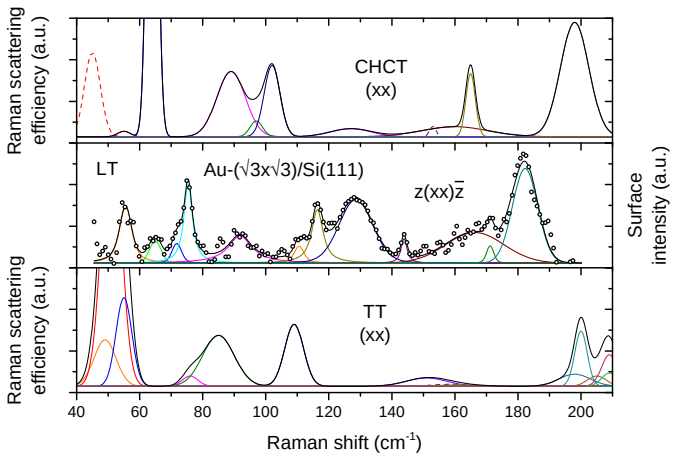

Figure 3.18.: Comparison of the calculated Raman scattering efficiency and the $z(xx)\bar{z}$ surface Raman spectrum of Au-($\sqrt{3} \times \sqrt{3}$)/Si(111) at LT. The results for the structural models CHCT and TT are depicted for the polarization configuration (xx). Dashed lines show peaks that are observed in the experimental Raman spectra, but have vanishing intensities in the calculations. Calculation results adapted from Ref. [33].

Raman scattering efficiency and the polarization properties are given for every mode. Like from the experimental point of view, the polarization properties of the modes are separated into A and E modes. Here, A modes preserve the rotational symmetry, while E modes reduce the surface symmetry. The degeneracies of the modes are equivalent to the group theoretical cases. Another key information of the modes are their localizations which help to identify their origin. Modes whose eigenvectors are localized by at least 75 % within the topmost three layers are considered as surface phonons. In a second step the modes can be attributed mainly to movements of the Au or Si atoms or to mixtures of both. After assignment of calculated to measured peaks, the peaks in the calculated spectra are broadened with Voigt profiles of the experimentally obtained FWHMs. The result can be directly compared to the measured Raman spectra.

The calculated spectra for both models are shown in Fig. 3.18. For comparison, the experimental $z(xx)\bar{z}$ spectrum at LT is added. The experimental and calculated spectra can be compared in the spectral range $45-200\,\mathrm{cm}^{-1}$. For the CHCT model, the distinct experimental Raman peaks at 75.2 and $182.9\,\mathrm{cm}^{-1}$ are identified with the most intense calculated modes at 64 and $198\,\mathrm{cm}^{-1}$, respectively. The first mode is theoretically predicted to buckle the Au adlayer by elongation in [111] direction, while the latter one is mainly due to a vertical breathing mode of the Si trimers with only minor movement of the Au atoms. No correspondence to the shoulder of the peak at $75.2\,\mathrm{cm}^{-1}$ is found in the calculations. Therefore, a possible scenario

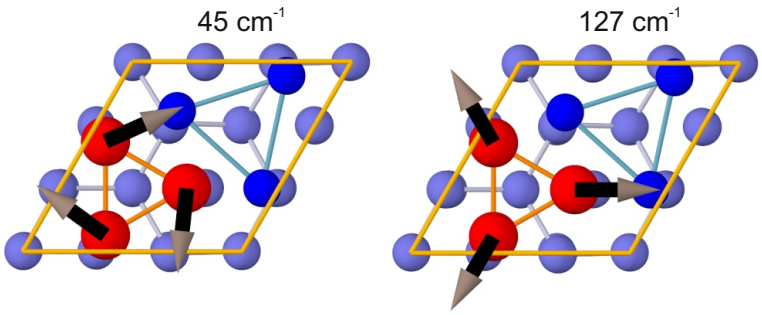

Figure 3.19.: Displacement patterns of two modes of the Au-($\sqrt{3} \times \sqrt{3}$)/Si(111) surface system for the CHCT model. The modes are of A type and have the frequencies 45 and 127 cm^{-1}. Arrows indicate rigid translations. Adapted from Ref. [33].

might be the splitting of the main E mode at 75.2 cm^{-1} in the experimental spectra due to structural aspects like additional adsorbates or domains boundaries. This is supported by the fact that the shoulder has also E symmetry. At lower frequencies, the first two calculated modes at 33 and 45 cm^{-1} are identified with peaks close to that frequency in the RT spectrum in Ref. [33]. However, for the peaks at 45 and 55 cm^{-1} there are measured features that fit better if instead of intensities only frequencies are considered. For all other calculated modes equivalents are found in the measured spectra. These are the calculated phonon modes at 89, 97, 102, 127, 153, 160, and 165 cm^{-1}. Also the polarization configurations are conform in many cases. At higher frequencies, there are modes found that are mainly located at the Si layers. All peaks find their counterparts and the discrepancies between the frequencies are quite small. Instead, the calculated spectra of the TT model do not match with the SRS data as good as the ones of the previous model. In the spectral ranges 109 – 151 cm^{-1} as well as 209 – 242 cm^{-1}, no Raman scattering efficiency was predicted, although it is observed experimentally. In turn, many vibrational modes appear in the calculations in the spectral range 200 – 209 cm^{-1}, but there is no intensity observed in the SRS data. As a conclusion of this discussion, it is stated that the CHCT structural model matches much better to the SRS measurements than the TT model.

Discrepancies between the calculations and the measured Raman spectra might have the same reasons as discussed in the case of Au-(5×2)/Si(111). For the Au-($\sqrt{3} \times \sqrt{3}$)/Si(111) surface, STM measurements revealed domains walls [123], which are also likely to be present here. The vibrational modes are prone to be altered by these domain walls.

Another output of the calculations within the frozen-phonon method are the eigenvectors of the modes. For two exemplary modes, the planar displacement vectors are shown in Fig. 3.19 for the CHCT model. Both modes have A symmetry.

They are predominantly localized at the Au atoms, while the Si adatoms are not affected by the Au atom motion. For the mode with 45 cm^{-1}, a rigid torsion of the Au trimers with respect to the substrate is predicted by the calculations. Instead, the mode with a frequency of 128 cm^{-1} is a symmetric expansion of the Au trimer and is accordingly labeled breathing mode. The vibrational pattern of the Au adatoms of this mode can be also determined by applying Eq. (2.15).

3.3.5. Relationship of Au/Si(111) and Au/Si(hhk)

Apart from the coverage of Au on the substrate surface, another parameter that can be varied is the orientation of the substrate. Thus, Si(111) can be substituted with vicinal Si(hhk) substrates, i.e., like Si(553), Si(557), and Si(775). The surface planes of the substrates with higher Miller indices are tilted with respect to the (111) plane. In particular, the mentioned vicinal Si substrates are titled by approximately $8-13°$ in $[11\bar{2}]$ or $[\bar{1}\bar{1}2]$ direction [152]. This results in a surface with terraces with (111) orientation, separated by steps. To evaluate the influence of the surface orientation on the (5×2) and $(\sqrt{3}\times\sqrt{3})$ reconstruction and their surface vibrations, SRS results for MLs of Au on different substrate types were reported in Ref. [88]. The preparation conditions are similar to the ones of the Au/Si(111) surfaces. A first result is that the surface reconstructions still appear as observed for the Si(111) substrate. This is not too surprising because the substrates are just terraced while keeping their short-scale (111) orientation. A useful advantage of the Au-(5×2)/Si(hhk) surface is that there is macroscopic single-domain selection in contrast to Au-(5×2)/Si(111).

The observed surface vibration modes for Au/Si(hhk) can be grouped into three classes. The first class contains modes that involve the displacement of the Au adatoms. Therefore, they are located at lower frequencies (below ≈130 cm^{-1}). A second class is related to vibrations of Si-Si configurations that are in the spectral range centered around ≈150 cm^{-1} and up to ≈350 cm^{-1}. Since these modes mimic the 2TA phonon structure, they are thought to be acoustical phonons of the Si substrate that are activated by the impact of the adlayers and the orientation of the substrate. The third and last class includes modes at around 400 cm^{-1} that are purely attributed to the vicinality of the substrate. These modes are located at approximately 392 and 414 cm^{-1}. They only appear for stepped substrates and vary only by a few cm^{-1} for substrates with different (hhk) surface orientations.

However, for the Au-$(\sqrt{3}\times\sqrt{3})$/Si(111) surface (see Sec. 3.3.4) modes with very similar frequencies like the ones of the third class are observed, i.e., at 397.2 and 414.4 cm^{-1} (at RT). This is puzzling at first glance, since the Si(111) substrates are not intentionally miscut with respect to the (111) surface plane. A plausible reason for that might be very slight deviations in the preparation conditions of the clean Si substrates. Additional to miscut, it is known that steps on Si(111) substrate can be also influenced by the annealing temperature and time, the heating current

direction, and possible stress [153]. This even holds for substrates with miscuts in the range of 1° which also show steps and were used for the preparation of the Au-($\sqrt{3} \times \sqrt{3}$)/Si(111) reconstruction. Hence, the occurrence of vicinality-induced modes for Au-($\sqrt{3} \times \sqrt{3}$)/Si(111) can be readily explained.

3.4. Sn-induced surface reconstructions on Ge(111) and Si(111)

In a similar manner like Au on Si(111), small amounts of Sn deposited onto Ge(111) and Si(111) substrates can reconstruct in dependence of the thermal treatment and coverage in many different ways [154,155]. The phase diagrams for the systems Sn/Ge(111) and Sn/Si(111) are shown in Fig. 3.20. The meaning of the temperatures and coverages in the diagrams is the same as for Au/Si(111) in Fig. 3.8. For Sn coverages below 0.1 ML, the reconstructions of the clean surfaces, i.e., c(2×8) for Ge(111) and (7×7) for Si(111), are still observable. Of special interest are the $(\sqrt{3} \times \sqrt{3})R30°$ surface reconstructions, formed for a Sn coverage of $\theta_{\mathrm{Sn}} \simeq \frac{1}{3}$ ML on both substrates (see Secs. 3.4.3, 3.4.4, and 3.4.5). Although the $(\sqrt{3} \times \sqrt{3})$ reconstruction of Sn/Ge(111) was considered to be metastable in Ref. [154], it is included in Fig. 3.20(a) according to results of this thesis. The region for Sn/Si(111), where the $(\sqrt{3} \times \sqrt{3})$ reconstruction can be observed, is quite large. Yet, only surface reconstructions with a coverage of $\frac{1}{3}$ ML (marked by an arrow in Fig. 3.20(b)) are examined here. The Sn/Ge(111) system forms for higher coverages (5×5) and (7×7) reconstructions as well as mixed phases. For higher Sn coverages on Si(111) ($\theta_{\mathrm{Sn}} \simeq$ 0.3 – 1.1 ML) and annealing temperatures below 450 K, the Sn-($2\sqrt{3} \times 2\sqrt{3}$)/Si(111) reconstruction is obtained (see Sec. 3.4.6). By further annealing, the $(\sqrt{3} \times \sqrt{3})$ reconstruction can be subsequently prepared based on the $(2\sqrt{3} \times 2\sqrt{3})$ surface. Both substrates show for very high annealing temperatures the (1×1) reconstruction, like also observed for Au/Si(111). In the case of Sn/Ge(111), there is a region in the phase diagram around 0.2 ML where the (1×1) periodicity is observed irrespective of the annealing temperature.

The main part of this section will be dedicated to the reconstruction of $\frac{1}{3}$ ML Sn on Ge(111) and Si(111) as well as its comparison. The atomic structure and the closely connected relevant model for the description of the observed physical phenomena will be explained before. The second part deals with the Sn-($2\sqrt{3} \times 2\sqrt{3}$)/Si(111) reconstruction and thin films of α-Sn.

Although both surface systems Sn/Ge(111) and Sn/Si(111) are isovalent and have many similarities, their temperature behavior differs considerably. For the Sn/Ge(111) surface, a reversible structural phase transition (SPT) was observed experimentally upon cooling. The $(\sqrt{3} \times \sqrt{3})R30°$ reconstruction transforms to the (3×3) reconstruction at $T_{\mathrm{SPT}} \approx 210 - 220$ K [156,157]. In contrast, the Sn/Si(111)

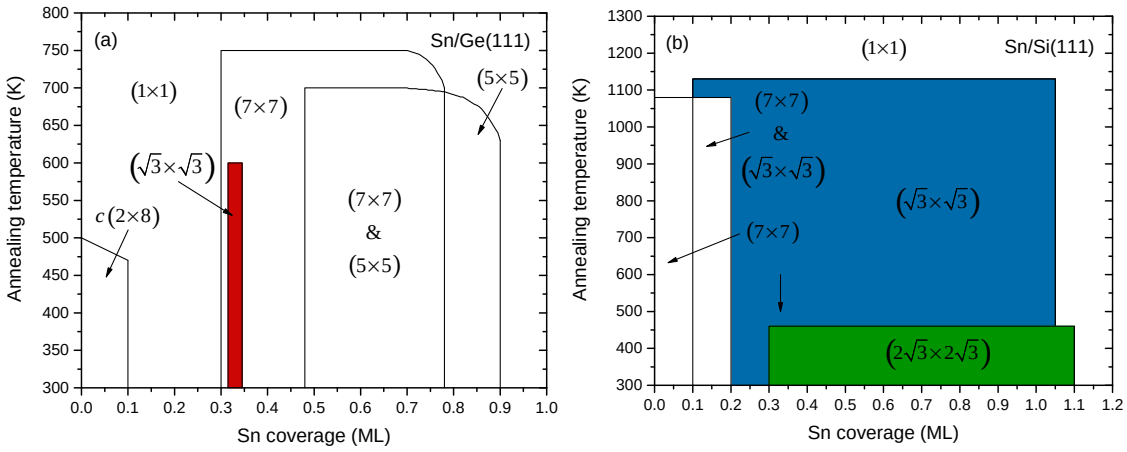

Figure 3.20.: Phase diagrams of the surface adsorbate systems (a) Sn/Ge(111) and (b) Sn/Si(111). With varying Sn coverages and annealing temperatures different phases are obtained. Adsorbate reconstructions considered here are marked by different colors. Data adapted from Refs. [154,155].

surface exhibits the $(\sqrt{3} \times \sqrt{3})R30°$ reconstruction even when the sample is cooled. Thus, a SPT does not occur [158].

For the explanation of the SPT of Sn/Ge(111), several models were proposed, which include, e.g., the charge density wave model [156,159,160], defect-related models [161,162], and the dynamical fluctuation (DF) model [163–166].

Apart from this discrepancy, further interesting effects were found for these surface systems. For Sn/Si(111), a Mott transition was observed for $T < 60\,\mathrm{K}$ in scanning tunneling spectroscopy (STS) measurements [167]. When the sample is cooled, the conductance declines for sample bias voltages equal to E_F and an energy gap of 40 meV opens. This behavior is remarkable, since the surface should be metallic because it has an odd number of electrons per SUC and the transition is not accompanied by a structural rearrangement. Also for Sn/Ge(111), a Mott insulating ground state was observed for $T < 30\,\mathrm{K}$ by Cortés *et al.* [168]. Moreover, it is accompanied by a restoration of the $(\sqrt{3} \times \sqrt{3})R30°$ reconstruction. Both Mott transitions were also predicted in *ab initio* calculations for Sn/Ge(111) and Si/Si(111) [169]. Yet, there were subsequent studies for Sn/Ge(111) that disagreed with this experimental result [170–172]. More recently, Cortés *et al.* restated the idea of an insulating $(\sqrt{3} \times \sqrt{3})$ phase together with the existence of an additional phase, labeled as charge ordered insulator (COI) phase [173]. This additional intermediate phase has (3×3) periodicity and was reported to appear at $T \lesssim 60\,\mathrm{K}$ in coexistence with the metallic (3×3) phase and at lower temperatures together with the $(\sqrt{3} \times \sqrt{3})$ Mott phase. It will be part of a later discussion. Note that the measurements presented in this thesis are conducted above this second claimed

transition temperature of ≈30 K for Sn/Ge(111), but the onset of the COI phase is in the accessible temperature interval.

With respect to surface magnetism, the three spins located at the adsorbed Sn atoms in a triangular lattice generally cannot arrange antiparallel simultaneously, which results in spin-liquid behavior. Despite this spin frustration, for the $(\sqrt{3}\times\sqrt{3})$ reconstruction of Sn/Si(111) it was shown in a combined study of theoretical calculations and ARPES measurements that the spins are ordered in a row-wise collinear antiferromagnetic alignment [174]. Through this ordering, an effective surface periodicity of $(2\sqrt{3}\times 2\sqrt{3})$ is observed. This is also confirmed by a recent study, which also finds $(2\sqrt{3}\times\sqrt{3})$ domains that constitute to the $(2\sqrt{3}\times 2\sqrt{3})$ symmetry [175]. Moreover, because of the observed small Rashba splitting, i.e., the splitting of spin-polarized parabolic electronic dispersions due to the surface symmetry, the SOC is believed to be weak for Sn/Si(111). On the basis of this study, the Mott transition is more likely ascribed to be driven by electronic correlations than by ordering of electron spins [175].

Aside of Sn adatoms, with Pb there is another group-IV element that forms regular reconstructions on Ge(111) and Si(111). For a coverage of $\frac{1}{3}$ ML, Pb atoms reconstruct on Ge(111) and Si(111) in a $(\sqrt{3}\times\sqrt{3})$ periodicity at RT, but undergo a reversible SPT to a (3×3) reconstruction upon cooling [176,177]. These systems are similar to Sn/Ge(111) in many aspects. But there is another reconstruction with $(\sqrt{3}\times\sqrt{3})$ periodicity for a higher Pb coverage of $\frac{4}{3}$ ML. This reconstruction of Pb/Si(111) was investigated by E. Speiser *et al.* in a recent SRS study in combination with *ab initio* calculations [178]. For the $(\sqrt{3}\times\sqrt{3})$ reconstruction two different atomic structures that differ only slightly were proposed [179]. Three Pb atoms on T_1 positions saturate Si DBs from the substrate, while an additional Pb atom is located at the H_3 or T_4 position. These two structure models are only separated by a formation energy of 0.01 eV per (1×1) SUC [179]. Moreover, the calculated vibrational eigenfrequencies for both models are very close inhibiting an assignment of the SRS data. Despite that, the SRS-derived vibration-mode frequencies agree very well with calculations. Since Pb atoms are heavy, modes that involve Pb vibrations all occur in the range below 95 cm^{-1}. In general, these modes can be divided into classes with different vibrational patterns and different localizations.

SPTs in surface adsorbate systems, as mentioned above, are observable by SRS as was demonstrated for instance for In nanowires on Si(111) substrate [180]. This system exhibits a transition from a (4×1) reconstruction at RT to an (8×2) reconstruction upon cooling [181], which was attributed to CDW formation as well as to other mechanisms [182]. In the temperature-dependent surface Raman data, the spectra for the different phases can be clearly distinguished by their different Raman peak signatures. The expected SPT for Sn/Ge(111) which is considered in the context of the DF model will be the subject of the next section.

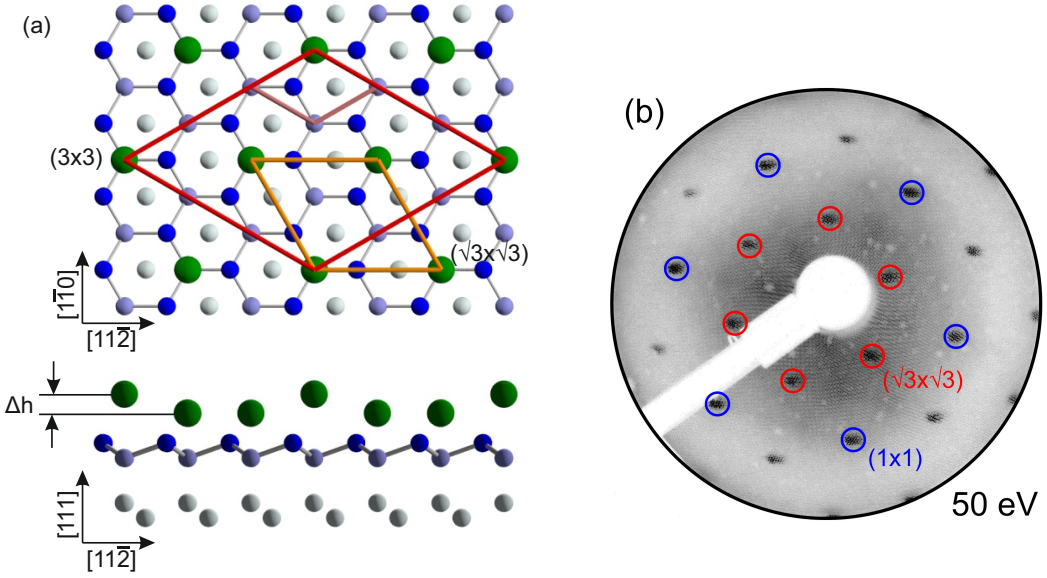

Figure 3.21.: Depiction of (a) the atomic surface structure (top and side view) and (b) the LEED pattern of Sn/Ge(111). The Sn atoms are colored in green. The orange, red, and brown rhombs mark the $(\sqrt{3} \times \sqrt{3})$, (3×3), and (1×1) SUC, respectively. The LEED pattern was recorded at RT and with an electron energy of 50 eV.

3.4.1. Dynamical fluctuation model and phase transitions

Before the DF model and its implications are discussed in detail, the underlying atomic surface structures of Sn/Ge(111) and Sn/Si(111) are explained.

Atomic surface structure and LEED pattern of Sn/Ge(111) and Sn/Si(111)
The atomic structures for both Si(111) and Ge(111) with $\frac{1}{3}$ ML Sn coverage are very similar at RT [164]. A top view of the structure is shown in Fig. 3.21(a) for Sn/Ge(111), but also applies for Sn/Si(111). Indeed, the atomic distances are different as implied by the different substrates. On both substrates, the Sn atoms occupy T_4 positions [183,184].

This similarity between Sn/Ge(111) and Sn/Si(111) is also reflected in the LEED pattern which exhibits analogous features. The LEED pattern shown in Fig. 3.21(b) is that of Sn/Ge(111) at RT. The features of the LEED pattern are similar to those of Au-$(\sqrt{3} \times \sqrt{3})$/Si(111) in Fig. 3.15.

However, the temperature behavior of both systems differs substantially when the temperature is lowered from RT. An essential key for the understanding will be the vertical height of the Sn atoms above the substrate. The Sn atoms are not on equal heights and are thus not equivalent. This is indicated in the side view as

depicted in the lower part of Fig. 3.21(a). Two possible SUCs are marked in the top view of Fig. 3.21(a). The orange rhomb marks the $(\sqrt{3} \times \sqrt{3})R30°$ SUC which encloses one Sn atom per SUC for the hypothetical configuration of Sn atoms on equal heights. In contrast, the (3×3) SUC, marked by the red rhomb, contains three Sn atoms per SUC. The description of the height development is discussed in the framework of the DF model.

Dynamical fluctuation model

If all Sn atoms are on the same height above the substrate, a $(\sqrt{3} \times \sqrt{3})$ is formed. But as observed in experiments (see, e.g., Ref. [185]), every third atom in $[11\bar{2}]$ direction protrudes the other two. This leads to the enlarged (3×3) SUC. The Sn atoms are labeled as "up" (U) and "down" (D) atoms according to their vertical height. The height difference was experimentally determined to be $\Delta h = 0.3$–0.45 Å [185,186]. The resulting configuration is abbreviated by 1U2D. In principle, a 2U1D configuration would also result in a (3×3) SUC, but was rejected by DFT calculations [187].

At elevated temperatures like RT, the Sn atom in an up position exchanges its vertical location randomly with one of the other Sn atoms in down positions. From measurements of the time dependent tunneling current in STM, a time scale of 1 ms is reported for the exchanges at 220 K [166]. This general assumption for the behavior is supported by MD simulations, but a much shorter time scale of 1 ps at 350 K was obtained [188]. Due to these random swaps, neighboring SUCs are not in phase and therefore the formation of a long-range order is inhibited. The considerations so far apply for both Sn/Ge(111) and Sn/Si(111) at RT [164,189].

This situation changes when the temperature of the sample is lowered. For Sn/Ge(111), the frequency of interchanges between the positions decreases with decreasing temperature [166]. The SUCs freeze into a static 1U2D configuration. Initially, small patches grow into larger areas with a long-range 1U2D pattern. This results in a coherent (3×3) reconstruction at LT. Hence, a reversible SPT occurs: $(\sqrt{3} \times \sqrt{3}) \leftrightarrow (3\times3)$. These considerations constitute the DF model. In contrast, the Sn/Si(111) surface keeps its high-temperature behavior also at LT. The different properties of both systems were predicted by Pérez *et al.* to be related to vibrational characteristics, i.e., the existence of a soft phonon [164]. A soft phonon is a vibrational mode whose frequency declines (possibly to zero) with decreasing temperature at a certain $\vec{k}$ point in the BZ. Thus, it induces a certain static periodicity. Sn/Ge(111) is assumed to exhibit a surface soft phonon, while Sn/Si(111) has none. The underlying reason is found in the different hybridizations between Sn adatoms and the substrate atoms which results in a greater electronic energy gain by the phonon softening for the Ge substrate over the Si counterpart. Further details of the surface phonons will be given below for each surface system.

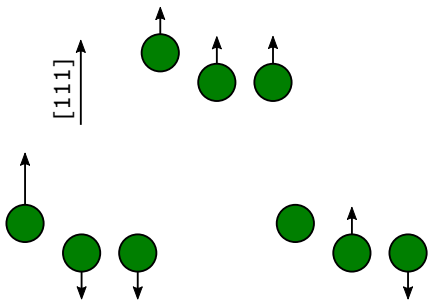

Figure 3.22.: Schematic depiction of the vibrational patterns of the Sn atoms for Sn/Ge(111) and Sn/Si(111). These eigenmodes are labeled as DF modes. The mode in the upper row, where all displacement vectors point vertically in phase, is of special interest here. Adapted from Ref. [190].

Vibrational eigenmodes and symmetry considerations

Besides the dominant up-down configuration, the three Sn atoms vibrate in several eigenmodes around their equilibrium positions. By restricting the movement to vertical displacement, one assumes three different eigenmodes. In Fig. 3.22, three possible displacement patterns are depicted [190]. These modes constitute an orthogonal basis and were chosen to be presumably close to the exact phonon modes of the system. Since these modes are closely entangled with the DF model, they are accordingly referred to as DF modes. Note that the vibrational patterns can also be applied to situations where one of the other Sn atoms is in an up position. Apart from these prototypical modes, however, further vibrational modes including also the substrate atoms and mixtures are expected.

The (3×3) reconstruction belongs to the 2D space group $p3m1$ which corresponds to the 3D point group C_{3v}. The $(\sqrt{3} \times \sqrt{3})$ reconstruction, which would result for equivalent Sn atoms, transforms according to the 2D space group $p31m$ which also corresponds to the 3D point group C_{3v} [191]. Hence, irrespective of the actual reconstruction the symmetry aspects and Raman selection rules are identical for Sn/Ge(111) and Sn/Si(111). The applying selection rules were already discussed in connection with the Au-$(\sqrt{3} \times \sqrt{3})$/Si(111) surface in Sec. 3.3.4, where it is stated that there are two possible Raman-active modes with A_1 and E symmetry for the C_{3v} group.

As argued within the DF model so far, even at RT the 1U2D configuration with (3×3) character still exists locally. On the other hand, the LEED pattern shows a $(\sqrt{3} \times \sqrt{3})$ reconstruction. This apparent contradiction can be solved by regarding the used experimental technique.

Importance of used experimental technique

The observed reconstruction ($(\sqrt{3}\times\sqrt{3})$ vs. (3×3)) of Sn/Ge(111) and Sn/Si(111) at RT depends crucially on the used experimental technique. Methods like conventional LEED and STM for instance, average their measurement data over the time duration of observation. Therefore, the Sn atoms appear to be on equal heights after averaging, resulting in an apparent $(\sqrt{3}\times\sqrt{3})$ reconstruction. But there are other experimental methods that take essentially snapshots of the sample and are therefore intrinsically non-averaging. As an example may serve RS since the Raman process takes place instantaneously (except for extremely resonant cases) [14]. In view of the Sn/Ge(111) surface and its temperature evolution of the atomic configuration, one would expect similar observations, i.e., similar surface Raman spectra, for RT and LT.

3.4.2. Preparation of Sn reconstructions on Ge(111) and Si(111)

Onto the clean Ge(111)-c(2×8) and Si(111)-(7×7) surfaces, $\frac{1}{3}$ ML of Sn is evaporated. The absolute Sn amount varies slightly because of the different sizes of the UCs of Ge(111) and Si(111).

In the case of Ge(111), the surface is annealed after deposition of the Sn atoms at $T = 560\,\mathrm{K}$ for $t = 3\,\mathrm{min}$. Similarly, the Si(111) surface is also annealed after deposition at $T = 970\,\mathrm{K}$ for $t = 3\,\mathrm{min}$. After annealing the samples are slowly cooled to RT (see also Sec. F).

The LEED pattern is checked afterwards for both surface systems to ensure the quality of the surface reconstruction.

If the amount of Sn deposited on Si(111) is further increased to ≈1.0 ML, the Sn-$(2\sqrt{3}\times2\sqrt{3})$/Si(111) surface is formed. Technically, the $(2\sqrt{3}\times2\sqrt{3})$ reconstruction is obtained by deposition of additional Sn onto the already prepared reconstruction with $\frac{1}{3}$ ML. The annealing temperature is reduced to $T = 770\,\mathrm{K}$ for $t = 2\,\mathrm{min}$ to achieve this reconstruction. This temperature is higher than the annealing temperature suggested by the phase diagram in Fig. 3.20(b). The LEED pattern changes correspondingly and is clearly distinguishable.

3.4.3. Raman spectroscopy results for Sn/Ge(111)

The Raman spectra of Sn/Ge(111) are presented in this section for frequencies above ≈80 cm^{-1}. The spectra for lower frequencies are discussed separately in Sec. 3.4.5.

The surface Raman spectra for the polarization configurations $z(xx)\bar{z}$ and $z(xy)\bar{z}$ are shown in Fig. 3.23(a). As can be seen there, the spectra for RT and LT look similar on first glance. The LT spectra show temperature-induced narrowing of the line width and therefore finer features are resolved. For a further evaluation,

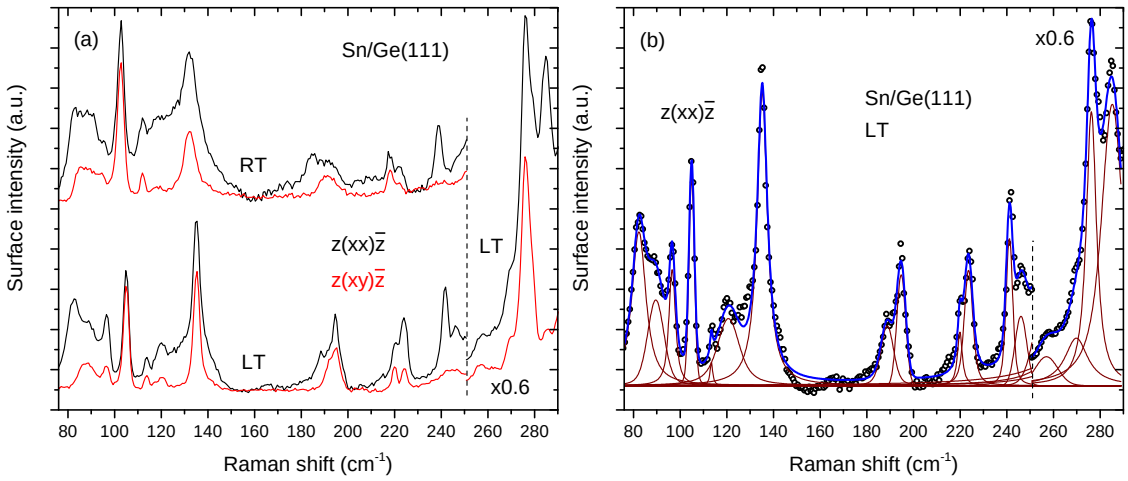

Figure 3.23.: Surface Raman spectra of Sn/Ge(111) (a) at RT and LT for both polarization configurations and (b) at LT for $z(xx)\bar{z}$ configuration with Voigt fits. In the spectral region from 250 cm^{-1} toward the LTO phonon the Raman intensity is scaled down to enable the observation of all peaks.

the spectra are fitted by Voigt profiles, as shown exemplarily in Fig. 3.23(b). A narrow and distinct Raman peak is observed in the LT spectra for 104.9 cm^{-1} (102.6 cm^{-1} at RT). It clearly appears in both polarization configurations and is therefore assigned as E-like mode. This peak is framed by groups of three peaks on the low-frequency side (82.3, 89.6, and 96.6 cm^{-1}) as well as on the high-frequency side (113.4, 120.7, and 135.2 cm^{-1}). Note that except for the first peak, which is only observed in $z(xx)\bar{z}$ configuration, all modes are present in both configurations. In the spectral range above the bulk 2TA(X) feature of the Ge(111) substrate (at ≈163 cm^{-1}, see Sec. 3.1), there are three groups of two peaks each. In the first group at 188.8 and 194.7 cm^{-1} the peaks have different polarization behavior. The next group at 219.9 and 223.6 cm^{-1} is clearly resolved as a double peak, especially in the $z(xy)\bar{z}$ spectrum. The last group, only clearly resolved in the LT spectra, is mainly observed in the $z(xx)\bar{z}$ spectrum at 241.1 and 246.1 cm^{-1}. An associated peak with the latter mode was not clearly resolved in the RT spectra. In the low-frequency edge of the LTO phonon of the substrate, starting at ≈250 cm^{-1}, several peaks at 257.0, 269.8, 276.3, and 285.2 cm^{-1} are observed. The two latter are very distinct and exhibit E and A_1 polarization, respectively. Their origin might be similar to the one related to backfolding discussed for Ge(111)-c(2×8) in Sec. 3.2.3. However, for the peak at 269.8 cm^{-1} in the LT spectrum no equivalent at RT was observed. The peaks described so far are tabulated in Tab. 3.6.

Apart from the usual frequency shifts with temperature, no vast changes between

the RT and LT spectra are observed. Therefore, no indications for a SPT occur in the Raman spectra of Sn/Ge(111) above ≈80 cm^{-1}.

3.4.4. Raman spectroscopy results for Sn/Si(111)

Like for Sn/Ge(111), the Raman spectra of Sn/Si(111) are shown in this section only for frequencies above ≈130 cm^{-1}. The spectra for lower frequencies are considered separately in Sec. 3.4.5.

The surface Raman spectra of Sn/Si(111) are shown for both temperatures and polarization configurations in Fig. 3.24(a). The first distinct peak is found in the LT spectra at 185.5 cm^{-1} (183.5 cm^{-1} at RT). This peak appears in the $z(xx)\bar{z}$ and $z(xy)\bar{z}$ spectra as expected for E-like modes. Below, a broad shoulder-like feature adjoins. It is centered at 169.9 cm^{-1} and vanishes almost completely in the $z(xy)\bar{z}$ spectra. The peak at 230.5 cm^{-1} is located at the edge of the bulk 2TA(L) of the Si(111) substrate (see Sec. 3.1), but is clearly apparent in the difference spectra. Above the step at ≈300 cm^{-1} induced by the bulk 2TA(X) of Si(111), the next peak at 331.8 cm^{-1} is only observed in the $z(xx)\bar{z}$ spectra. These polarization properties (i.e., A_1 symmetry) account also for the following two peaks at 385.5 and 416.4 cm^{-1}, of which the first one is by far the most intense. The origin of these peaks will be discussed later in combination with Au/Si(111). The peak at 450.5 cm^{-1} is located at the same frequency as the bulk 2TA(W) of Si(111), but is revealed in the difference spectra. Similar peaks, like the last one at 487.5 cm^{-1}, are observed at the low-frequency edge of the LTO phonon for Ge(111)-c(2×8) and Sn/Ge(111) and likely share the same origin. All peaks are appended to Tab. 3.6.

Like for the previous surface system Sn/Ge(111), no indications for a SPT are found in the spectral range above ≈130 cm^{-1}.

The analysis of the surface Raman spectra is further extended to the temperature dependence of some peaks. The dependence is shown for the eigenmodes at 185.5, 331.8, and 385.5 cm^{-1} in Fig. 3.24(b). The temperature influence on both the frequency and the FWHM of these peaks is considered and fitted to theoretical models. The used model takes anharmonic effects into account and predicts a temperature dependence of the form [192]:

$$\Delta(T) = A\left(1 + \frac{2}{e^x - 1}\right) + B\left(1 + \frac{3}{e^y - 1} + \frac{3}{(e^y - 1)^2}\right), \tag{3.6}$$

where $x = \frac{\hbar\omega_0}{2k_B T}$ and $y = \frac{\hbar\omega_0}{3k_B T}$. The first term on the right-hand side in Eq. (3.6) accounts for three-phonon decay processes, while in the second term also contributions of four-phonon decay processes are included. For the case of temperature-induced frequency shifts, to the result of Eq. (3.6) the frequency ω_0 for purely harmonic vibrations has to be added to get the total Raman shift. For the FWHMs, Eq. (3.6) can be directly applied. The resulting fits are included in Fig. 3.24(b). As expected,

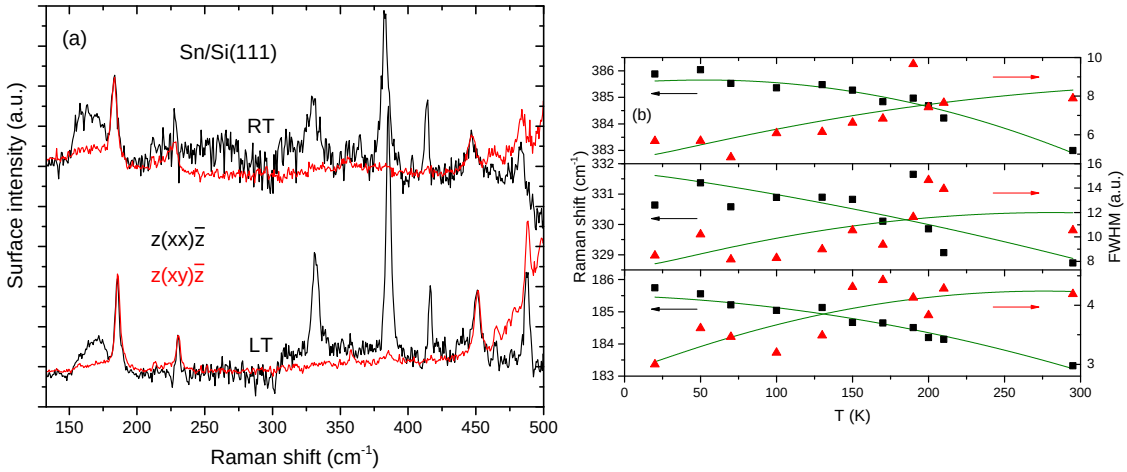

Figure 3.24.: Surface Raman spectra of Sn/Si(111) (a) at RT and LT for both polarization configurations and (b) the temperature development of the frequency values and FWHMs of several prominent peaks of Sn/Si(111). For details of the model fits see text.

the fit shows that the coefficient A outnumbers B by several orders. This is due to the fact that processes with three phonons are way more probable than processes involving more phonons. For the peaks in the lower and upper panel in Fig. 3.24(b), the fitted curves model the data quite well and satisfactorily. However, for the middle panel the fit is less exact, but the tendencies are in agreement with theory. This peak lies in the steep edge of the 2TA(X) of bulk Si(111) which partly obscures the peak and impedes its evaluation. As an important result of these fits, one can state that these surface phonons show a temperature dependence as expected also for bulk phonons.

Before the discussion will focus on the low-frequency spectral region of Sn/Ge(111) and Sn/Si(111), it is worth noting a remarkable similarity between both materials in the Raman spectra above. At RT, both surface systems are believed to behave alike and a direct comparison is therefore justified. By taking the frequency ratio of the two distinct peaks at 183.5 cm^{-1} for Sn/Si(111) and at 102.6 cm^{-1} for Sn/Ge(111) and compare it to the frequency ratio of the LTO phonon modes of bulk Si(111) and bulk Ge(111), it matches quite well. The ratios differ only by $\approx$3 %. A conclusion that can be drawn is that both vibrational modes have a similar origin and that the Sn adatoms do not have a great impact on these modes. The assumption that the displacement patterns of both eigenvibrations are related is also supported by their equal polarization behavior.

Table 3.6.: Vibrational peak frequencies (in cm^{-1}) for the surface reconstructions of Sn/Ge(111) (above ≈80 cm^{-1}) and Sn/Si(111) (above ≈130 cm^{-1}). For both systems, the SRS results for RT and LT are presented for $z(xx)\bar{z}$ polarization configuration together with the mode symmetries.

Sn/Ge(111)			Sn/Si(111)		
RT	LT	Sym.	RT	LT	Sym.
82.1	82.3	A_1	118.0		A_1
88.3	89.6	E	165.6	169.9	A_1
95.8	96.6	E	183.5	185.5	E
102.6	104.9	E	227.8	230.5	E
111.9	113.4	E	328.6	331.8	A_1
119.2	120.7	E	382.9	385.5	A_1
132.4	135.2	E	413.7	416.4	A_1
184.8	188.8	A_1	447.1	450.5	E
192.5	194.7	E	482.9	487.5	E
217.8	219.9	E			
222.4	223.6	E			
238.8	241.1	A_1			
	246.1	A_1			
254.1	257.0	E			
	269.8	E			
271.1	276.3	E			
280.7	285.2	A_1			

3.4.5. Low-frequency modes of Sn/Ge(111) and Sn/Si(111)

So far, the shown Raman spectra of Sn/Ge(111) and Sn/Si(111) at higher frequencies exhibit a variety of Sn-induced Raman response. Now, the emphasis will be on the low-frequency surface Raman spectra of both surface systems. In this spectral region, vibrational features that are closely related to the DF model are expected (see Sec. 3.4.1). Moreover, the different temperature behavior, i.e., the occurrence of a SPT or its absence, is also expected to be reflected in the Raman spectra.

Only for the low-frequency spectral range of Sn/Ge(111), there exist HAS measurements that were fitted by a second-nearest-neighbor coupling model [188,193]. Additionally, there are DFT calculations in combination with a force constant model [164]. For Sn/Si(111), only DFT data are available [164]. These results are compared to the surface Raman spectra.

Low-frequency modes of Sn/Ge(111)

The Raman spectra of Sn/Ge(111) show distinct peaks in the lower spectral range as can be seen in Fig. 3.25(a). The spectra are shown for RT and LT as well as for both polarization configurations. At RT, there is a sole peak at 55.6 cm^{-1} in the $z(xx)\bar{z}$ and $z(xy)\bar{z}$ spectrum. This peak shifts only marginally to 55.8 cm^{-1} for LT. It is associated with the DF mode depicted in the upper part of Fig. 3.22. All Sn atoms move in phase and all displacement vectors are orientated orthogonally to the surface [188,190]. However, this mode has small admixtures of other eigenmodes. The measured Raman frequency for the DF mode is in good accordance with DFT calculations in combination with a force constant model (65 cm^{-1} with an error of 16 %) [164] and HAS experiments and its fitting to a second-nearest-neighbor model (55 cm^{-1}) [188]. The frequencies of the other two DF modes, that were used to interpret the surface phonon dispersions obtained by HAS, could not be clearly observed in SRS. Their location at 22 and 34 cm^{-1} is in an inaccessible spectral range since it is too close to the laser line.

The insignificant shift of the DF mode of $\approx$0.2 cm^{-1} ($\simeq$0.4 %) to higher wavenumbers with decreasing temperature is in the range of the spectral peak position accuracy (cf. vertical line in Fig. 3.25(a)). As can be seen from Fig. 3.24(b), the usual temperature induced shift accounts to several cm^{-1}. Therefore, the small shift of the DF mode is a strong hint that the mode is mainly of harmonic character. Theoretically, a harmonic mode is not influenced by temperature (see Sec. 2.1). This is well in line with calculations that predict this mode to be a harmonic oscillator that is only weakly coupled [188,190]. The HAS data also suggest that temperature has only a small impact on the frequency [188], but a distinct determination is not as exact as from the SRS data. Furthermore, this mode is apparently almost not affected by the response of the substrate material to thermal changes. In contrast to the frequency shift, the FWHM decreases by $\approx$0.7 cm^{-1} ($\simeq$19 %) from RT to LT. This decrease is in the same range as observed for the LTO phonon of Ge(111).

The most important temperature induced change in Fig. 3.25(a) is the appearance of a shoulder on the low-frequency side of the DF mode. The center of the shoulder is located at 49.6 cm^{-1} at LT. This is a strong indication for a SPT.

The SPT in the DF model relates the $(\sqrt{3}\times\sqrt{3})$ and (3×3) reconstructions. The corresponding SBZs are depicted in Fig. 3.26(a). According to calculations, this transition is mediated by a soft phonon [164], whose frequency declines to zero at the $\bar{K}$ point of the $(\sqrt{3}\times\sqrt{3})$ SBZ ($k = 0.6\,\mathrm{Å}^{-1}$ in $[11\bar{2}]$ direction). This is depicted in Fig. 3.26(b) as well as its renormalized to a nonzero value at RT. This $\vec{k}$ point then becomes the $\bar{\Gamma}'$ point of the (3×3) reconstruction. The softening, however, cannot be observed directly by SRS.

Therefore, the SPT is accompanied by a folding of the SBZ. This folding affects all vibrational modes. Moreover, this includes modes that are not observed in the RT Raman data so far, e.g., a RW that is observed in the HAS data [188]. The

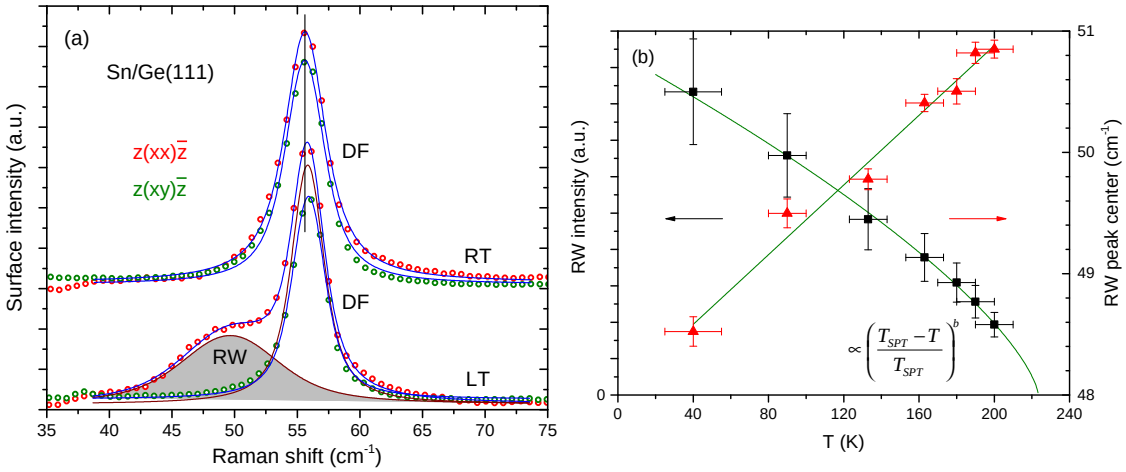

Figure 3.25.: Low-frequency surface Raman spectra of (a) Sn/Ge(111) at RT and LT for both polarization configurations and (b) the temperature-dependent evaluation of the RW shoulder (peak intensity and center) appearing of LT. The fit functions are a power law and a linear fit, respectively.

shrinkage of the SBZ due to the SPT results in the backfolding of this RW (cf. inset of Fig. 2.1). The frequency of the backfolded RW at the $\bar{\Gamma}$ point is determined to be $50\,\mathrm{cm}^{-1}$ by HAS. Therefore, the shoulder of the DF mode in the Raman spectrum is explicitly attributed to the backfolded RW. A further backfolded RW branch at $\approx 70\,\mathrm{cm}^{-1}$ was predicted by HAS (and the subsequent fitting of the data) for both temperatures. It is due to folding by in-plane and out-of-plane reciprocal vectors. In the Raman spectra, no indications are observed in that certain spectral range, which might be due to its weak Raman scattering efficiency. All SRS peaks as well as the results of other methods are summarized in Tab. 3.7.

The investigation of the SPT is further extended by considering the temperature dependence of the RW. The development of the RW intensity with temperature is plotted in Fig. 3.25(b). The intensity decreases with increasing temperature until it vanishes completely. The data points are fitted by a power law of the form [157]:

$$I_{\mathrm{RW}} \propto \left(\frac{T_{\mathrm{SPT}} - T}{T_{\mathrm{SPT}}} \right)^{b}, \tag{3.7}$$

where I_{RW} is the intensity of the RW and b is a fitting parameter. The Raman data suggest a phase transition temperature of $T_{\mathrm{SPT}} \approx 225\,\mathrm{K}$. This matches very well with the reported temperature of $T_{\mathrm{SPT}} \approx 220\,\mathrm{K}$ which was determined by HAS in Ref. [157]. Interestingly, the center position of the RW shoulder also shifts with temperature as can be observed in Fig. 3.25(b). But unlike the evaluated surface

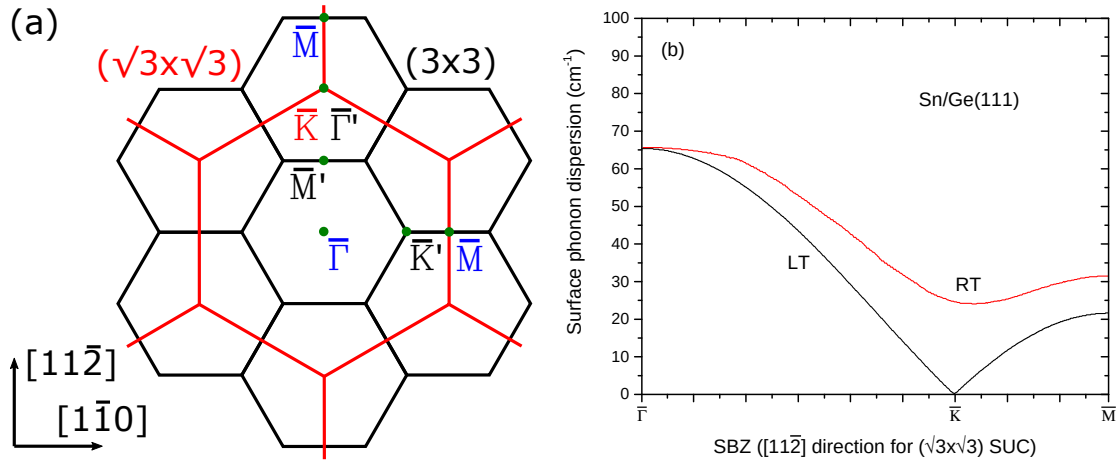

Figure 3.26.: Depictions of (a) the SBZs of the reconstructions $(\sqrt{3}\times\sqrt{3})$ (red) and (3×3) (black) for Sn/Ge(111) and (b) the surface phonon dispersions of Sn/Ge(111) at LT and RT for the $(\sqrt{3}\times\sqrt{3})$ SUC. Green dots mark high symmetry points along both crystal axes. Points with blue labels are shared by both reconstructions. Phonon dispersion data adapted from Ref. [164].

phonons of Sn/Si(111) (see Fig. 3.24(b)), the center of the RW increases with increasing temperature. This development is contrary to the usual temperature-induced frequency shift. The approximation by a linear fit is quite satisfactory over the whole temperature range. This further underscores the assumption of temperature-induced backfolding as origin.

The developments of the RW intensity can be conclusively interpreted within the DF model. For temperatures well above T_{SPT}, the Sn atoms in both height positions fluctuate randomly which inhibits a long-range order. When the temperature is lowered below T_{SPT}, the fluctuations start to freeze out resulting in adjacent (3×3) SUCs with the same order of height positions, i.e., UDD-UDD-UDD. With further decreasing temperature, the patches grow larger as shown schematically in Fig. 3.27. The patches exhibit a longer coherence length, which gives rise to the backfolded RW. Thus, the Raman measurements suggest the SPT to be of order-disorder type and that it is a second-order transition. This is also reported in Refs. [157,188,194], although phase transitions involving soft phonons are usually of displacive type [188].

For temperatures below 60 K, the predicted COI phase appears in coexistence with the so far discussed metallic (3×3) phase. While the latter forms a 1U2D configuration, the Sn atoms in the SUC of the COI phase are all on different heights above the substrate surface [173]. The Raman spectra are expected to reflect these

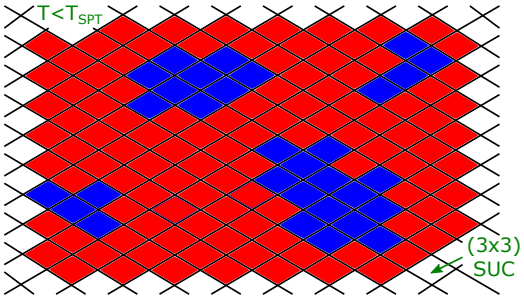

Figure 3.27.: Schematic depiction of the impact of the SPT on the Raman spectra of the Sn/Ge(111) surface within the DF model. Blue patches indicate coherently connected (3×3) SUCs, while red areas stand for randomly distributed (3×3) SUCs. The temperature is below the transition temperature T_{SPT}, but well above LT.

structural changes, if the abundance of COI SUCs is assumed to be high enough to be detectable. Since the COI phase has also a (3×3) pattern, the RW shoulder, which appears due to periodicity-induced backfolding, should not be affected (cf. Fig. 3.25(a)). However, if the Sn atoms at down positions are rearranged to different heights, the DF mode should be indeed altered. A possible scenario would be a splitting of the DF mode into a double peak, but a sole broadening is also imaginable. An obscuring of an additional peak by the shoulder can be excluded since this peak is assumed to appear in both polarization configurations as the DF mode. Yet, in the existing Raman spectra in Fig. 3.25(a) no hints for the COI phase can be observed. According to Ref. [173], the COI phase is connected with the vibrational mode depicted at the bottom right of Fig. 3.22.

The temperature dependence of both the DF mode and the RW shoulder can be directly observed in the Stokes Raman spectra in Fig. 3.28. At 200 K, the shoulder has almost completely vanished. The frequency shift of the shoulder with temperature is also apparent. Instead, the DF mode shows no changes with temperature. The figure also shows the anti-Stokes spectra for the same temperatures. The comparison of Stokes and anti-Stokes spectra has the comfortable advantage of excluding artifacts as origin of spectral features. Note that these Raman spectra are separately recorded from the spectra shown in Fig. 3.25(a). The DF modes are observed on both sides of the laser line and they do not shift considerable with temperature. The shoulder is also evident in the anti-Stokes spectra. At LT, modes at low frequencies, like the DF mode, can be still populated in accordance with the Bose-Einstein statistics (cf. Eqs. (2.9) and (2.10)). Nevertheless, the vibrational modes in the anti-Stokes spectra are strongly attenuated with decreasing temperature.

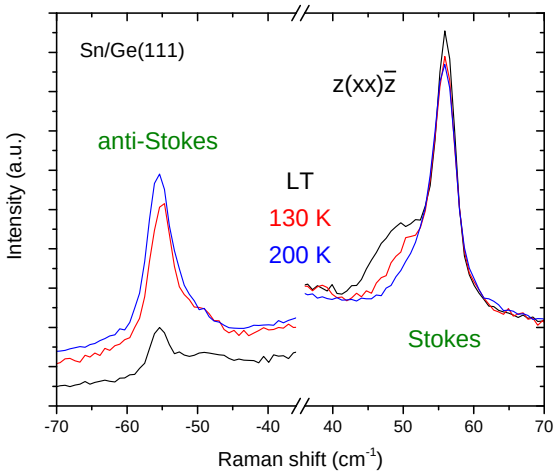

Figure 3.28.: Raman spectra of Sn/Ge(111) for $z(xx)\bar{z}$ at LT as well as 130 and 200 K. The DF peak and the RW shoulder are observed on the Stokes and anti-Stokes side. The spectra at 200 K are close to the transition temperature T_{SPT}.

Low-frequency modes of Sn/Si(111)

The Raman spectra of Sn/Si(111) show also clearly resolved peaks in the lower spectral range as displayed in Fig. 3.29. The main peak is observed at 85.9 cm^{-1} at RT for both polarization configurations. At LT, the peak shifts considerably to 88.3 cm^{-1}. It is attributed to the DF mode and is the counterpart of the DF mode of Sn/Ge(111) with the same eigenvectors. The frequency is in good agreement with DFT calculations in combination with a force constant model (81 cm^{-1} with an error of 7 %) [164]. Note the unusual intensity decline with decreasing temperature.

Unlike Sn/Ge(111), the frequency of the DF mode is shifted by 2.4 cm^{-1} ($\simeq$2.7 %) to higher wavenumbers when the sample is cooled from RT to LT. This value is in the same range as other surface phonons (cf. Fig. 3.24(b)) and this temperature shift can therefore be considered as usual. The Raman peak frequency and the theoretical results are appended to Tab. 3.7.

The origin of the DF modes as Raman features can be directly verified in Fig. 3.30(a) by comparison of the Stokes and anti-Stokes spectra. Therefore, artifacts can be excluded. A peak found at 118.0 cm^{-1} in the spectrum with $z(xx)\bar{z}$ polarization configuration in Fig. 3.29 and marked by an arrow is also observed in the separately recorded Raman spectra in Fig. 3.30(a). The intensity of this peak vanishes completely at LT. The peak is appended to Tab. 3.6. The Raman structures in Fig. 3.30(a) are already observed in Figs. 3.24(a) and 3.29 for RT.

The appearing peaks in Fig. 3.30(a) may be explained with the aid of the surface phonon dispersion of Sn/Si(111) displayed in Fig. 3.30(b). Together with the phonon dispersion for the $(\sqrt{3}\times\sqrt{3})$ SUC, the surface PDOS is plotted. The PDOS, deduced

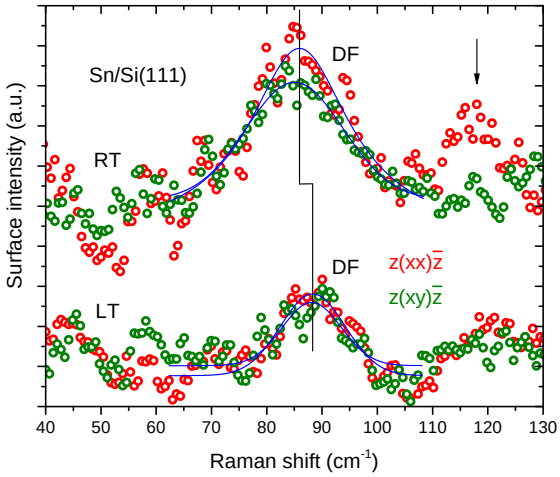

Figure 3.29.: Low-frequency surface Raman spectra of Sn/Si(111) at RT and LT for both polarization configurations. Note the peak at ≈120 cm^{-1} marked by an arrow.

from the phonon dispersion, exhibits three maxima due to the flat dispersion regions at the high symmetry points. The maximum of the $\bar{\Gamma}$ point of the SBZ is readily attributed to the DF mode in the Raman spectra. The next two Raman peaks can be associated with second-order processes. The first peak might be due to contributions of the $\bar{M}$ point which accounts to ≈100 cm^{-1}. The discrepancy to the measured frequency of 118.0 cm^{-1} might be explained by renormalization due to the elevated temperatures, similarly to the case of Sn/Ge(111). The broad Raman peak at 165.6 cm^{-1} is close to the double frequency value of the DF mode. Assuming the measured frequency of the first-order DF mode at RT as exact, the second-order peak is lower in frequency according to $2 \cdot 85.9\,\mathrm{cm}^{-1} > 165.6\,\mathrm{cm}^{-1}$. This is not surprising since the phonon dispersion curve declines when the $\bar{\Gamma}$ point is departed and the second-order Raman process is not confined to the $\bar{\Gamma}$ point. Another hint towards this assumption is that both peaks are predominantly observable in the spectrum with $z(xx)\bar{z}$ polarization configuration, which is typical for second-order processes. The Raman peak at 183.5 cm^{-1} was already discussed thoroughly in Sec. 3.4.4.

Comparison of Sn/Ge(111) and Sn/Si(111)

The presented Raman results of Sn/Ge(111) and Sn/Si(111) are very well described within the DF model and thus constitute a strong experimental support for this model. Finally, the investigation is extended here by a comparison of both systems.

The low-frequency spectra shown so far exhibit many similarities, but also some differences. For a comprehensive overview all relevant data for the low-frequency spectral range of Sn/Ge(111) and Sn/Si(111) are tabulated in Tab. 3.7.

A remarkable difference is that the DF mode in the Raman spectra of Sn/Ge(111)

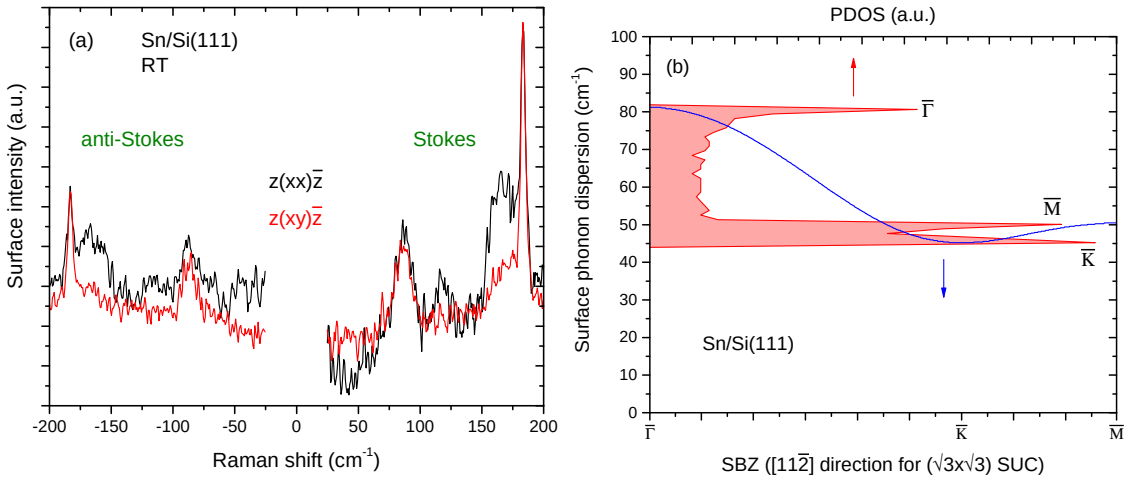

Figure 3.30.: Depiction of (a) the surface Raman spectra of Sn/Si(111) at RT for $z(xx)\bar{z}$ and $z(xy)\bar{z}$ and (b) the surface phonon dispersion (blue) and PDOS (red) of Sn/Si(111) for the $(\sqrt{3} \times \sqrt{3})$ SUC. All Raman peaks are observed on the Stokes and anti-Stokes side. Phonon dispersion data adapted from Ref. [164].

does virtually not shift with temperature, while the DF mode of Sn/Si(111) undergoes the usual temperature shift. Having the different LT behavior in mind, this could be a good starting point for a further evaluation of the SPT in Sn/Ge(111). The absence of anharmonic terms only for the DF mode in Sn/Ge(111) might be due to electronic correlations.

In turn, a comparison of the frequencies of the DF modes at RT of Sn/Ge(111) ($\omega_{\mathrm{Sn/Ge(111)}} = 55.6\,\mathrm{cm}^{-1}$) and Sn/Si(111) ($\omega_{\mathrm{Sn/Si(111)}} = 85.9\,\mathrm{cm}^{-1}$) reveals a close connection. A consideration at RT is needed since both systems are proposed to behave similar at high temperatures [164]. The shown Raman spectra indicate that both DF modes are related and have similar eigenvectors [195], which can be also evaluated qualitatively. In general, the vibrational frequencies are material-dependent according to the formula [196]:

$$\omega \propto \mu^{-\frac{1}{2}} d^{-\frac{3}{2}}, \tag{3.8}$$

where μ is the reduced mass of the involved elements and d is here the distance between Sn atoms and the atoms in the first layer of the Ge and Si substrate. The latter were reported to be $d_{\mathrm{Sn/Ge(111)}} = 2.760\,\text{Å}$ and $d_{\mathrm{Sn/Si(111)}} = 2.573\,\text{Å}$ as experimentally determined [197]. Thus, a comparison of the following ratios is

Table 3.7.: Low-frequency peak frequencies (in cm^{-1}) for the surface reconstructions of Sn/Ge(111) and Sn/Si(111). The SRS results are presented for RT and LT in polarization configuration $z(xx)\bar{z}$ together with the mode symmetries. The theoretical results of DFT calculations in combination with a force constant model are given for both models [164]. For Sn/Ge(111), HAS data are listed for RT and $T = 145\,K$ [188,193]. The type of the modes according to HAS are labeled as backfolded RW and DF.

	SRS			DFT	HAS		
	RT	LT	Sym.		RT	$T = 145\,K$	Type
Sn/Ge(111)						22	DF
						34	DF
		49.6	A_1			50	RW
	55.6	55.8	E	65	55	55	DF
					71	72	RW
Sn/Si(111)	85.9	88.3	E	81			DF

appropriate:

$$\frac{\omega_{\mathrm{Sn/Ge(111)}}}{\omega_{\mathrm{Sn/Si(111)}}} = 0.647 \tag{3.9}$$

compared to

$$\left(\frac{\mu_{\mathrm{Sn/Si(111)}}}{\mu_{\mathrm{Sn/Ge(111)}}}\right)^{\frac{1}{2}} \left(\frac{d_{\mathrm{Sn/Si(111)}}}{d_{\mathrm{Sn/Ge(111)}}}\right)^{\frac{3}{2}} = 0.639. \tag{3.10}$$

Due to the striking resemblance of both numerical values a close similarity of the modes is strongly suggested. This includes the displacement patterns of the modes and is further supported by the identical polarization properties. This also justifies the attribution of the upper DF mode in Fig. 3.22 to the low-frequency mode of Sn/Si(111).

All three DF modes of Fig. 3.22 of both systems Sn/Ge(111) and Sn/Si(111) conserve the symmetry properties of the point group C_{3v}. This is usually associated with A-like modes. However, the DF modes for both adsorbate surfaces appear in both polarization configurations $z(xx)\bar{z}$ and $z(xy)\bar{z}$, which is typical for E-like modes. This contradiction cannot be solved with the current knowledge of the systems.

3.4.6. Sn-$(2\sqrt{3} \times 2\sqrt{3})$/Si(111) and thin α-Sn films

With increasing coverage of Sn on Si(111) the $(2\sqrt{3} \times 2\sqrt{3})$ reconstruction is formed. This reconstruction is a precursor to a thin film of α-Sn [198]. Bulk α-Sn as well as films crystallize in the diamond structure, like Si and Ge (cf. Fig. 3.1). When the Sn coverage is raised considerably beyond $\frac{1}{3}$ ML, the Sn atoms tend to mimic the bonding configuration of the diamond structure. This can be regarded as an incomplete double layer of α-Sn(111) [198]. Thus, it is appropriate to consider these systems together. Both Sn-$(2\sqrt{3} \times 2\sqrt{3})$/Si(111) and α-Sn films are investigated by SRS and compared to the previously discussed Sn reconstructions on Si(111) and Ge(111).

Despite the differences in the lattice constants of α-Sn compared to Si and Ge, thin film growth of α-Sn on Si(111) was reported [199]. To achieve this, it was necessary to use the $(\sqrt{3} \times \sqrt{3})$ or $(2\sqrt{3} \times 2\sqrt{3})$ reconstruction as a template. For 3.5 ML, the formed film exhibited a compressed diamond-like structure. The α-Sn film considered in this thesis is much thicker and is grown on a substrate that matches closely with the lattice constant of bulk α-Sn.

Raman spectroscopy results for Sn-$(2\sqrt{3} \times 2\sqrt{3})$/Si(111)

An atomic structural model of the Sn-$(2\sqrt{3} \times 2\sqrt{3})$/Si(111) reconstruction is shown in Fig. 3.31(a). The model was initially proposed by Törnevik *et al.* [198] and was supported by a recent study [200]. Its key feature is a double Sn layer resulting in a Sn coverage of $\frac{14}{12}$ ML. The double layer is indicated in Fig. 3.31(a) by different colors: blue colored atoms belong to the lower layer, while orange and red colored atoms belong to the upper layer. Yet, the atoms marked in red are 1.5 Å higher than the orange ones. The Sn atoms of the upper dimer are located close to T_4 positions, while the ones of the lower dimer are located above H_3 positions. Furthermore, the Sn atoms in the upper layer are bound to the lower layer in a distorted tetrahedral configuration, leaving each Sn atoms with one DB. Note that also the two atoms on the short axis of the rhomb of the SUC have DBs [200].

The Sn-$(2\sqrt{3} \times 2\sqrt{3})$/Si(111) surface has only a mirror plane symmetry and therefore belongs to the C_s point group. The selection rules are similar as for Au-(5×2)/Si(111), but with the mirror plane instead of a glide plane as the relevant symmetry element. Therefore, for the Sn-$(2\sqrt{3} \times 2\sqrt{3})$/Si(111) reconstruction another space group, i.e., $c1m1$, applies [200,201].

The LEED pattern of the Sn-$(2\sqrt{3} \times 2\sqrt{3})$/Si(111) reconstruction is shown in Fig. 3.31(b). Between the (1×1) spots, distinct superstructure spots appear. Some spots near the center are hidden by the electron gun. Note that the innermost red marked spot is also observed for the $(\sqrt{3} \times \sqrt{3})$ reconstruction. The $(2\sqrt{3} \times 2\sqrt{3})$ SUC is also rotated by 30°.

The surface Raman spectra of the Sn-$(2\sqrt{3} \times 2\sqrt{3})$/Si(111) surface are shown for both polarization configurations at LT in Fig. 3.32. Since the LT spectra are better

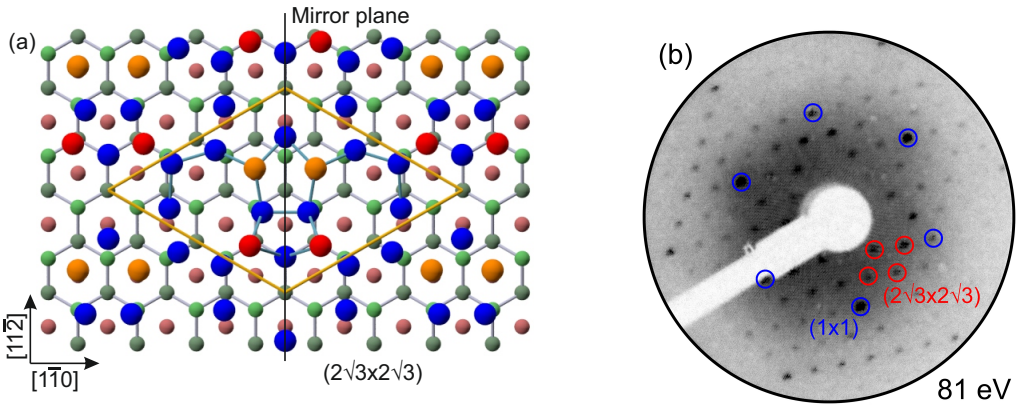

Figure 3.31.: Depiction of (a) the atomic surface structure and (b) the LEED pattern of the Sn-$(2\sqrt{3} \times 2\sqrt{3})$/Si(111) surface reconstruction. Sn atoms are colored in red and orange (upper layer) as well as in blue (lower layer). The LEED pattern was recorded at RT and with an electron energy of 81 eV. Structural data adapted from Ref. [202].

resolved than the ones at RT, the discussion is restricted to LT. The first peak is centered at 60.3 cm^{-1} and is only clearly appearing in $z(xx)\bar{z}$ polarization configuration. The following distinct peak is observed in both polarization configurations and has therefore a symmetry character of A′ and A″. It is located at 73.3 cm^{-1}. All following peaks predominantly appear only in $z(xx)\bar{z}$ configuration, although there are small humps in the spectrum with crossed polarization. Two peaks are located in a valley-like structure at 82.3 and 91.1 cm^{-1}. There are further peaks at 108.8, 119.7, 134.9, and 169.0 cm^{-1}. No additional Raman peaks are observed above ≈180 cm^{-1}. The Raman peak frequencies are summarized in Tab. 3.8. The spectra show a considerable increase of intensity close to the laser line which is attributed to strong diffuse stray laser light. Since for the Sn-$(\sqrt{3} \times \sqrt{3})$/Si(111) surface the diffuse light is much less intense, it is very likely that the buckling, i.e., roughness, of the $(2\sqrt{3} \times 2\sqrt{3})$ reconstruction is responsible for the increase. Nonetheless, the distinct Raman peaks are not obscured by this background intensity.

The details of the atomic structure, especially the number of Sn adatoms in a SUC, are still under discussion. This is mainly due to the fact, that the upper Sn layer prevents an observation of the lower Sn layer, for instance by STM [200]. If the presented SRS data of the Sn-$(2\sqrt{3} \times 2\sqrt{3})$/Si(111) reconstruction are compared to future calculations of the Raman intensity of this structure, further insights into structural details may be obtained.

The Sn-$(2\sqrt{3} \times 2\sqrt{3})$/Si(111) reconstruction can be clearly distinguished by SRS from other Sn-induced reconstructions on Si(111), i.e., the $(\sqrt{3} \times \sqrt{3})$ reconstruction. As illustrative example may serve the peak at 185.5 cm^{-1} of Sn-$(\sqrt{3} \times \sqrt{3})$/Si(111)

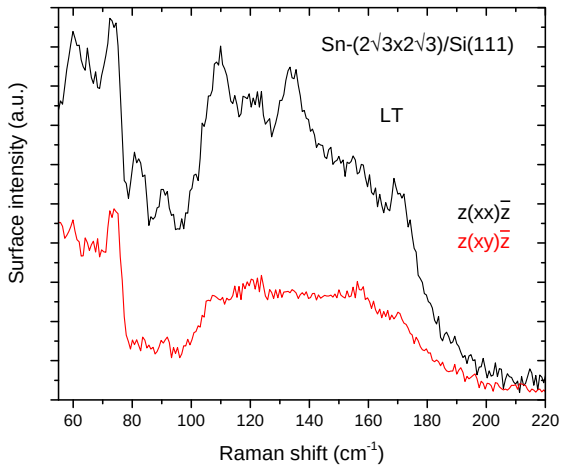

Figure 3.32.: Surface Raman spectra of the Sn-$(2\sqrt{3} \times 2\sqrt{3})$/Si(111) reconstruction. Both polarization configurations are shown for LT. The increasing intensity towards the laser line is due to diffuse stray light.

(see Fig. 3.24(a)), which is clearly not observed in the Raman spectra of Sn-$(2\sqrt{3} \times 2\sqrt{3})$/Si(111) in Fig. 3.32. Apart from this very satisfying finding in respect of distinguishability, the frequency of 185.5 cm^{-1} is close to the main phonon frequency of 200.0 cm^{-1} (LO and TO phonon at $T = 77$ K) of a thin α-Sn film (see below). Therefore, the disappearance of this $(\sqrt{3} \times \sqrt{3})$-related mode for the $(2\sqrt{3}\times2\sqrt{3})$ reconstruction is an astonishing discovery since the structural properties of Sn-$(2\sqrt{3} \times 2\sqrt{3})$/Si(111) are related to that of α-Sn. An explanation for this might be found in the different surface symmetries and the concomitant symmetry reduction. The point group C_{3v}, which is equal for Sn-$(\sqrt{3} \times \sqrt{3})$/Si(111) and the surface of α-Sn(111) (cf. Sec. 3.1), is reduced in the case of Sn-$(2\sqrt{3} \times 2\sqrt{3})$/Si(111) and only one mirror plane is applicable. When the eigenvector of the relevant mode is incompatible with this symmetry reduction, the mode could therefore disappear in the Raman spectrum of Sn-$(2\sqrt{3} \times 2\sqrt{3})$/Si(111), even when the atomic structure exhibits similar Sn configurations.

Raman spectroscopy results for thin α-Sn films

For comparison films of α-Sn(001), which are comparable to films with a (111) crystal surface, are studied by SRS. Bulk Sn undergoes a phase transition from metallic β-Sn (white tin) to semiconducting α-Sn (gray tin) below 286.4 K [203]. As a zero gap semiconductor α-Sn is of potential interest for IR devices [199]. Apart from the relationship to Sn adsorbate surface systems, the Raman spectra of the α-Sn films exhibit some further interesting effects.

The studied α-Sn films are grown by molecular beam epitaxy (MBE) [204]. During the MBE process the different constituents are evaporated and impinge on the substrate surface where they rearrange to the desired material. The growth

Table 3.8.: Vibrational peak frequencies (in cm^{-1}) of the Sn-$(2\sqrt{3} \times 2\sqrt{3})$/Si(111) reconstruction. The SRS data are given for $z(xx)\bar{z}$ polarization configuration for LT. Additionally the symmetry is listed for each mode.

SRS	
LT	Sym.
60.3	A′
73.3	A′, A″
82.3	A′
91.1	A′
108.8	A′
119.7	A′
134.9	A′
169.0	A′

can be tuned by varying growth parameters like the flux of the effusion cells and the temperature of the substrate. The lattice constant of the substrate should match the one of the deposited material. Therefore, a GaAs(001) substrate wafer is overgrown with ZnTe and CdTe for lattice matching. This procedure is a promising alternative for the usual application of InSb as a substrate for α-Sn. All these substrate materials crystallize in zinc blende structure, which is closely related to the diamond structure. Subsequently, a Sn film of 42 nm is grown on top of the substrate. Finally, the sample is capped with amorphous Se (≈1 nm) for protection, e.g., against oxidation. The sample was grown by S. Schreyeck. For the Raman measurements, the laser power was lowered (≈40 mW for RT and ≈20 mW for 77 K) to avoid uncontrolled heating in the region of the laser spot on the sample and therefore a phase transition to β-Sn.

The Raman spectra of a thin α-Sn film are shown in Fig. 3.33 at RT and $T = 77$ K. The main peak of α-Sn is located at 200.0 cm^{-1} at 77 K and 196.9 cm^{-1} at RT. These values agree very well with the one of 197.4 cm^{-1} reported for (001) films in the same thickness range for RT [203]. The peak is almost completely absent in $z(xy)\bar{z}$ polarization configuration (see inset of Fig. 3.33), which is in line with selection rules for (001) surfaces of crystals with diamond structure. Note that the used axes in the Porto notation are adapted here for a (001) surface. For this surface only the LO phonon is allowed. It may appear for the $z(xx)\bar{z}$ polarization configuration and is forbidden in the $z(xy)\bar{z}$ spectrum [12]. The FWHM of the α-Sn peak at 77 K is quite small with a value of 2.6 cm^{-1}. For comparison, the FWHMs of the LTO phonons of Ge(111) and Si(111) at LT are 3.2 and 2.7 cm^{-1}, respectively. These line widths are all determined by the same Raman setup and are therefore directly comparable (cf. Sec. 3.1). The small FWHM of the α-Sn peak together

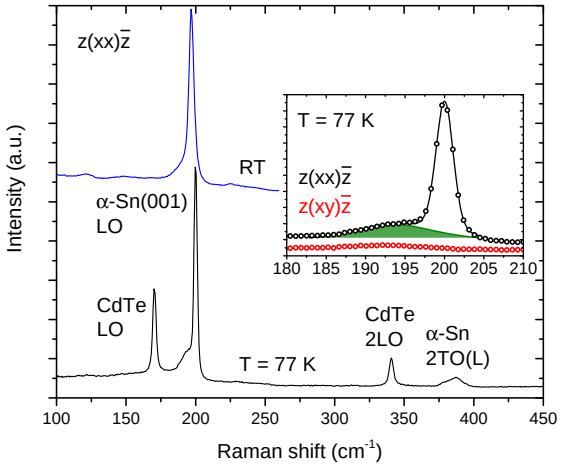

Figure 3.33.: Raman spectra of a thin α-Sn film with a thickness of 42 nm. The crystal axes for the polarization configurations are $x = [110]$, $y = [1\bar{1}0]$, and $z = [001]$. The spectra are shown for RT and $T = 77$ K. The inset zooms on the shoulder (green) of the LO phonon of α-Sn which is due to isotopical disorder in natural Sn.

with the perfect compliance of the selection rules suggest a very good crystal quality and a low defect density. Note that the Raman peak of the CdTe substrate layer is still observed and originates only from the LO phonon [205]. The split TO phonon is not observed due to selection rules. The intensity of the CdTe peak is only weak since α-Sn has a high absorption coefficient [206] and vanishes completely at RT due to the weak Raman scattering efficiency of CdTe [207]. At higher frequencies, Raman peaks that are assigned to second-order processes are observed. Besides the second-order peak of the LO phonon of CdTe, there is a feature that is identified with the 2TO(L) phonon of α-Sn [206]. In the Raman spectra at both temperatures, there are no hints of other phases of bulk Sn or other materials (e.g., amorphous Se, SnSe, or SnO [208–210]). Especially, no indications are found for β-Sn which has a TO phonon mode at $\approx$130 cm^{-1} in the here accessible spectral range [211,212]. The studied sample shows no phase transition to β-Sn at RT due to the stabilizing effect of the substrate as was also observed in Ref. [203].

In general, phonons confined to very thin films or other nanostructures may show frequency shifts to lower frequencies and broadening of the spectral line shape. This impact was investigated for Si particles down to several nm in mean diameter [213–215]. Transferred to the α-Sn films, it can be concluded that the films are thick enough that the phonon properties are not substantially altered by confinement.

Remarkable is the pronounced shoulder on the low-frequency side as marked by green shading in the inset in Fig. 3.33. It is also present in $z(xy)\bar{z}$ polarization configuration as small hump. Amorphous Sn as origin for the shoulder can be excluded since the intense TO maximum of the PDOS is located at $\approx$186 cm^{-1}

and therefore below the shoulder [13]. As shown for amorphous Si, the Raman spectrum of amorphous semiconductors resembles the PDOS and a peak at the TO maximum would be expected for this reason [93]. However, an explanation for the shoulder is found in isotopical disorder in the α-Sn film [216]. Natural Sn consists of considerable parts of different stable Sn isotopes that are randomly mixed in the crystal lattice. This breaks the translational invariance of the crystal. Therefore, the momentum conservation like formulated in Eq. (2.4) does not apply strictly [42]. Regions of the phonon dispersion which are more distant from the BZ center can contribute and generate the shoulder in the Raman spectra. The polarization configuration of the shoulder of α-Sn corresponds to the polarization behavior of a shoulder measured for natural Ge due to the same effect [217].

3.5. Conclusion

The presented Raman spectra of Au/Si(111), Sn/Ge(111), and Sn/Si(111) show clearly additionally emerging Raman peaks that can be attributed to surface phonons. Moreover, the Raman data are capable of distinguishing between different adatom reconstructions on the surface. The vibration-induced Raman signatures can be therefore considered as individual fingerprints.

Additional information is acquired by recording polarization- and temperature-dependent Raman spectra. Therefore, SRS allows the determination of mode symmetries as well as the observation of temperature-dependent structural changes. Through these phase transitions, insights in physical effects can be gained and a transition temperature can be extrapolated. Furthermore, in combination with first-principles calculations, on basis of the SRS data a differentiation between several structural models for the surface reconstructions is feasible. Moreover, experimentally observed vibrational modes can be attributed to specific frequencies, eigenvectors, symmetries, and localization.

For all investigated adsorbate systems, in dependence of the used substrate, the frequency ranges in which the surface vibrations are observed are almost identical. In accordance with theoretical relations, the vibrational frequencies of the surface vibration modes are below the LTO phonon frequencies of the semiconductor substrates. This especially holds for the heavier adatoms Au and Sn, where the Au-induced surface modes are in general located at lower frequencies than the Sn-induces modes. Also for the clean surfaces, which are covered with adatoms of the same atomic species, the mode frequencies decline due to the altered bonding configuration of the surface atoms.

By comparison of the surface Raman spectra of the different surface adsorbate systems, noticeable crosslinks can be established. There are Raman peaks that appear to be universal in the sense that they are observed irrespective of the adsorbate species and the actual reconstruction. The following examples suggest

that the surface region of the substrate might be the origin for these peaks. For the Au-($\sqrt{3}\times\sqrt{3}$)/Si(111) reconstruction, the vibrational modes at 401.2 and 418.6 cm^{-1} are identified to be mainly located at the Si substrate surface region. Similar modes are observed for the Sn-($\sqrt{3}\times\sqrt{3}$)/Si(111) reconstruction which are located at 385.5 and 416.4 cm^{-1}. The accordance of the latter frequency values is astonishing, while the former ones seem to be more influenced by the adsorbates. Moreover, all peaks are observed in the same polarization configuration. In hindsight, this also confirms the attribution of the modes of Au-($\sqrt{3}\times\sqrt{3}$)/Si(111) to the Si atoms in the surface region. The occurrence of these modes is related to steps on the surface substrate as shown for Au/Si(hhk). A further example is the mode at 335.8 cm^{-1} of Au-(5×2)/Si(111), which was also observed for Au/Si(hhk). A similar mode of Sn-($\sqrt{3}\times\sqrt{3}$)/Si(111) observed at 331.8 cm^{-1} matches quite well and shares possibly the same origin. These relations between separately obtained surface Raman spectra of different surface systems are extremely gratifying and further proof SRS to be a reliable experimental method.

For all studied surfaces, it is important to note that, different from STM for instance, no explicit selection of a spatial region on the surface is possible. Hence, in the comparatively large Raman probing spot, domain walls, defects and other changes in the periodicity influence the Raman spectra. This needs to be taken into account for the interpretation of the spectra.

4. Surface intermetallic systems

In this chapter, ultrathin intermetallic films on metal substrates are studied. Intermetallic systems are compounds of two or more metals. In contrast to alloys, intermetallic compounds do not adapt the crystal structure of their constituents [218]. Here, alternatively Ce or La is used as one part of the binary compound system and is deposited onto the Pt(111) substrate, which constitutes the other part. The intermetallic compound systems Ce-Pt and La-Pt are then alloyed directly on the surface of the substrate. The used terminology concerning intermetallics and alloys follows Ref. [219].

The phase diagram of the Ce-Pt system shows a large variety of stable intermediate phases [220]. One of these is the binary intermetallic compound $CePt_5$ which is of special interest here. The extension to thin films of Ce-Pt compounds on a Pt(111) crystal was provided by Tang *et al.* [221]. These films crystallize in the same structure as bulk $CePt_5$ [222,223]. For the related La-Pt system, the phase $LaPt_5$ also exists [224] and thin films on Pt(111) show a similar structure like $CePt_5$ [225,226].

Intermetallic systems that contain Ce atoms host $4f$ electrons, which are localized at the Ce nuclei and keep their atom-like character. The $4f$ electrons of Ce are enclosed by $5s$ and $5p$ electron shells [142]. Furthermore, the $4f$ electrons can interact with conduction electrons leading to hybridization and to various new physical phenomena, e.g., Kondo and heavy fermion physics [142]. To determinate the influence of the $4f$ electrons, it is useful to investigate in parallel for comparison a structurally similar material system without these electrons. Hence, it is reasonable to substitute Ce ($4f^1$) with La ($4f^0$) and compare the intermetallic systems $CePt_5$/Pt(111) and $LaPt_5$/Pt(111).

Important emerging phenomena that are expected for materials containing $4f$ electrons are described in the next section. These physical effects are also related to experimental and theoretical results observed for $CePt_5$/Pt(111). As pointed out in Ch. 2, RS is capable of analyzing vibrational excitations and more importantly electronic excitations that may involve $4f$ electrons and their modification by the CF. In contrast to INS, which is commonly used for the investigation of CF splitting schemes of bulk materials, SRS can also cope with small sample volumina, i.e., thin films. However, until now only bulk samples were subject of electronic Raman measurements on $4f$ electrons [227–230].

This work was realized in close cooperation with K. Fauth and M. Zinner from Experimentelle Physik II of the Universität Würzburg. The investigation of

$CePt_5$/Pt(111) and $LaPt_5$/Pt(111) by RS was also subject of the B.Sc. thesis of R. Hölldobler which was prepared during the course of this work [231]. Most parts of the results presented in this chapter are published in Refs. [232,233].

4.1. Kondo effect and heavy fermion physics

Following the considerations of correlated electron systems in Sec. 3.3.1, strong correlations are also found for the intermetallic compounds that are in the focus of this chapter. In addition to the conduction electrons, here are extra $4f$ electrons involved which cause new physical effects [234,235].

For metals containing small amounts of magnetic impurities, e.g., the spin of $4f$ electrons, an increasing electrical resistance was observed upon cooling below a certain temperature. This temperature behavior cannot be explained within Matthiessen's rule, which states a constant resistance for extrapolation to $T \to 0\,\mathrm{K}$ [236]. Early observations of the resistivity development could not be explained nor explicitly related to diluted magnetic impurities. Several decades later, a theoretical model was proposed by Kondo that explained the reincrease of resistance and related it to the magnetic impurities [237]. The phenomenon therefore is known as Kondo effect. The conduction electrons interact with the localized magnetic ions through spin-flip scattering (s-d exchange interaction) [142]. The Kondo temperature T_K determines a characteristic temperature below which this scattering becomes relevant. However, the solution of Kondo has the main problem that the resistivity diverges logarithmically for $T \to 0\,\mathrm{K}$. For a more realistic description it has to be considered that below T_K, the conduction electrons can screen the magnetic moments of impurities by forming a Kondo cloud with opposite spin. The resulting singlet states have a binding energy of $k_\mathrm{B}T_\mathrm{K}$ (in relation to the unscreened magnetic state). For $T \to 0\,\mathrm{K}$, the magnetic moments are therefore reduced to zero by the so-called Kondo screening and the restistivity does not diverge [142].

When the density of the impurities increases, it is more appropriate to speak of a Kondo lattice with impurities in each UC of a crystal [238]. For these lattices, the screening Kondo clouds of the conduction electrons overlap enabling interimpurity interactions [237]. Especially for Kondo lattices containing Ce atoms the $4f$ electrons can become itinerant at low temperatures [142]. The impurity bands hybridize with the conduction band electrons and form flat electron bands which are referred to as heavy fermions. This also leads to the opening of an energy gap at E_F [239,240].

A related effect found in systems with $4f$ electrons is the Ruderman-Kittel-Kasuya-Yosida (RKKY) interaction [236]. The spins of the localized $4f$ electrons cannot couple directly because of the small overlap of their wave functions. However, the $4f$ spins can be arranged in ferromagnetic or antiferromagnetic order due to mediation by polarization of the spins of the conduction electrons. The magnetic ordering by RKKY interaction competes with the paramagnetic state of a Kondo

system [238].

For ultrathin $CePt_5$ films in the material system $CePt_5$/Pt(111), Kondo screening was observed by x-ray absorption spectroscopy (XAS), x-ray linear dichroism (XLD), and x-ray magnetic circular dichroism (XMCD) experiments [241,242]. Instead, no Kondo interactions were reported for bulk $CePt_5$ [243]. The Kondo temperature of the $CePt_5$/Pt(111) system varies with film thickness. As obtained by XAS measurements, the Kondo temperature rises from $T_K \approx 125\,K$ for 1 UC to $T_K \approx 200\,K$ for 4 UC [241]. The nominal film thickness t_{nom} is specified here in multiples of UCs in direction normal to the surface (1.0 UC $\approx$ 0.44 nm). From the XMCD measurements, the temperature-dependent magnetic susceptibility can be deduced which provides access to the magnetic moments of the $4f$ electrons. A model for fitting the susceptibility depends on both the Kondo screening and the CF splitting scheme [242,244]. Since it is difficult to estimate both contributions only by the fits, an independent direct determination is recommendable. For the CF levels, this requirement is met by SRS focusing on the electronic excitations. The CF splittings, that are obtained by SRS, can be inserted into the model fits and also compared with the already existing results of the fits.

4.2. Preparation of $CePt_5$/Pt(111) and $LaPt_5$/Pt(111)

The $CePt_5$/Pt(111) and $LaPt_5$/Pt(111) samples are prepared under similar conditions in the mobile preparation chamber. The samples were prepared by M. Zinner.

The Pt(111) crystal is cleaned *in situ* by sputtering with Ar^+ ions ($E = 1\,keV$). Afterwards, the whole crystal is heated from the back side with e-beam heating to temperatures of 1170 K. This procedure is repeated until the LEED pattern shows a sharp (1×1) reconstruction.

Subsequently, Ce or La is deposited onto the clean Pt(111) substrate. The amount of Ce or La is adjusted to meet the required film thickness. The film is alloyed by heating to $T = 920\,K$ for $t = 5-10\,min$.

In a final step, the reconstruction is checked by LEED to ensure the quality of the surface.

For subsequent preparation of samples with varying film thicknesses, the intermetallic films can be completely removed by sputtering. Afterwards, a new preparation can be started.

4.3. Identification of electronic excitations in $CePt_5$/Pt(111)

For a thorough interpretation of the Raman spectra of $CePt_5$/Pt(111), the CF as well as the vibrational properties of $CePt_5$/Pt(111) must be known. Additionally, for comparison $LaPt_5$/Pt(111) is considered.

4.3.1. Crystal-field and vibrational properties

The $CePt_5$/Pt(111) system is investigated for several thicknesses of the $CePt_5$ films on the Pt(111) substrate. The film thicknesses of $CePt_5$/Pt(111) are in the range 1.0 – 18.0 UC. Accordingly, the $LaPt_5$/Pt(111) system is examined for comparison for similar film thicknesses in the range 2.5 – 12.0 UC. As basis for the following considerations, the crystal structure is initially presented in the next part.

Atomic structure and LEED pattern

There are two types of UCs for $CePt_5$ on Pt(111) substrate which both consist of stacked atomic layers. For the bulk UC, as shown in the lower part of Fig. 4.1, the hexagonal structure is generated by $CePt_2$ layers alternating with Pt layers in the kagome structure. The Ce atoms are thus embedded in an environment of Pt atoms, which constitute the CF and also its symmetry. This atomic configuration is also known as $CaCu_5$ structure and belongs to the 3D point group D_{6h} (corresponding 3D space group D^1_{6h}) [245].

According to a LEED-IV study and theoretical predictions, the regular kagome pattern of the Pt layers is altered at the topmost layer [246,247]. For the surface UC, the kagome hole position of the first layer is filled with an additional Pt atom as illustrated in the upper part of Fig. 4.1. The remaining layers in the UC are unchanged. Therefore, the symmetry is reduced at the surface to the 3D point group C_{6v} (corresponding 3D space group C^1_{6v}) compared to the bulk. The group C_{6v} results due to the lack of inversion symmetry for the surface UC. The relation $D_{6h} = C_{6v} \otimes C_i$ applies, where C_i is the point group of inversions [68].

A typical LEED pattern for a $CePt_5$/Pt(111) sample with a film thickness of $t_{\mathrm{nom}} = 16.0$ UC is depicted in Fig. 4.2. The apparent (2×2) reconstruction is truly squeezed and is thus labeled as compressed (2×2) [248]. Moreover, the LEED pattern depends crucially on the film thickness. The shown reconstruction appears for $t_{\mathrm{nom}} > 10$ UC and stays unchanged for thicker samples. Below, there are thickness ranges where rotated (by 30°) and non-rotated reconstructions and their superpositions are observed. The surface lattice constant also evolves in parts to higher and lower values with respect to the reconstruction of the thickest samples [241,248].

Since $LaPt_5$ is isostructural to $CePt_5$, the description of atomic structure and symmetry for $CePt_5$/Pt(111) applies for $LaPt_5$/Pt(111) as well [245]. This also holds

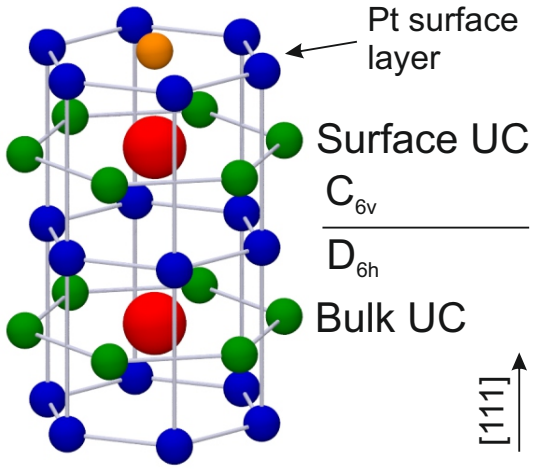

Figure 4.1.: Atomic structure of the $CePt_5$ UC. A stack of two different UCs is depicted together with the applying symmetry groups: the surface UC and the bulk UC. The Ce atoms are marked in red. All other atoms are Pt atoms. The surface is terminated by a Pt kagome layer with filled holes.

for the vibration properties of $LaPt_5$, e.g., number of eigenmodes and eigenvectors. The LEED pattern of $LaPt_5$/Pt(111) is similar to the one of $CePt_5$/Pt(111), but the above-mentioned thickness-dependent changes in the reconstruction appear already for lower film thicknesses (private communication with M. Zinner).

Crystal-field splitting and excitations

The $4f$ electron of Ce has the principal quantum numbers $n = 4$, $l = 3$, and $s = \frac{1}{2}$. The resulting state ^{2}F of the $4f$ electron is energetically split into two degenerate states through SOC (cf. Sec. 2.2). The state $^2\mathrm{F}_{\frac{5}{2}}$ with $J = \frac{5}{2}$ is the relevant ground state. It is clearly separated from the higher state with $J = \frac{7}{2}$ by $\approx$2100 cm^{-1} [249], which is therefore omitted in the further discussion. Mixing of these states is not expected.

The lower-lying electronic state with $J = \frac{5}{2}$ is further split by the CF into three twofold degenerate Kramers doublets with quantum numbers $M_J = \pm\frac{1}{2}, \pm\frac{3}{2}, \pm\frac{5}{2}$. For the double point group D_{6h} of the bulk, these Kramers doublets can be associated with the irreducible representations Γ_7^-, Γ_9^-, and Γ_8^-, respectively [42,75]. The resulting term diagram with included group theoretical indications is depicted in Fig. 4.3. Note that the orbital shape (and symmetry) of the electronic wave function combined with the spatial CF configuration (introduction of anisotropy) can have different impacts on the energy levels. For a hexagonal CF like in $CePt_5$, a mixing of the pure doublets does not take place [244].

Transitions between the CF states of the $4f$ electron in the double point group

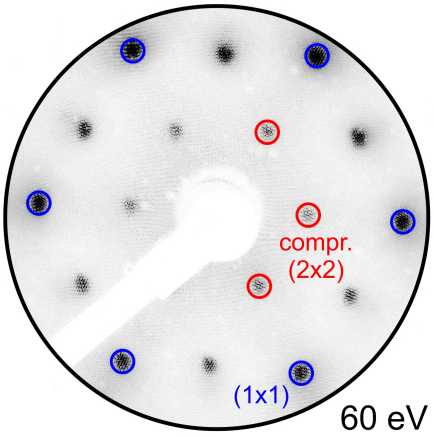

Figure 4.2.: LEED pattern of the $CePt_5$/Pt(111) intermetallic surface system exhibiting a compressed (2×2) surface reconstruction. The LEED pattern was recorded at RT and with an electron energy of 60 eV. The thickness of the $CePt_5$ film is $t_{\mathrm{nom}} = 16.0$ UC.

D_{6h} observed in electronic Raman scattering obey quadrupole selection rules (see Sec. 2.4). Since both the initial and final state belong to $J = \frac{5}{2}$, this yields $\Delta J = 0$ in line with the selection rules. Furthermore, transitions with $\Delta M_J = 0$ can be neglected since they do not contribute to the frequency-shifted Raman signal. By restriction to quadrupole transitions with $\Delta M_J = \pm 2$ due to the used scattering geometry, this yields the two possible transitions $\Gamma_7^- \leftrightarrow \Gamma_8^-$ $(\pm\frac{1}{2} \leftrightarrow \pm\frac{5}{2})$ and $\Gamma_7^- \leftrightarrow \Gamma_9^-$ $(\pm\frac{1}{2} \leftrightarrow \mp\frac{3}{2})$. The electron state $M_J = \pm\frac{1}{2}$ is involved in both transitions. A similar situation was also observed for $CeCl_3$ [74].

As described in Sec. 2.4, the direct products for both electronic transitions can be decomposed into irreducible representations:

$$\Gamma_7^- \otimes \Gamma_8^- = \Gamma_3^+ + \Gamma_4^+ + \Gamma_6^+, \tag{4.1}$$

$$\Gamma_7^- \otimes \Gamma_9^- = \Gamma_5^+ + \Gamma_6^+. \tag{4.2}$$

Note the change of parity of the representations according to Eq. (2.17). Both decompositions contain the irreducible representation Γ_6^+. According to the character table for the point group D_{6h} in Sec. B, this representation has the basis function $(x^2 - y^2, xy)$. All other representations are not of relevance since they are not observable in the Raman experiments with the used scattering geometry. Hence, both considered CF transitions cannot be distinguished by group theory only. As will be discussed below, this problem can be circumvented by the aid of other experimental methods.

The symmetry reduction at the surface does not change the electronic properties of the $4f$ electrons considerably since C_{6v} is a subgroup of D_{6h}. There is a one-to-one

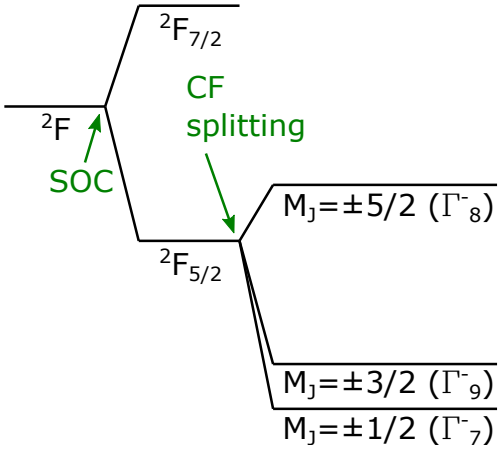

Figure 4.3.: Energy level scheme of the $4f$ electron in $CePt_5$/Pt(111) including the SOC and CF splitting. For the Kramers doublets the irreducible representations of the double group D_{6h} are also indicated.

relation between the representations of both double groups: $\Gamma_7^- \rightarrow \Gamma_7$, $\Gamma_8^- \rightarrow \Gamma_8$, and $\Gamma_9^- \rightarrow \Gamma_9$. Therefore, the electronic states at the surface are linked to the irreducible representations Γ_7, Γ_9, and Γ_8 of C_{6v}. The states are still Kramers doublets, but the superscript indicating the parity must be omitted due to the missing inversion symmetry. The selection rules for transitions can be accordingly adopted:

$$\Gamma_7 \otimes \Gamma_8 = \Gamma_3 + \Gamma_4 + \Gamma_6, \tag{4.3}$$

$$\Gamma_7 \otimes \Gamma_9 = \Gamma_5 + \Gamma_6. \tag{4.4}$$

Both transitions also share in their resulting direct products the Γ_6 representation, which has also the basis function $(x^2 - y^2, xy)$ (see Sec. B). For the other representations, the same considerations apply as in the case of D_{6h}.

According to this analysis, the CFE peaks are predicted to appear in the Raman spectra with $z(xx)\bar{z}$ and $z(xy)\bar{z}$ polarization configuration.

Vibrational eigenmodes

In analogy to the selection rules for electronic Raman scattering, the vibrational properties of the system can also be considered by group theory. The bulk UC of $CePt_5$ has a total number of 18 vibrational modes of which 15 are optical modes. In the bulk UC, the Ce atom occupies the Wyckoff position $1a$. The Pt atoms occupy $2c$ and $3g$ positions localized in the $CePt_2$ and Pt layers, respectively. With the aid of group theory the total number of normal modes and the associated symmetry

Table 4.1.: Vibrational modes and the linked Wyckoff positions for the point group D_{6h} of the bulk UC. Only the optical mode E_{2g} is Raman active. This table also contains the acoustic vibration modes $A_{2u} + E_{1u}$.

	A_{2u}	B_{1g}	B_{1u}	B_{2u}	E_{1u}	E_{2g}	E_{2u}
$3g$	1		1	1	2		1
$2c$	1	1			1	1	
$1a$	1				1		

properties of the vibrational patterns can be determinded (cf. Sec. 2.4). The results for the group D_{6h} are summarized in Tab. 4.1, where the acoustic modes $A_{2u} + E_{1u}$ must be subtracted to get the optical modes.

Of the listed irreducible representations in Tab. 4.1, only the mode E_{2g} is Raman active, as can be seen from the corresponding character table in Sec. B. The fundamental result of this analysis is that in SRS only one mode with E_{2g} symmetry is observable for bulk $CePt_5$.

The E_{2g} mode has the basis function $(x^2 - y^2, xy)$ (see Sec. B). The corresponding Raman tensors can be obtained by the basis function as:

$$\mathcal{R}^1_{E_{2g}} = \begin{pmatrix} 0 & a & 0 \\ a & 0 & 0 \\ 0 & 0 & 0 \end{pmatrix}, \tag{4.5}$$

$$\mathcal{R}^2_{E_{2g}} = \begin{pmatrix} b & 0 & 0 \\ 0 & -b & 0 \\ 0 & 0 & 0 \end{pmatrix}. \tag{4.6}$$

The resulting Raman intensities can be determined by evaluating Eq. (2.21). Thus, this vibrational mode is observable in both polarization configurations $z(xx)\bar{z}$ and $z(xy)\bar{z}$.

The situation changes for the topmost layers of $CePt_5$/Pt(111). Due to the symmetry reduction at the surface, the number of vibrational modes rises. The occupied Wyckoff positions are also altered. The Ce atom is still on a $1a$ position, while the Pt atoms are now on $2b$ and $3c$ Wyckoff positions. The additional Pt atom in the topmost kagome layer also occupies a $1a$ position. The expected normal modes for the UC with reduced symmetry are given in Tab. 4.2, where the acoustic modes $A_1 + E_1$ must be subtracted to get the optical modes. The parity indices are left out since the point group C_{6v} possesses no inversion symmetry. Another significant change is that more modes become Raman active. However, of the Raman-active modes A_1, E_1, and E_2, only the modes with A_1 and E_2 symmetry can be observed in the used scattering geometry. The group theoretical analysis for the surface UC predicts two A_1 and two E_2 modes.

Table 4.2.: Vibrational modes and the linked Wyckoff positions for the point group C_{6v} of the surface UC. The optical modes A_1, E_1, and E_2 are Raman active. This table also contains the acoustic vibration modes $A_1 + E_1$.

	A_1	B_1	B_2	E_1	E_2
$3c$	1	1	1	2	1
$2b$	1	1		1	1
$1a$	1			1	

The mode with A_1 symmetry transforms according to the basis functions $x^2 + y^2$ and z^2 (see Sec. B). The Raman tensor for the A_1 mode is thus expressed as:

$$\mathcal{R}^1_{A_1} = \begin{pmatrix} a & 0 & 0 \\ 0 & a & 0 \\ 0 & 0 & b \end{pmatrix}. \tag{4.7}$$

The A_1 modes can only be observed in $z(xx)\bar{z}$ polarization configuration. The Raman tensors for the E_2 modes are identical to the ones of E_{2g} of the point group D_{6h} as given in Eqs. (4.5) and (4.6).

The group theoretical considerations regarding the vibrational modes of $CePt_5$ also apply for $LaPt_5$. Apart from slight mass differences, similar vibrational properties are therefore expected.

Relation of crystal-field and vibrational excitations

The considerations of the CF and vibrational excitations so far can be related to each other using group theory. For the point group D_{6h}, both the CF transitions in Eqs. (4.1) and (4.2) as well as the vibrational E_{2g} mode have the same basis function $(x^2 - y^2, xy)$. Hence, both features should be observed in the same polarization configurations $z(xx)\bar{z}$ and $z(xy)\bar{z}$ of the Raman spectra. This holds also for the counterparts of the point group C_{6v}.

Thereby, it is possible to relate the relevant irreducible representations with different notations and from different point groups according to:

$$\Gamma_6^+ \leftrightarrow E_{2g} \leftrightarrow \Gamma_6 \leftrightarrow E_2. \tag{4.8}$$

The information so far provides a good basis for the following interpretation of the Raman spectra of $CePt_5$/Pt(111) and $LaPt_5$/Pt(111).

4.3.2. Temperature dependence and comparison with $LaPt_5$/Pt(111)

The unpolarized Raman spectra of the $CePt_5$/Pt(111) sample with $t_{nom} = 18.0$ UC are shown in Fig. 4.4(a) for RT and LT. The comparison of the RT and LT spectra

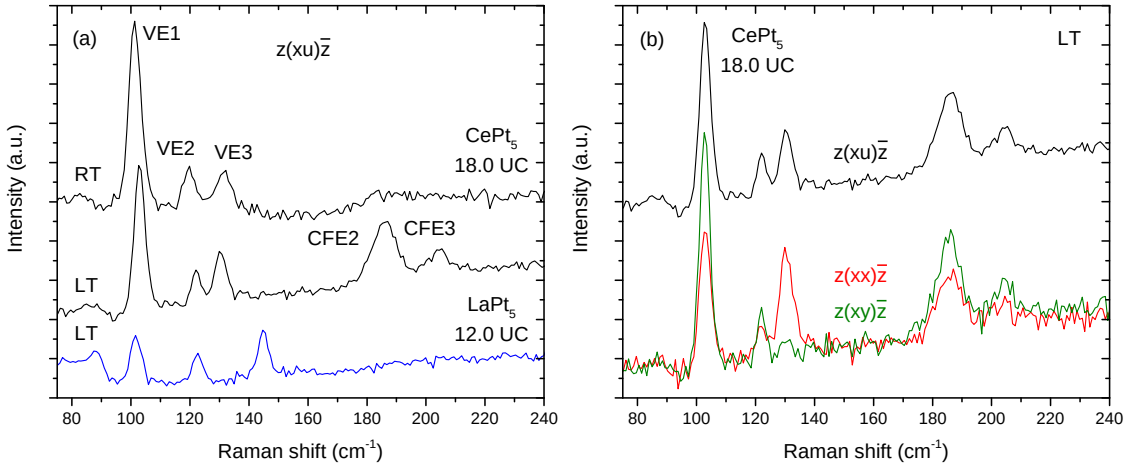

Figure 4.4.: Raman spectra of (a) $CePt_5$/Pt(111) (t_{nom} = 18.0 UC) at RT and LT as well as $LaPt_5$/Pt(111) (t_{nom} = 12.0 UC) at LT for reference and (b) the polarized spectra of $CePt_5$/Pt(111) (t_{nom} = 18.0 UC) at LT. The comparison of the Raman spectra in the left plot enables for $CePt_5$ the identification of the electronic Raman peaks CFE2 and CFE3 due to CFEs of the $4f$ electrons.

shows similarities but also huge differences. At a first glance, no vast changes are observed for the first three Raman peaks that appear in both spectra. They are located at 103.0, 122.0, and 130.4 cm^{-1} (at LT) and labeled with VE1 to VE3, respectively. The origin of these peaks is discussed later. In contrast, two further peaks at 185.8 and 204.8 cm^{-1} are observed at LT, but vanish almost completely at RT. Therefore, this second group of peaks seems to have a different origin than the first one. The clear appearance of these two peaks only at LT is a explicit indication for electronic excitations in Raman scattering (cf. Sec. 2.3.2). This assumption is further underscored by comparison with the Raman spectrum of $LaPt_5$/Pt(111) at LT, which is appended to Fig. 4.4(a). Since La hosts no $4f$ electron, no CFE peaks are expected. In accordance with that, in the approximate spectral region 180 – 200 cm^{-1} no Raman intensity is found for $LaPt_5$/Pt(111). These two Raman peaks of $CePt_5$/Pt(111) are thus attributed to CFEs and marked by CFE2 and CFE3 (motivation for the indexing will be provided further down).

In Fig. 4.4(b), additional Raman spectra for $CePt_5$/Pt(111) are shown for both polarization configurations $z(xx)\bar{z}$ and $z(xy)\bar{z}$. The unpolarized spectrum is identical with the LT Raman spectrum of Fig. 4.4(a). Focusing on the peaks CFE2 and CFE3, it is apparent that both peaks have the same polarization properties and are observed in both configurations. This can be assessed as an additional indication for a similar origin since both CFE Raman peaks are assigned to E_{2g} symmetry. Besides, polarization properties of other peaks and their connection, that can be

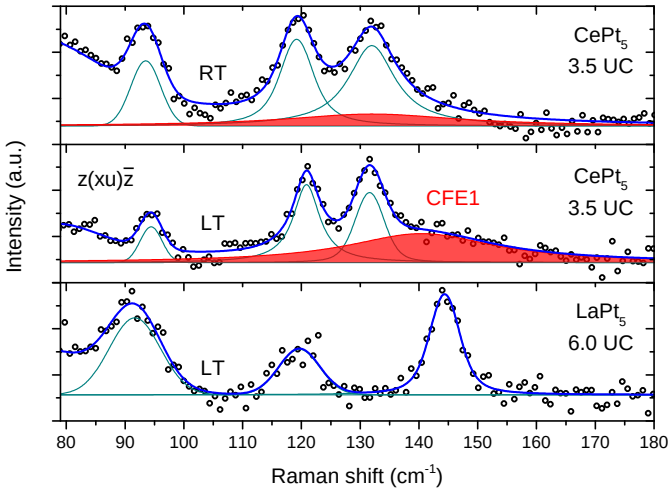

Figure 4.5.: Raman spectra of $CePt_5$/Pt(111) (t_{nom} = 3.5 UC) at RT and LT as well as $LaPt_5$/Pt(111) (t_{nom} = 6.0 UC) for LT. The spectra are fitted with Voigt profiles. The comparison of the Raman spectra enables the identification of a further electronic Raman peak CFE1.

extracted from Fig. 4.4(b), will be part of the considerations below.

The labels CFE2 and CFE3 suggest that there is another peak whose origin is a CFE. An appropriate Raman feature is observed for samples with the thinnest $CePt_5$ films. Therefore, the LT Raman spectrum for a $CePt_5$/Pt(111) sample with t_{nom} = 3.5 UC is shown in Fig. 4.5. For comparison, the corresponding Raman spectra for RT and for $LaPt_5$/Pt(111) (t_{nom} = 6.0 UC) are also depicted. To illustrate the composition of the spectra, Voigt profiles are fitted to the data points. The argumentation is the same as for the other CFE peaks. A Raman peak at 140.4 cm^{-1} in the LT spectrum, superimposed by the peaks VE2 and VE3, is nearly absent at RT and not observed at all in the spectrum of $LaPt_5$/Pt(111). This Raman peak is labeled CFE1. The polarization properties of the CFE1 peak could not extracted from the Raman spectra. At the left border of all shown plots, the intensity increases which is integrated into the fits.

The unambiguous identification of the CFE peaks can be further extended by a study of the thickness dependence. The series of LT Raman spectra of $CePt_5$/Pt(111) for several thicknesses as well as the bare Pt(111) substrate is accumulated in a waterfall plot in Fig. 4.6(a). Initially, the comparison of the spectrum of Pt(111) with the ones with $CePt_5$ films on top reveals that the observed peaks undoubtedly origin from the alloying of Pt with Ce. This is also true for the alloying with La. Furthermore, the intensity development with increasing film thickness t_{nom} can be tracked. The development of the CFE peaks will be subject of Sec. 4.4. Instead, the focus will be on the peaks VE1 to VE3 whose Raman intensity is dependent of the film thickness. The Raman intensity development is individually specific for

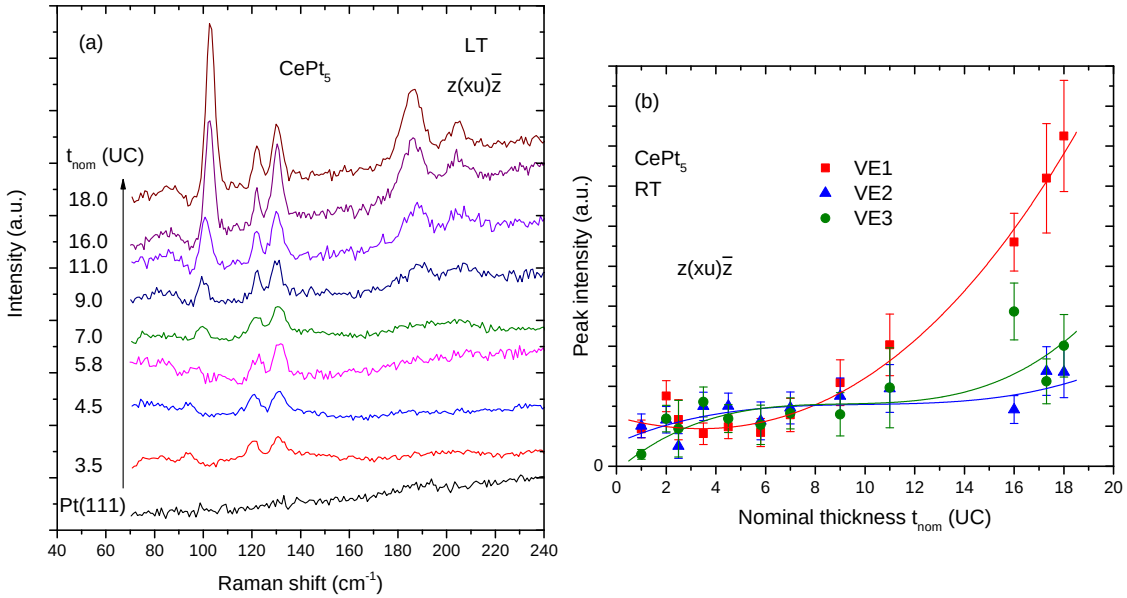

Figure 4.6.: Unpolarized Raman spectra of $CePt_5$/Pt(111): (a) waterfall plot for several thicknesses and the bare Pt(111) substrate for LT and (b) intensity development of the peak intensities of VE1 to VE3 in dependence of the nominal thickness t_{nom} at RT. Lines are meant as guides to the eyes. This development enables the identification of VE1 as the bulklike E_{2g} mode.

each vibrational peak as can be seen in Fig. 4.6(b) for RT. While the peaks VE2 and VE3 show nearly the same behavior, the peak VE1 gains much more spectral weight when the thickness is increased. This suggests a division into two groups with different origin. Since the amount of bulklike UCs contributing to the Raman signal raises with film thickness, it is obvious to attribute the peak VE1 to the only bulklike mode E_{2g} in $CePt_5$ (cf. Sec. 4.3.1). This assignment is further supported by considering the polarization properties. According to Fig. 4.4(b), the peak VE1 is observed in both polarization configurations $z(xx)\bar{z}$ and $z(xy)\bar{z}$, which perfectly matches with the group theoretical predictions for the E_{2g} mode. Hence, the E_{2g} vibrational mode is clearly identified with VE1. The properties of the peaks VE2 and VE3 are further discussed in Sec. 4.5.

For the completion of the identification of the CFE peaks, group theoretical arguments can be used again. As pointed out in Sec. 4.3.1, the CFE peaks and the VE1 peak of the bulk have the same irreducible representation and thus the same polarization properties. Both the strong peaks CFE2 and CFE3 as well as VE1 are observed in $z(xx)\bar{z}$ and $z(xy)\bar{z}$ and therefore both belong to the same irreducible representation (see Fig. 4.4(b)). Thereby, a consistent picture for the CFE peaks in

Table 4.3.: Peak frequencies (in cm^{-1}) of the vibrational modes and CFEs for $CePt_5$/Pt(111) and $LaPt_5$/Pt(111) obtained by SRS. The film thicknesses t_{nom} (in UC) are indicated for each frequency value. The corresponding spectra are shown in Figs. 4.4(a) and 4.5.

	$CePt_5$/Pt(111)			$LaPt_5$/Pt(111)	
	RT	LT	t_{nom}	LT	t_{nom}
VE1	101.3	103.0	18.0	101.6	12.0
VE2	119.7	122.0	18.0	122.6	12.0
VE3	131.4	130.4	18.0	144.9	12.0
CFE1		140.4	3.5		
CFE2		185.8	18.0		
CFE3		204.8	18.0		

the Raman spectra exists.

Hence, there are three peaks related to CFEs in $CePt_5$/Pt(111): CFE1, CFE2, and CFE3. Further properties of these peaks are discussed in Sec. 4.4. Consequently, the other peaks (VE1, VE2, and VE3) are due to vibrational excitations and are examined for $CePt_5$/Pt(111) and $LaPt_5$/Pt(111) in Sec. 4.5. The relevant peaks of the Raman spectra shown so far are all compiled in Tab. 4.3. Apart from the Raman peaks found so far for $CePt_5$/Pt(111), no further spectral features were found in the spectral range up to $\approx 1450\,cm^{-1}$. This also applies for the higher spectral range of $LaPt_5$/Pt(111).

4.4. Properties of the crystal-field excitations in $CePt_5$/Pt(111)

The origin and properties of the CFE peaks of $CePt_5$/Pt(111), which were identified in the previous section, will be subject in the following.

So far, both possible CFE transitions $\pm\frac{1}{2} \leftrightarrow \mp\frac{3}{2}$ and $\pm\frac{1}{2} \leftrightarrow \pm\frac{5}{2}$ can be attributed to the three observed CFE Raman peaks. This question cannot be solved by SRS alone and thus requires further information. With the help of XAS results, where the energetic configuration of the involved CF states was reported [219,242], the SRS data can be further evaluated. The Kramers doublets with $M_J = \pm\frac{1}{2}$ and $M_J = \pm\frac{3}{2}$ are only separated by an energy of less than $8\,cm^{-1}$, while the states with $M_J = \pm\frac{5}{2}$ have the highest energy. This is schematically indicated in Fig. 4.3. The transition $\pm\frac{1}{2} \leftrightarrow \mp\frac{3}{2}$ can therefore be ruled out as origin for the CFE Raman peaks, leaving only $\pm\frac{1}{2} \leftrightarrow \pm\frac{5}{2}$ ($\Gamma_7^- \leftrightarrow \Gamma_8^-$) as possible transition.

The examination of the development of the CFE peaks with the film thickness

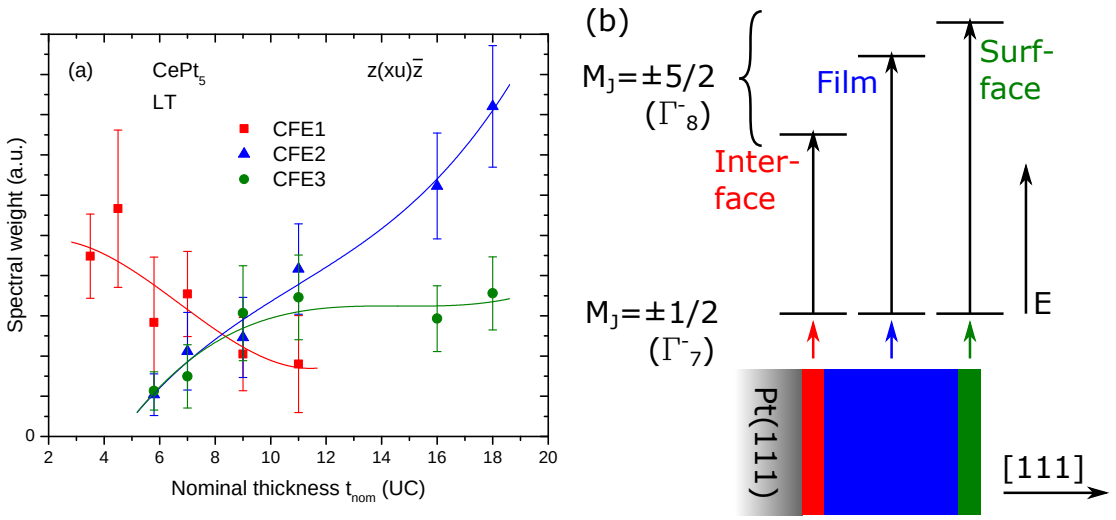

Figure 4.7.: Depiction of (a) the development of the spectral weight of the CFE peaks with t_{nom} in $CePt_5$/Pt(111) at LT and (b) schematic illustration of the attribution of the observed CFE peaks to their regions of origin for a $CePt_5$/Pt(111) sample. Lines are meant as guides to the eyes.

t_{nom} reveals further insights. For this purpose, the spectral weight of the CFE peaks in the unpolarized LT spectra of $CePt_5$/Pt(111) is plotted in Fig. 4.7(a). The intensity of the peak CFE1 decreases with increasing film thickness. For ≈12 UC and thicker samples, the intensity becomes too weak to be recognized which leads to the estimation of an attenuation length of (6.0 ± 1.5) nm. In contrast, at thicknesses below ≈5 UC the peaks CFE2 and CFE3 are not observed, but gain weight with increasing thickness. However, their high-thickness behavior is different. While the CFE3 peak only slightly increases with film thickness, the intensity of CFE2 is increasing much faster.

The thickness development of all three CFE peaks can be consistently explained by attribution of each peak to regions of different depths below the surface. The distribution of neighboring Pt atoms around a Ce atom will influence the CF and therefore alter the CFE as observed by SRS. In that sense, the CFE1 feature is assigned to the interface between the $CePt_5$ film and the Pt(111) substrate. It vanishes when the film thickness exceeds the penetration depth of the laser light. In turn, the CFE3 peak is allocated to the topmost layers of the $CePt_5$ film. Since the film has always a surface region, the slowly varying intensity accounts for that. The CFE2 peak is related to the inner, bulklike part of the film. Therefore, its Raman intensity increases with growing volume of the film. This attribution is schematically depicted in Fig. 4.7(b).

The question whether the polarization properties of the CFE peaks, i.e., CFE2 and CFE3, should change in dependence of their region of origin can be addressed by the group theoretical considerations of Sec. 4.3.1. It is mentioned there that the irreducible representations Γ_6^- of the bulk and Γ_6 of the surface have equal basis functions. So, the CF is altered but leaves the polarization properties unchanged. This is perfectly in line with the fact that CFE2 and CFE3 are observed in $z(xx)\bar{z}$ and $z(xy)\bar{z}$ polarization configuration in Fig. 4.4(b). This consideration might also be true for the interface region, i.e., CFE1, but cannot be verified in the Raman spectra due to its weak intensity.

The results so far can be directly compared to the CF scheme predicted by XLD and XMCD measurements [242]. Since the probing depth of XAS is smaller than that of SRS (reduction by a factor of 4 – 6), it is reasonable to compare the peaks of CFE2 and CFE3 as obtained by SRS with the samples with thicker films. For the thinner samples a comparison with CFE1 might be more appropriate. In the XLD and XMCD measurements, the states with $M_J = \pm\frac{5}{2}$ are observed to be separated from the other two Kramers doublets by $\gtrsim$200 cm^{-1} for $t_{\mathrm{nom}} \gtrsim 7$ UC. This is in the same range as the frequency of 185.8 cm^{-1} of the bulklike peak CFE2 and matches excellent with the frequency of 204.8 cm^{-1} of near-surface peak CFE3, which is assumed to match better with the x-ray data. For films with $t_{\mathrm{nom}} \lesssim 4$ UC, the splitting measured by XLD and XMCD reduces to $\lesssim$145 cm^{-1}. Compared to the near-interface peak CFE1 at a frequency of 140.4 cm^{-1}, the agreement is very good. Hence, the overall resemblance of both techniques is quite gratifying.

Regarding the FWHMs of the CFE Raman peaks, the question rises for which reason the peak CFE1 is much broader compared to the other peaks CFE2 and CFE3. This observation can be related to INS observations for bulk Ce-containing materials. There, a correlation was found between the width of the CFEs in INS and the hybridization strength between $4f$ electrons of Ce and itinerant electrons as found by XAS [250]. This indicates that hybridization leads to a reduced lifetime of the CFE states. The Raman results are fully compatible with these findings since the broad CFE1 peak is observed to be most intense for small film thicknesses where also the hybridization of the $4f$ electrons is strongest [241].

4.5. Vibrational excitations in $CePt_5$/Pt(111) and $LaPt_5$/Pt(111)

After the inspection of the CFE peaks, the vibrational peaks of $CePt_5$/Pt(111) and $LaPt_5$/Pt(111) will be discussed here as last part for understanding of the Raman spectra.

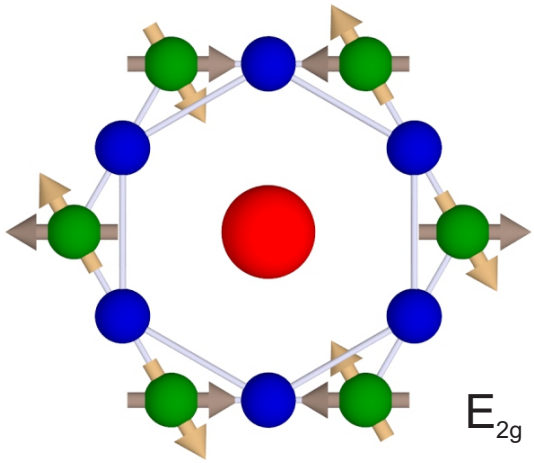

Figure 4.8.: Top view (in [111] direction) of the vibrational eigenmode E_{2g} of the $CePt_5$ UC with D_{6h} symmetry. This mode is twofold degenerate as indicated by the two differently colored groups of arrows.

4.5.1. Properties of the vibrational excitations

In addition to the investigations of the vibrational peaks above, i.e., the identification of the VE1 as bulklike E_{2g} mode, further considerations on $CePt_5$/Pt(111) including their origin is required. $LaPt_5$/Pt(111) will be also in the focus of this section.

Vibrational peaks of $CePt_5$/Pt(111)

In Sec. 4.3, the VE1 peak in Fig. 4.4(a) is identified by its intensity development with film thickness as E_{2g} vibrational mode and some properties are already mentioned, i.e., that it is the only Raman-active mode of the bulk $CePt_5$ UC. A further remarkable circumstance is the nonsaturating intensity for thick films as found in Fig. 4.6(b). This might be related to an increasing Raman scattering efficiency with increasing film thickness, which is possibly linked to gradual formation of bulklike symmetry. The resulting electronic scattering becomes also stronger if there is considerable coupling to the vibrational mode. This interaction was already observed and described in Refs. [227,251,252].

To gain further insights into the properties of VE1, the vibrational pattern can be determined by evaluation of Eq. (2.15). The resulting eigenvectors are depicted in Fig. 4.8. Only Pt atoms from the $CePt_2$ layer are displaced perpendicular to the [111] direction. This is in line with the group theoretical prediction that the E_{2g} mode originates from Pt atoms at the Wyckoff position 2*c* (see Tab. 4.1). As E-like mode, it is twofold degenerate as indicated by the differently colored arrows. Moreover, the displacement pattern of the mode preserves the inversion symmetry.

Yet, there are two further vibrational modes VE2 and VE3 in Fig. 4.4(a) whose existence cannot be explained by group theoretical analysis of bulk $CePt_5$ (cf.

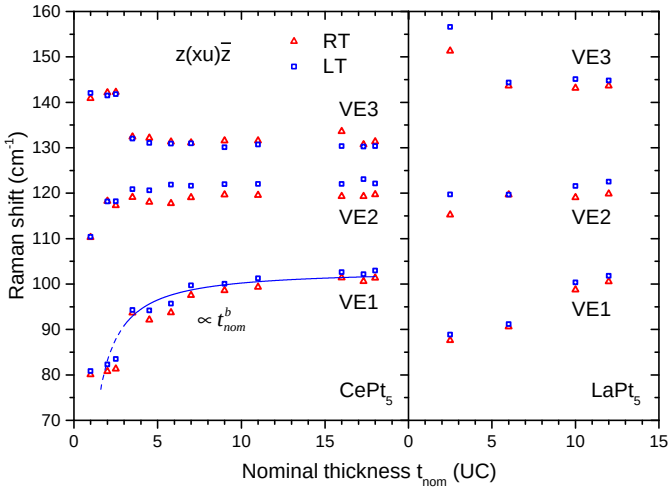

Figure 4.9.: Development of the Raman shift of the vibrational peaks of $CePt_5$/Pt(111) and $LaPt_5$/Pt(111) with the film thickness t_{nom}. Both temperatures RT and LT are shown. For details on the model fit see text.

Tab. 4.1). As mentioned in Sec. 4.3.1, the symmetry reduction at the surface allows the emergence of additional modes. With the aid of Tab. 4.2, these new modes find a natural explanation. The mode VE2 is observed in both polarization configurations, while the mode VE3 is only observed in $z(xx)\bar{z}$ configuration (see Fig. 4.4(b)). These properties can be directly linked to the representations E_2 and A_1 of C_{6v}, respectively. One of the two E_2 modes of the symmetry-reduced UC from the surface has the same vibrational pattern as depicted in Fig. 4.8. The eigenvectors of the second E_2 mode as well as the modes with other symmetries are more complicated and involve the displacement of additional atoms. For instance, A_1 modes are composed of atomic movements along the [111] direction. However, four new optical Raman modes are predicted by Tab. 4.2 (excluding acoustic modes), but not all are observed. Maybe the two missing modes are spectrally located below the filter edge or their Raman efficiency is too weak to be observed. For Bi_2Se_3, a similar situation of new appearing phonons due to surface symmetry reduction was observed by RS as well [253].

The frequency development in dependence of the film thickness t_{nom} of the three vibrational eigenmodes exhibits a comprehensive picture. The data for RT and LT are compiled in Fig. 4.9. The frequency of the VE1 phonon mode of $CePt_5$/Pt(111) decreases for low thicknesses, but saturates for samples with $t_{\mathrm{nom}} \gtrsim 10\,\mathrm{UC}$. The peak frequency of VE1 at $t_{\mathrm{nom}} = 18.0\,\mathrm{UC}$ can therefore be truly seen as bulk value for $CePt_5$/Pt(111). The frequency development is also apparent in Fig. 4.6(a). The considered film thicknesses are small enough to alter phonon frequencies due to confinement [214]. Therefore, the LT data are fitted by a power law of the form

[254]:

$$\Delta\omega \propto t_{\mathrm{nom}}^{b}, \tag{4.9}$$

where $\Delta\omega$ is the thickness-induced frequency shift and b is a fitting parameter. Only data points above 3 UC are considered in the fit, but the extension (dashed curve) of the curve to smaller thicknesses is satisfactory. The frequency shift is well described by Eq. (4.9) and suggests therefore phonon confinement as reason for the observed shift of peak VE1. It should be mentioned that strain, which is also present in the films, can similarly shift the peak frequency of phonons [49]. In contrast, the deviations for the peaks VE2 and VE3 from the values for thicker films are less pronounced. This is in line with the attribution of peak VE1 to the bulk and the other peaks to the surface region. Quantitatively, from highest to lowest film thicknesses the frequencies at LT varies by −21.5, −9.6, and 8.9 % for the peaks VE1 to VE3, respectively. It is therefore plausible to relate the development of the near-surface peaks VE2 and VE3 to the evolution of the surface lattice parameter as observed in Ref. [241]. Note that the peaks VE2 and VE3 shift in opposite directions and will be revisited in combination with $LaPt_5$.

Interestingly, all three peak frequency shifts exhibit a step-like feature around $t_{\mathrm{nom}} \approx 3$ UC. This observation is especially pronounced for VE1 and VE3 and, with decreasing thickness, results in a down-ward step and an up-ward step of $\approx 10\,\mathrm{cm}^{-1}$, respectively. For samples with around 3 UC, it is known by a LEED analysis that for this film thicknesses the surface lattice constant changes vastly [241]. This will of course affect the eigenfrequencies of the modes and is likely the reason for the observed steps. Moreover, the steps seem to continue the trend of the previous curve.

Vibrational peaks of $LaPt_5$/Pt(111)

So far, the Raman spectra of $LaPt_5$/Pt(111) are only considered as references for interpretation of the Raman spectra of $CePt_5$/Pt(111). Now, the spectra will be discussed in more detail. First of all it should be noted that the Raman spectra of $LaPt_5$/Pt(111) and $CePt_5$/Pt(111) are closely related, apart from the CFE peaks (see Fig. 4.4(a)). Since both materials crystallize in the same structure, it is plausible that the three vibrational peaks share the same origin. This assumption is fortified by considering the polarization properties as shown for $LaPt_5$/Pt(111) in Fig. 4.10. The peak VE1 of $LaPt_5$ has E_{2g} symmetry, while the peaks VE2 and VE3 have E_2 and A_1 symmetry, respectively. This matches perfectly with the peak polarizations of $CePt_5$ (cf. Fig. 4.4(b)). The vibrational mode pattern depicted in Fig. 4.8 can also be transferred to the E_{2g} mode of $LaPt_5$/Pt(111).

For a systematic evaluation of the vibrational peaks, the peak frequencies are appended to Fig. 4.9. The studied thickness range is less than that of $CePt_5$/Pt(111). For this reason, a saturation for the frequencies at high thicknesses is not apparent. Nevertheless, a similar behavior like for $CePt_5$/Pt(111) is observed. Similar are also

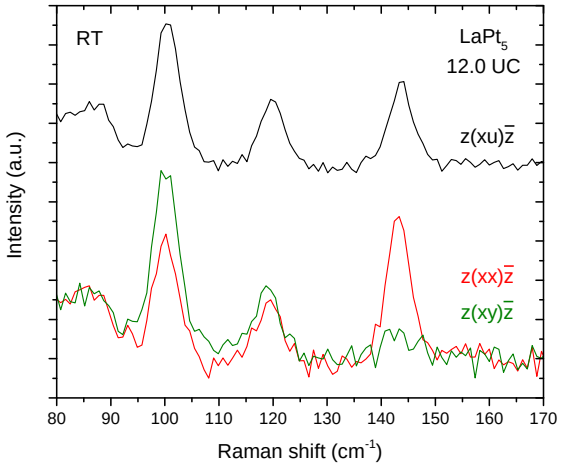

Figure 4.10.: Raman spectra of $LaPt_5$/Pt(111) ($t_{\mathrm{nom}} = 12.0\,\mathrm{UC}$) at RT. The unpolarized spectrum as well as the spectra for the polarization configurations $z(xx)\bar{z}$ and $z(xy)\bar{z}$ are shown.

the tendencies of VE1 to shift downward and VE3 to shift upward with decreasing thickness, while the VE2 deviates only slightly downwards. A qualitative evaluation as for $CePt_5$/Pt(111) yields shifts at LT of -12.7, -2.3, and $8.1\,\%$ for the peaks VE1 to VE3, respectively. For simplicity, the peak frequencies for the samples with the highest thicknesses are assumed to be saturated.

When comparing $LaPt_5$/Pt(111) and $CePt_5$/Pt(111), the peak frequencies for VE1 and VE2 are quite similar for the thickest samples. This is not surprising since the relative atomic mass difference between Ce and La atoms is only $\approx 0.7\,\%$. The in-plane lattice constant of $LaPt_5$ is only slightly larger than that of $CePt_5$ due to the lanthanide contraction [255], but they differ in total only in the percentage range [247]. Based on Eq. (3.8), the similar frequency values are reasonable since the mass increase and UC-volume reduction cancel partly out. Moreover, the displacement pattern of Fig. 4.8 suggests that for VE1 the rare-earth ion only influences the phonon frequency to a small extent. However, the peak VE3 does not fit into this picture. The frequency of this mode of $LaPt_5$ is approximately $15\,\mathrm{cm}^{-1}$ higher than the corresponding one of $CePt_5$ and also increases with decreasing film thickness. Since for both surface systems the peak frequencies of VE1 and VE2 show opposite thickness dependence to VE3, the $4f$ electrons as cause can be excluded. It seems rather likely that the symmetry of the modes (VE1 and VE2 are E-like modes, VE3 is an A-like mode) is responsible for the direction of the shifts.

With regard to the different surface systems and its response to temperature changes, the peak VE3 hosts another curiosity. For $LaPt_5$/Pt(111), the peak frequencies increase when the sample temperature is lowered to LT as it usually does. However, another explanation must therefore apply for the Raman peak VE3 of $CePt_5$/Pt(111).

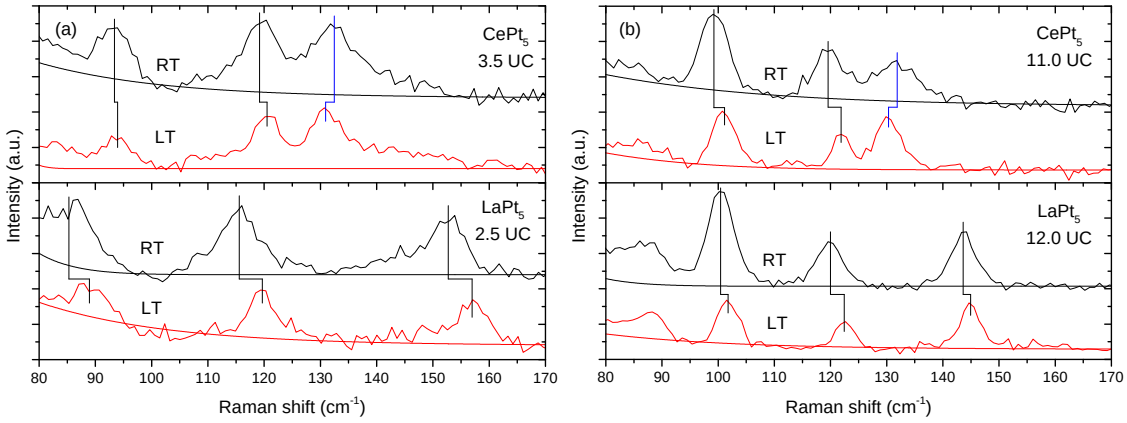

Figure 4.11.: Raman spectra of $CePt_5$/Pt(111) and $LaPt_5$/Pt(111) for RT and LT for (a) thinner films ($t_{\mathrm{nom}} = 3.5\,\mathrm{UC}$ for $CePt_5$/Pt(111) and $t_{\mathrm{nom}} = 2.5\,\mathrm{UC}$ for $LaPt_5$/Pt(111)) and (b) for thicker films ($t_{\mathrm{nom}} = 11.0\,\mathrm{UC}$ for $CePt_5$/Pt(111) and $t_{\mathrm{nom}} = 12.0\,\mathrm{UC}$ for $LaPt_5$/Pt(111)). The polarization configuration of all spectra is $z(xu)\bar{z}$. The anomalous temperature shift is indicated by blue vertical lines. The horizontal curves mark the assumed background.

4.5.2. Anomalous temperature-induced frequency shifts

The obscure temperature behavior of peak VE3 of $CePt_5$/Pt(111) found in the previous section is further studied. For that reason, temperature-dependent Raman spectra are compiled for $CePt_5$/Pt(111) and $LaPt_5$/Pt(111) in Fig. 4.11. The unusual property of the peak VE3 of $CePt_5$/Pt(111) becomes apparent: VE3 is shifted anomalously with temperature. This is already observable when Figs. 4.4(a) and 4.9 are closely inspected. Note that this is not a thickness-dependent phenomenon, since it is observed for both the sample with 3.5 and 11.0 UC. Note the weak features below $\approx 90\,\mathrm{cm}^{-1}$, especially for $LaPt_5$/Pt(111) in Fig. 4.11(b), which are omitted in the analysis since they might be artifacts due to rising intensity in combination with the transmission characteristics of the edge filter (see Sec. G). For the peaks VE1 and VE2 of $CePt_5$/Pt(111), the common temperature shift due to anharmonicity is observed. Since the anomalous temperature shift is not observed for $LaPt_5$/Pt(111), there is the strong suspicion that $4f$ electrons are involved.

Due to electron-phonon coupling the phonon mode VE3 might be influenced by the $4f$ electrons. Conduction electrons may be also come into play since ($5d$,$4f$) hybridization and hence Kondo screening occurs when the sample is cooled below T_{K} [240]. These mechanisms would then lead to the observed phonon softening. Since only one phonon mode is affected which besides is the sole one with A_1 symmetry, symmetry might be relevant and inhibit the electron-phonon coupling with other

modes. Phonon softening was also previously discussed for the Ce-containing material $CeAl_2$ [256,257].

4.6. Conclusion

In the presented Raman data distinct peaks were observed for thin intermetallic films of $CePt_5$ and $LaPt_5$ on Pt(111) substrate. This is remarkable, since the conduction electrons of metals are generally believed to cause a broad background possibly obscuring other Raman peaks. Moreover, the penetration depth of light, and therefore the information depth, is greatly reduced in metals (compared to, e.g., Si).

In the Raman spectra, two kinds of Raman peaks of different origin could be distinguished. The Raman peaks due to CFEs could be unambiguously determined and all related to the same transition between CF states but from different film regions. Hence, there are three CFE Raman peaks which originate from the surface, the bulklike region of the film, and the interface to the substrate. Apart from that, three vibrational Raman peaks are observed of which one is attributed to the bulk region while the other two originate from the surface. This determination, which allows a more direct evaluation than from XLD and XMCD measurements, enables the reinsertion of the CF splitting parameters into the model fits of the susceptibility and therefore a reevaluation of the Kondo physics. Apart from that, the SRS data support the existing fits.

Group theoretical considerations are shown to be very useful for the interpretation of the Raman spectra. This holds not only for the number and polarization properties of vibrational Raman peaks, but also for CFE peaks. Moreover, the polarization configurations of Raman features of both origins can be related to each other. Through symmetry reduction at the surface, properties of emerging vibrational modes can be predicted. The determination of eigenvectors of vibrational modes is another merit of group theory.

5. Summary and outlook

The present thesis deals with the investigation of elementary excitations of surface systems by surface Raman spectroscopy (SRS). Low-dimensional surface systems are subject of current extensive research interest since they exhibit new physical phenomena with respect to bulk materials. The microscopically ordered surface morphology alters the electronic and vibrational properties as well as their interaction in a distinct way. Moreover, through confinement to two-dimensional (2D) and one-dimensional (1D) extensions, electronic correlations become more relevant. These and related effects are expected to have a considerable impact on the analyzed surface systems.

All analyzed surface systems - ordered metal adsorbates on semiconductor substrates and thin intermetallic films - show specific and unique Raman peaks that are related to excitations of vibrational or electronic nature. Hence, SRS lends itself as a versatile optical probe for surfaces and near-surface regions. Since scattering from atomic arrangements as thin as a monolayer (ML) is detectable, the very high sensitivity of the experimental setup is evident. In addition to the spectroscopic advantages and the contactless operation mode of Raman spectroscopy (RS), the Raman spectra contain and reveal much information about physical phenomena in the samples. Insights are obtained by comparison between spectra of reconstructed and unreconstructed surfaces as well as material systems where specific atoms are substituted. Additional information about the Raman peaks is extracted from their temperature dependence and their polarization configurations in combination with group theoretical considerations. Moreover, cumulative fits of single Voigt profiles of the Raman data allow an excellent spectral peak determination accuracy of $\approx 0.1\,\mathrm{cm}^{-1}$. To ensure a high sample quality and reproducible conditions, great experimental effort is spent on the optical and ultrahigh vacuum (UHV) setups. All prepared sample surfaces are checked by low-energy electron diffraction (LEED) prior to the Raman measurements.

The Raman data of all systems are combined and compared with theoretical and other experimental results as far as available. Special emphasis lies on exclusive first-principles calculations of vibrational Raman spectra for different structural models. This enables the choice of preferred models for the structural description, even if the atomic surface configurations of the models are quite alike. With experimental respect, the surface Raman data are compared with results of complementary methods, like, e.g., helium atom scattering (HAS) and high-resolution electron energy loss spectroscopy (HREELS), and to other surface Raman spectra obtained

separately in a different setup. A benefit of SRS, in relation to other surface-sensitive techniques, is its high spectral resolution and sensitivity which allows the observation of new features as well as the refinement of existing ones. For the particular surface systems, all results fit generally with good agreement into a consistent picture.

In the following two parts, the key results of the Raman investigation for both types of investigated surface systems are comprehensively summarized. This chapter is concluded by an outlook.

Summary - Surface adsorbate systems

A major part of this thesis covers several surface reconstructions of Au adatoms on Si(111) substrate as well as Sn adatoms on Ge(111) and Si(111) substrates. The surface reconstructions are obtained by self-assembly of the adsorbed atoms in special preparation procedures.

The Au-induced reconstructions Au-(5×2)/Si(111) and Au-($\sqrt{3}\times\sqrt{3}$)/Si(111) are of special interest. The Au adatoms on the Si(111) surface form quasi-1D chain-like structures and 2D triangular patterns, respectively. For the Au-(5×2)/Si(111) reconstruction, many distinct surface phonons are identified and analyzed for their polarization configuration. However, there exist several possible models for the exact atomic configuration of this reconstruction. With the aid of the SRS results in combination with first-principles calculations, a preferred model is chosen for this surface reconstruction. On this basis, the Raman data are compared to calculated spectra for the Erwin-Barke-Himpsel (EBH) and Kwon-Kang (KK) model, which are the two most promising ones. As a result, the KK structural model is favored for the description of the Au-(5×2)/Si(111) surface. Moreover, from the calculations atomic displacement patterns for atoms can be deduced. A similar approach is conducted for the Au-($\sqrt{3}\times\sqrt{3}$)/Si(111) surface. The observed features in the surface Raman spectra are clearly reconstruction-dependent and allow therefore a discrimination. The Raman spectra, decomposed by fitting, are compared to calculated spectra for different structural models. Thus for the proposed twisted-trimer (TT) and conjugate honeycomb-chained-trimer (CHCT) model, a choice toward the CHCT model for Au-($\sqrt{3}\times\sqrt{3}$)/Si(111) is made. The calculations further reveal the localization of the surface modes to be at the Au adatoms, the Si substrate or a mixture of both. For both Au reconstructions, the analysis is enriched by discussing group theoretical considerations and the effect of temperature. The method of combining SRS and first-principles calculation results is therefore a promising tool for structural exploration of surfaces.

For a Sn coverage of $\frac{1}{3}$ ML on Ge(111) and Si(111), a triangular surface pattern is formed on both substrates. Although these systems are closely related and similar, they exhibit distinctive deviations concerning their low temperature (LT, $T \approx 20-40\,\mathrm{K}$) behavior. For Sn/Ge(111), a reversible structural phase transition (SPT) between two reconstructions occurs upon cooling: ($\sqrt{3}\times\sqrt{3}$) ↔ (3×3). In contrast,

no SPT is observed for the Sn/Si(111) system. The dynamical fluctuation (DF) model is capable of explaining this transition for Sn/Ge(111), while some aspects also apply for Sn/Si(111). This model claims that one of three Sn atoms protrudes the other two. The adatoms with different height positions exchange and freeze, dependent on the actual system, into a long-range order upon cooling, which triggers the phase transition. Theoretically, there are three eigenmodes describing the Sn adatom movement. For Sn/Ge(111) and Sn/Si(111), one DF mode is observed at 55.8 and 88.3 cm^{-1} at LT, respectively. The high-resolution Raman spectra reveal that the DF mode of Sn/Ge(111) is not shifted with temperature, while it is as usually shifted for Sn/Si(111). Therefore, the mode of Sn/Ge(111) exhibits nearly completely harmonic character which is in line with theoretical predictions. These findings confirm the assumed model and reveal both surface systems to be alike at room temperature (RT, $T \approx 300\,\mathrm{K}$). Furthermore, a low-frequency shoulder of the DF mode of Sn/Ge(111), centered at $\approx 50\,\mathrm{cm}^{-1}$, indicates the SPT and is ascribed to the induced backfolding of a Rayleigh wave (RW) by transition to the (3×3) periodicity. The intensity development of this RW shoulder yields a transition temperature of 225 K, which is in excellent agreement with other experimental results. This phase transition is furthermore stated to be of order-disorder type. The high-frequency Raman spectra ($\gtrsim 80\,\mathrm{cm}^{-1}$ for Sn/Ge(111) and $\gtrsim 130\,\mathrm{cm}^{-1}$ for Sn/Si(111)) exhibit a large variety of further surface phonon modes. No sign for SPTs are observed in that spectral ranges. The existing HAS data for Sn/Ge(111) are supported by the better resolved SRS data. Moreover, the higher frequency ranges as well as the SRS results for Sn/Si(111) are observed for the first time.

For higher coverages of Sn on Si(111), the Sn-$(2\sqrt{3}\times 2\sqrt{3})$/Si(111) reconstruction is formed. The Raman spectra of the Sn-$(2\sqrt{3}\times 2\sqrt{3})$/Si(111) surface are readily distinguishable from the reconstruction with lower Sn coverage. The observed vibration modes are located below $\approx 180\,\mathrm{cm}^{-1}$ and exhibit distinct polarization behavior. A structurally related system is found in thin films of α-Sn. The main peak of α-Sn, i.e., the longitudinal optic (LO) phonon for a (001) surface, is observed at $200.0\,\mathrm{cm}^{-1}$ at 77 K and is likely to be related to a surface phonon observed for Sn-$(\sqrt{3}\times\sqrt{3})$/Si(111). Furthermore, the Raman spectra allow the exclusion of β-Sn formation as well as the confirmation of good crystalline quality of the α-Sn film.

Vibrational eigenmodes of universal character which appear for the different adatom species and reconstructions on Si(111) are identified and are believed to be mainly located at the substrate. These cross-references are a good evidence for the reliability of SRS.

Apart from the reconstructions generated by different atomic species on the substrate surfaces, the clean semiconductor surfaces Si(111)-(7×7) and Ge(111)-c(2×8) are also part of the investigation. They are not only a reference for the induced changes by adatom deposition but also of interest on its own. The Raman spectra of the Si(111)-(7×7) reconstruction for LT are well in line with previous SRS

results for higher temperatures. However, additional Raman peaks are observed at LT. The Raman data for the Ge(111)-c(2×8) reconstruction exhibit many new reconstruction-induced spectral features. The Raman spectra are therefore compared with theoretical calculations and HAS measurements. Some Raman peaks are attributed to backfolded RWs and to optical phonons. Furthermore, on basis of the calculations for most experimentally observed modes a determination is feasible whether it is localized mainly at the Ge adatoms or restatoms. However, SRS reveals more modes of the Ge(111)-c(2×8) surface than expected from calculations and other experimental methods. Therefore, the Raman data represent the most complete set of vibrational modes.

Summary - Surface intermetallic systems

Another part of this thesis treats ultrathin films of $CePt_5$ and $LaPt_5$ on Pt(111) substrate. The film thicknesses of both systems are in the range of several unit cells (UCs) down to only a single UC. The major difference between both compounds is the $4f$ electron of Ce in $CePt_5$, which is absent when La is substituted with Ce. Therefore, $CePt_5$/Pt(111) can be compared to $LaPt_5$/Pt(111) which serves as a reference system with the same crystal symmetry but different electronic properties. The energy levels of the $4f$ electrons in $CePt_5$ are altered by the crystal field (CF) which results in a lifting of their degeneracy. Transitions between the CF states can be examined by SRS as crystal-field excitations (CFEs) in the Raman spectra. The knowledge of the CF scheme is essential for a correct description of Kondo physics. Further attention is turned to the vibrational properties of both systems.

Signatures in the Raman spectra of $CePt_5$/Pt(111) are unambiguously identified as transitions between the CF states of the $4f$ electrons. The assignment is based on several criteria, including the comparison to $LaPt_5$/Pt(111) and group theoretical considerations. The three observed CFE Raman peaks can be attributed to the same transition between two Kramers doublets: $\pm\frac{1}{2} \leftrightarrow \pm\frac{5}{2}$. Though, they originate from different depth regions of the films. An attribution is feasible by examination of the thickness dependence of the individual peak intensities. Hence, CFE Raman peaks from the surface, the bulklike part of the intermetallic film, and the interface to the substrate are observed at 140.4, 185.8, and 204.8 cm^{-1} (17.4, 23.0, and 25.4 meV), respectively. The polarization properties are in line with selection rules for electronic Raman scattering. These Raman results further support the data obtained by x-ray linear dichroism (XLD) and x-ray magnetic circular dichroism (XMCD).

From group theoretical analysis it is known that both bulk $CePt_5$ and $LaPt_5$ have only one Raman-active phonon, which is identified by the intensity development in the Raman spectra. Moreover, this observed vibrational Raman peak is related to the CFE Raman peaks by group theory. Among many other examples, this is a further proof of the extraordinary usefulness of group theory in RS. Additional vibrational Raman peaks appear in the spectra due to symmetry reduction at the

surface. Their existences and polarization properties are compatible with group theoretical predictions. Apart from the electronic Raman peaks, the spectra of $CePt_5$/Pt(111) and $LaPt_5$/Pt(111) are very similar and exhibit the same number of modes. However, for one phonon mode of $CePt_5$/Pt(111) an unusual temperature shift is observed. Since this behavior is absent for $LaPt_5$/Pt(111), this effect is evidently related to an interaction with the $4f$ electrons.

Outlook

Finally, possible ways to extend this research on the surface systems by SRS are pointed out as an outlook.

For the Sn/Ge(111) and Sn/Si(111) surfaces, new insights are expected from the comparison of the SRS data with further *ab initio* calculations, especially for the vibrational modes at higher frequencies. Also, the different temperature behavior of the DF modes of both systems could be addressed. Moreover, SRS seems to be a promising experimental technique to illuminate the controversy about the appearance of a second $(\sqrt{3} \times \sqrt{3})$ reconstruction for Sn/Ge(111) for temperatures below 30 K. If the $(\sqrt{3} \times \sqrt{3})$ phase is restored, the low-frequency shoulder of the DF mode should disappear as backfolding is lifted.

For the CFEs in $CePt_5$/Pt(111), a further investigation of their temperature behavior can be obtained by additional acquirement of anti-Stokes Raman spectra. Since the electron states are not populated according to the Bose-Einstein statistics, the intensity ratio between Stokes and anti-Stokes spectra is different than expected for phonons.

Due to the many positive examples for various surface systems presented in this thesis, SRS especially in combination with theoretical predictions is an experimental method with good prospects for the investigation of future surface systems. Many fields of surface physics are thereby accessible.

Appendix

A. Compilation of relevant symmetry groups

Symmetry groups that are relevant for this thesis are tabulated together with the applying surface systems. The 3D symmetry groups are listed in Schoenflies and Hermann-Mauguin (or international) notation [43,44,69,70]. The surface system Ge(111)-c(2×8) has no surface symmetry and is therefore omitted.

Table A.1.: Point and space groups are listed for 3D and if relevant for 2D together with the applying material systems.

Point group		Space group		Material systems
3D	2D	3D	2D	
C_s, m	$1m$	C_s^2, Pb	$p1g1$	Au-(5×2)/Si(111)
		C_s^3, Bm	$c1m1$	Sn-$(2\sqrt{3} \times 2\sqrt{3})$/Si(111)
C_{3v}, $3m$	$3m$	C_{3v}^1, $P3m1$	$p3m1$	Si(111)-(7×7), (3×3) rec. of Sn/Ge(111) and Sn/Si(111)
		C_{3v}^2, $P31m$	$p31m$	Au-$(\sqrt{3} \times \sqrt{3})$/Si(111), $(\sqrt{3} \times \sqrt{3})R30°$ rec. of Sn/Ge(111) and Sn/Si(111)
C_{6v}, $6mm$		C_{6v}^1, $P6mm$		Surface region of $CePt_5$/Pt(111) and $LaPt_5$/Pt(111)
D_{6h}, $6/mmm$		D_{6h}^1, $P6/mmm$		Bulk region of $CePt_5$/Pt(111) and $LaPt_5$/Pt(111)
O_h, $m3m$		O_h^7, $Fd3m$		Si, Ge, α-Sn

B. Compilation of relevant character tables

Character tables for relevant symmetry groups are listed together with their basis functions [43]. If required, the character tables for the double groups are given [68]. The basis functions R_c transform like axial vectors, in contrast to the radial vectors $c = x, y, z$. The basis functions for the double group representations transform like an angular momentum operator and are listed in Ref. [68].

The following symmetry operations as used in the tables:

E = Identity
i = Inversion
C_n = Rotation about an n-fold axis
σ_v = Reflection in a vertical plane
σ_h = Reflection in a horizontal plane
S_n = Rotation about an n-fold axis followed by a reflection

A bar on top of the operation symbol indicates an additional change of the sign of the spinor (only for double groups).

Table B.2.: Character table for point group C_s.

	E	σ_h	Basis functions		
A′	1	1	x, y	R_z	x^2, y^2, z^2, xy
A″	1	−1	z	R_x, R_y	yz, xz

Table B.3.: Character table for point group C_{3v}.

	E	$2C_3$	$3\sigma_v$	Basis functions		
A_1	1	1	1	z		$x^2 + y^2$, z^2
A_2	1	1	−1		R_z	
E	2	−1	0	(x, y)	(R_x, R_y)	$(x^2 - y^2, xy)$, (yz, xz)

Table B.4.: Character table for double point group C_{6v}.

		E	$\bar{E}$	C_2 $\bar{C}_2$	$2C_3$	$2\bar{C}_3$	$2C_6$	$2\bar{C}_6$	$3\sigma_d$ $3\bar{\sigma}_d$	$3\sigma_v$ $3\bar{\sigma}_v$	Basis functions		
A_1	Γ_1	1	1	1	1	1	1	1	1	1	z		$x^2+y^2,\ z^2$
A_2	Γ_2	1	1	1	1	1	1	1	-1	-1		R_z	
B_1	Γ_3	1	1	-1	1	1	-1	-1	1	-1			
B_2	Γ_4	1	1	-1	1	1	-1	-1	-1	1			
E_1	Γ_5	2	2	-2	-1	-1	1	1	0	0	(x,y)	(R_x,R_y)	(xz,yz)
E_2	Γ_6	2	2	2	-1	-1	-1	-1	0	0			(x^2-y^2,xy)
	Γ_7	2	-2	0	1	-1	$\sqrt{3}$	$-\sqrt{3}$	0	0			
	Γ_8	2	-2	0	1	-1	$-\sqrt{3}$	$\sqrt{3}$	0	0			
	Γ_9	2	-2	0	-2	2	0	0	0	0			

Table B.5.: Character table for double point group D_{6h} (continued on next page).

		E	$\bar{E}$	C_2 $\bar{C}_2$	$2C_3$	$2\bar{C}_3$	$2C_6$	$2\bar{C}_6$	$3C_2'$ $3\bar{C}_2'$	$3C_2''$ $3\bar{C}_2''$
A_{1g}	Γ_1^+	1	1	1	1	1	1	1	1	1
A_{2g}	Γ_2^+	1	1	1	1	1	1	1	−1	−1
B_{1g}	Γ_3^+	1	1	−1	1	1	−1	−1	1	−1
B_{2g}	Γ_4^+	1	1	−1	1	1	−1	−1	−1	1
E_{1g}	Γ_5^+	2	2	−2	−1	−1	1	1	0	0
E_{2g}	Γ_6^+	2	2	2	−1	−1	−1	−1	0	0
A_{1u}	Γ_1^-	1	1	1	1	1	1	1	1	1
A_{2u}	Γ_2^-	1	1	1	1	1	1	1	−1	−1
B_{1u}	Γ_3^-	1	1	−1	1	1	−1	−1	1	−1
B_{2u}	Γ_4^-	1	1	−1	1	1	−1	−1	−1	1
E_{1u}	Γ_5^-	2	2	−2	−1	−1	1	1	0	0
E_{2u}	Γ_6^-	2	2	2	−1	−1	−1	−1	0	0
	Γ_7^+	2	−2	0	1	−1	$\sqrt{3}$	$-\sqrt{3}$	0	0
	Γ_8^+	2	−2	0	1	−1	$-\sqrt{3}$	$\sqrt{3}$	0	0
	Γ_9^+	2	−2	0	−2	2	0	0	0	0
	Γ_7^-	2	−2	0	1	−1	$\sqrt{3}$	$-\sqrt{3}$	0	0
	Γ_8^-	2	−2	0	1	−1	$-\sqrt{3}$	$\sqrt{3}$	0	0
	Γ_9^-	2	−2	0	−2	2	0	0	0	0

Table B.6.: Character table for double point group D_{6h} (continued from previous page).

		i	$\bar{i}$	σ_h $\bar{\sigma}_h$	$2S_6$	$2\bar{S}_6$	$2S_3$	$2\bar{S}_3$	$3\sigma_d$ $3\bar{\sigma}_d$	$3\sigma_v$ $3\bar{\sigma}_v$	Basis functions		
A_{1g}	Γ_1^+	1	1	1	1	1	1	1	1	1			$x^2+y^2,\ z^2$
A_{2g}	Γ_2^+	1	1	1	1	1	1	1	-1	-1		R_z	
B_{1g}	Γ_3^+	1	1	-1	1	1	-1	-1	1	-1			
B_{2g}	Γ_4^+	1	1	-1	1	1	-1	-1	-1	1			
E_{1g}	Γ_5^+	2	2	-2	-1	-1	1	1	0	0		(R_x, R_y)	(xz, yz)
E_{2g}	Γ_6^+	2	2	2	-1	-1	-1	-1	0	0			(x^2-y^2, xy)
A_{1u}	Γ_1^-	-1	-1	-1	-1	-1	-1	-1	-1	-1			
A_{2u}	Γ_2^-	-1	-1	-1	-1	-1	-1	-1	1	1	z		
B_{1u}	Γ_3^-	-1	-1	1	-1	-1	1	1	-1	1			
B_{2u}	Γ_4^-	-1	-1	1	-1	-1	1	1	1	-1			
E_{1u}	Γ_5^-	-2	-2	2	1	1	-1	-1	0	0	(x, y)		
E_{2u}	Γ_6^-	-2	-2	-2	1	1	1	1	0	0			
	Γ_7^+	2	-2	0	1	-1	$\sqrt{3}$	$-\sqrt{3}$	0	0			
	Γ_8^+	2	-2	0	1	-1	$-\sqrt{3}$	$\sqrt{3}$	0	0			
	Γ_9^+	2	-2	0	-2	2	0	0	0	0			
	Γ_7^-	-2	2	0	-1	1	$-\sqrt{3}$	$\sqrt{3}$	0	0			
	Γ_8^-	-2	2	0	-1	1	$\sqrt{3}$	$-\sqrt{3}$	0	0			
	Γ_9^-	-2	2	0	2	-2	0	0	0	0			

C. Temperature dependence of Raman spectra of Si(111)

Additional Raman spectra of bulk Si(111) are presented in Fig. C.1 to show the influence of temperature on the spectra. Corresponding Raman spectra for RT are shown in Fig. 3.2(a) of which the spectrum for $z(xx)\bar{z}$ polarization configuration is included in Fig. C.1 as dashed line. The temperature-induced shift of the LTO phonon frequency can be readily observed at the upper part of the figure. The reduction of the FWHM is also apparent. The 2TA phonon structure decreases considerably with decreasing temperature. The underlying relation for this reduction is presented in Sec. 3.1. Moreover, the 2TA structure as second-order process almost vanishes in the $z(xy)\bar{z}$ spectrum at LT. Also note the splitting of the 2TA phonon structure around $\approx$300 cm^{-1} into contributions from the X and Σ point of the BZ. This is clearly observable in the $z(xx)\bar{z}$ spectrum at LT.

Similar temperature effects are also observed for the Raman spectra of bulk Ge(111) and of the adsorbate-covered substrates.

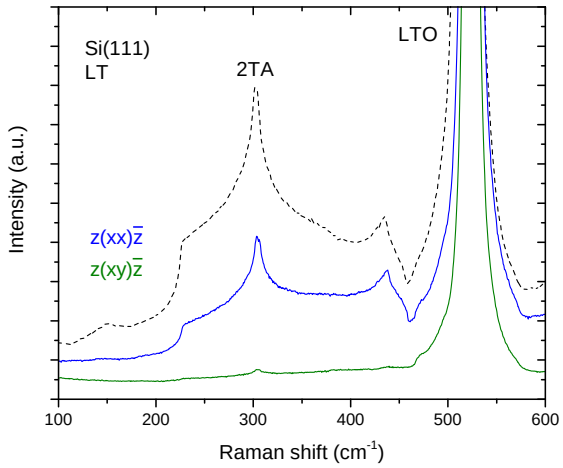

Figure C.1.: Raman spectra of the bulk semiconductor Si(111) for LT and both polarization configurations $z(xx)\bar{z}$ and $z(xy)\bar{z}$. The dashed line is the $z(xx)\bar{z}$ spectrum of Si(111) for RT as reference and is identical with the one shown in Fig. 3.2(a).

D. Raman spectra for different excitation wavelengths

Additonal Raman spectra which were recorded with different laser lines are shown for several surface and bulk systems. So far, the presented Raman spectra were

obtained by excitation with a laser line of 488 nm. Here, also spectra recorded with 514 and 633 nm are displayed. According to Eqs. (2.13) and (2.14), the Raman spectra are strongly influenced by the used excitation wavelength. For some excitation laser lines, resonant conditions can be achieved, which result in an increasing Raman intensity. By comparison of the Raman spectra for different excitation wavelengths, spectral features appearing in all spectra can be definitely assigned as Raman signals. In general, the observed intensity depends also on the used optical equipment, e.g., the grating and CCD efficiency for the specific wavelength.

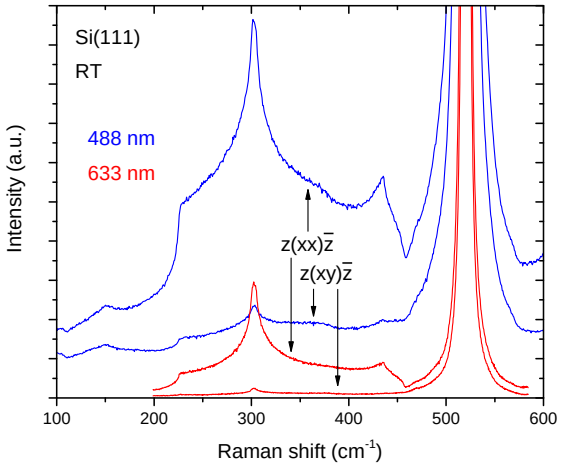

Figure D.2.: Raman spectra of the bulk semiconductor Si(111) for the excitation laser wavelengths 633 and 488 nm. The spectra were recorded at RT and are depicted for both polarization configurations $z(xx)\bar{z}$ and $z(xy)\bar{z}$. The intensity of the spectra is normalized with respect to integration time and laser power.

In Fig. D.2, Raman spectra of bulk Si(111) for 633 and 488 nm are shown. The Raman intensity is strongly reduced by changing the wavelength from 488 to 633 nm, which leads to the conclusion that the latter is less resonant. Apart from that, all spectral features of Si(111) are observable for both wavelengths. Note that the spectral range on the CCD detector varies with the used laser line as can be also seen in Fig. D.2.

A similar situation is also observed for the Raman spectra of the Ge(111)-c(2×8) surface in Fig. D.3. The spectra were obtained with the laser wavelengths 514 and 488 nm. For 514 nm (≅2.41 eV), the Raman signal is considerably enhanced due to the resonance with the energy gap $E_1 + \Delta_1$ of Ge, which has an energy of ≈2.33 eV [94,258]. The excitation with the laser line of 488 nm (≅2.54 eV) is consequently less resonant. In Ref. [94], an enhancement by a factor 2 is experimentally obtained between the two laser lines for one-phonon Raman scattering. This is in good agreement with the observation in Fig. D.3.

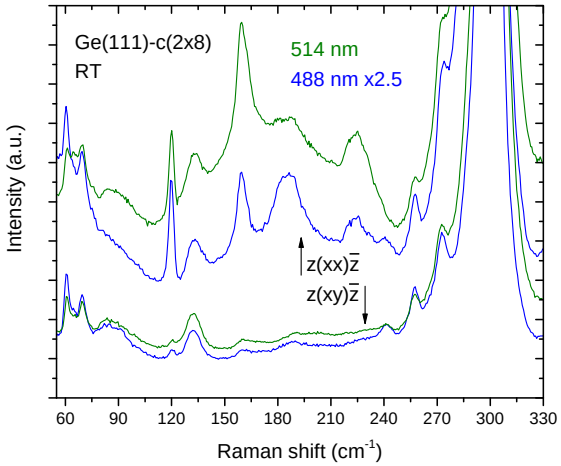

Figure D.3.: Raman spectra of the Ge(111)-c(2×8) surface reconstruction for the excitation laser wavelengths 514 and 488 nm. The spectra were recorded at RT and are depicted for both polarization configurations $z(xx)\bar{z}$ and $z(xy)\bar{z}$. The intensity of the spectra is normalized with respect to integration time and laser power. Note that the spectra for 488 nm are multiplied by a factor of 2.5.

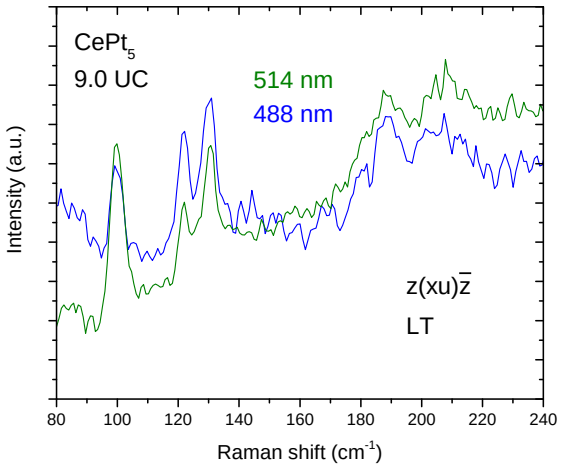

Figure D.4.: Raman spectra of $CePt_5$/Pt(111) for LT for the excitation laser wavelengths 514 and 488 nm. The spectra were recorded at LT and are depicted for the polarization configuration $z(xu)\bar{z}$. The intensity of the spectra is normalized with respect to integration time and laser power.

In Fig. D.4, Raman spectra for 514 and 488 nm are shown for $CePt_5$/Pt(111) with a film thickness of 9.0 UC. In these unpolarized spectra, the CFE Raman peaks (like the vibrational excitations) are clearly observed for both laser wavelengths.

No resonance behavior is observed for the intermetallic films.

E. Raman spectrum with plasma lines for calibration

An exemplary Raman spectrum with plasma lines of the Ar^+ ion gas laser is shown in Fig. E.5. The $z(xx)\bar{z}$ spectrum was recorded for a Si(111) substrate at RT and is depicted together with a reference spectrum with applied plasma line filter. The positions of the plasma lines (including the laser line) together with tabulated frequency values of the plasma lines are used for the calibration of the Raman spectra. To get the peak positions of the plasma lines in the spectrum, the peaks are fitted by Voigt profiles. From Fig. E.5 it is also apparent that no plasma lines leak through the filter.

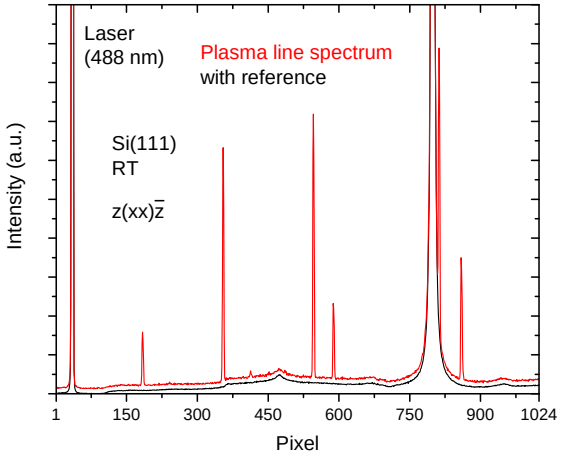

Figure E.5.: Raman spectrum with plasma lines of the Ar^+ ion gas laser for a Si(111) substrate. For reference, a spectrum with applied plasma line filter is shown and shifted for clarity. Prior to calibration, the pixels of the CCD detector are noted. The laser line had a wavelength of 488 nm.

F. Additional information on the preparation procedures

More details on the preparation procedures of the surface adsorbate systems are provided in this section. The relevant parameters that need to be controlled during the preparation of the clean semiconductor substrates are the sample temperature, the heating power of the direct current power supply, and the pressure in the UHV

chamber. When metal atoms are deposited on the substrate, the flux of the adatoms also needs to be considered.

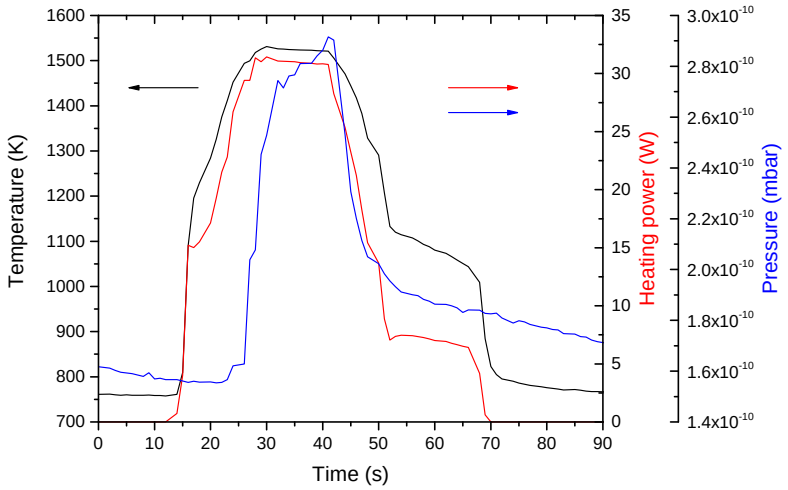

Figure F.6.: Preparation procedure for a flash annealing process for Si(111) to obtain the Si(111)-(7×7) reconstruction. The sample temperature, the heating power of the direct current power supply, and the pressure in the UHV chamber are plotted over time.

In Fig. F.6, the flash annealing procedure to prepare the clean semiconductor surface Si(111)-(7×7) is shown. The corresponding preparation is described in Sec. 3.2.1. After a sharp increase, the temperature is decreased and finally RT is approached. The temperature follows the heating power very closely. Instead, the pressure rises after a short time delay and decreases slowly after the sample temperature is lowered. In some cases, several flash annealing cycles are needed to get a very low pressure during the flash annealing process, which also is a good indication for a clean surface.

A similar procedure is used to obtain the clean semiconductor surface Ge(111)-c(2×8) as depicted in Fig. F.7. The corresponding preparation is also described in Sec. 3.2.1. In general, the annealing temperature is lower than in the case of Si(111)-(7×7). The thermal treatment is applied after Ar^+ ion sputtering.

After preparation of the clean semiconductor surfaces, adatoms are deposited on the substrates to obtain the adsorbate reconstructions. The flux of atoms of the evaporator is controlled by a quartz crystal microbalance.

In Fig. F.8, an exemplary frequency development for a Sn flux of 200 nA is depicted. The rate, i.e., the slope, is determined by linear fitting. With this rate and the calculated frequency shift for the desired coverage, the time, during which the evaporation shutter must be opened, can be obtained.

After Sn deposition, the samples is annealed again. Such an annealing process is shown for Sn/Si(111) in Fig. F.9. The corresponding preparation is also described in

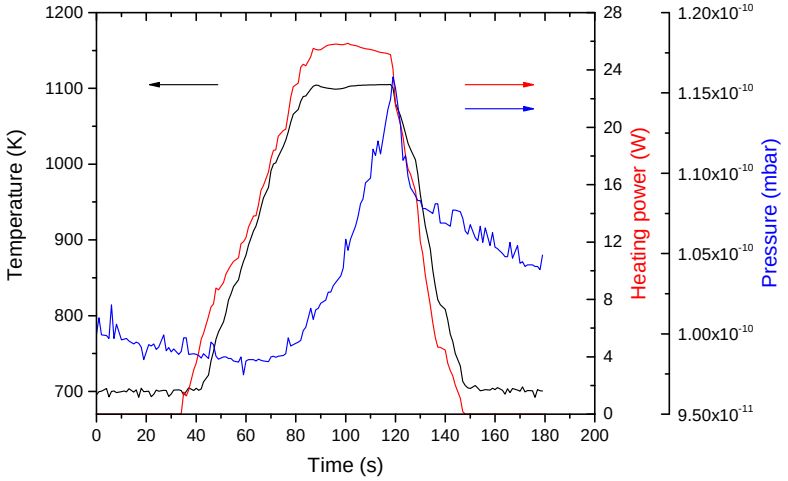

Figure F.7.: Preparation procedure for an annealing process for Ge(111) to obtain the Ge(111)-c(2×8) reconstruction. The sample temperature, the heating power of the direct current power supply, and the pressure in the UHV chamber are plotted over time.

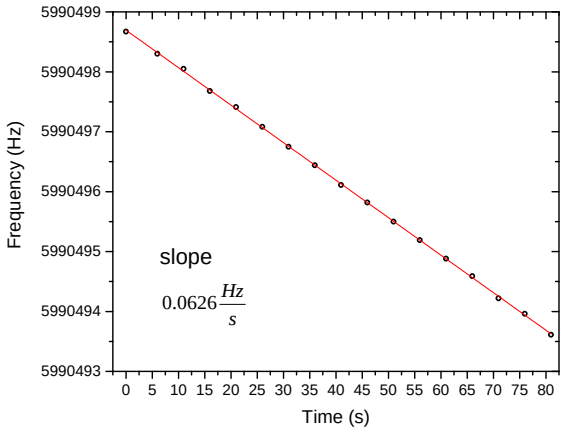

Figure F.8.: Frequency development during Sn deposition of the quartz crystal that is used in the quartz crystal microbalance. The flux of the evaporator is kept constant. The data points are fitted by a linear fit.

Sec. 3.4.2. Note the decreasing of the heating power which is related to the decrease of the electrical resistance of the sample. Due to the increasing temperature of the sample and the environment, an increasing number of conduction electrons participate. Therefore, the voltage drops, while the electric current is kept constant.

Similar preparation procedures are also used in the case of Ge(111) as substrate.

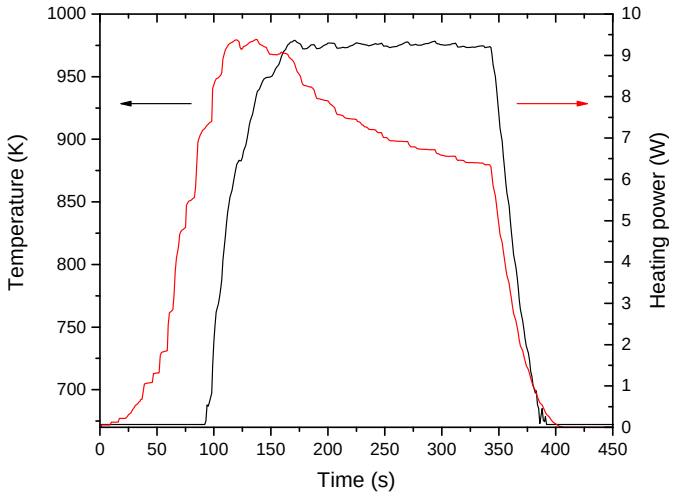

Figure F.9.: Preparation procedure for an annealing process after deposition of Sn on Si(111). After annealing the Sn-($\sqrt{3} \times \sqrt{3}$)/Si(111) reconstruction is obtained. The sample temperature and the heating power of the direct current power supply are plotted over time.

G. Optical characteristics of used laser-line filters

The Raman spectra were recorded by applying two types of laser-line filters, i.e., edge filters and Bragg notch filters. Both types have advantages and disadvantages with respect to the experimental requirements. To examine the filter characteristics, it is useful to replace the laser with a cold light source. In theory, the observed spectrum should be a smooth curve whose intensity only slightly varies in the visible spectral range. The cold light source is placed in front of the spectrometer in direction of the sample.

Two spectra with an applied edge filter (for the laser line with a wavelength of 488 nm) in two different positions (0° and 10°) are shown in Fig. G.10. As can be seen in the figure, the filter edge can be shifted by rotation of the filter (around a vertical axis). Nearly all intensity passes the filter above the filter edge (i.e., the Stokes side for Raman processes). On the other hand, the transmitted intensity drops by several orders on the shorter wavelength side of the edge. Note the slight intensity oscillations close to the filter edge that are only clearly observed for high intensities.

A different characteristic is observed for the Bragg notch filters as depicted in Fig. G.11. It is necessary to utilize two Bragg notch filters to achieve a laser suppression that is high enough. At the laser wavelength of 488 nm a narrow dip suppresses the laser intensity, while light with different wavelengths can pass the filters. Hence, anti-Stokes and Stokes Raman processes are observable. However, the transmittance is not as high as for an edge filter. Note the intensity steps on

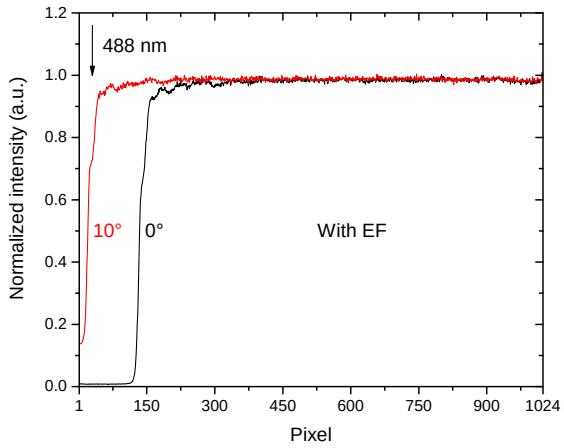

Figure G.10.: Spectra recorded with an applied edge filter (EF). The wavelength of 488 nm is marked. A spectrum for perpendicular incidence of the laser beam (0°) on the filter is shown as well as a spectrum with a rotated filter (10°). The intensities are normalized with respect to a spectrum obtained without filters.

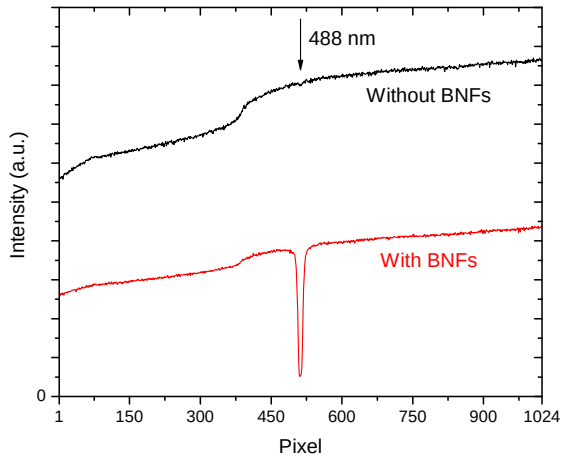

Figure G.11.: Spectra recorded with and without Bragg notch filters (BNFs). The wavelength of 488 nm is marked.

the anti-Stokes side, which are ascribed to changes in the grating efficiency due to blazing. Such steps are not observed for the Stokes side. Therefore, care must be taken when the sample temperature is obtained by the ratio of the anti-Stokes to the Stokes spectrum according to Eq. (2.9).

Acronyms

1D one-dimensional

1U2D 1 up, 2 down

2D two-dimensional

2TA second-order transversal acoustic

2U1D 2 up, 1 down

3D three-dimensional

AN Abukawa-Nishigaya

ARPES angle-resolved photoemission spectroscopy

BZ Brillouin zone

CCD charge coupled device

CDW charge-density wave

CF crystal field

CFE crystal-field excitation

CHCT conjugate honeycomb-chained-trimer

COI charge ordered insulator

DAS dimer-adatom-stacking fault

DB dangling bond

DF dynamical fluctuation

DFT density-functional theory

EBH Erwin-Barke-Himpsel

FCC face centered cubic

FWHM full width at half maximum

GGA generalized gradient approximation

H_3-MTL H_3-missing-top-layer

HAS helium atom scattering

HCT honeycomb-chained-trimer

HREELS high-resolution electron energy loss spectroscopy

INS inelastic neutron scattering

IR infrared

KK Kwon-Kang

LA longitudinal acoustic

LDA local-density approximation

LEED low-energy electron diffraction

LO longitudinal optic

LT low temperature ($T \approx 20-40\,\mathrm{K}$)

LTO longitudinal-transversal optical

MBE molecular beam epitaxy

MD molecular dynamics

MEIS medium-energy ion scattering

ML monolayer

PBE Perdew-Burke-Ernzerhof

PDOS phonon density of states

PLD periodic lattice distortion

RAS reflectance anisotropy spectroscopy

RHEED reflection high-energy electron diffraction

RKKY Ruderman-Kittel-Kasuya-Yosida

RS Raman spectroscopy

RT room temperature ($T \approx 300\,\mathrm{K}$)

RW Rayleigh wave

SBZ surface Brillouin zone

SERS surface-enhanced Raman scattering

SOC spin-orbit coupling

SPT structural phase transition

SRS surface Raman spectroscopy

STM scanning tunneling microscopy

STS scanning tunneling spectroscopy

SUC surface unit cell

TA transversal acoustic

TIRS transmission infrared spectroscopy

TLL Tomonaga-Luttinger liquid

TO transversal optic

TT twisted-trimer

UC unit cell

UHV ultrahigh vacuum

XAS x-ray absorption spectroscopy

XC exchange-correlation

XLD x-ray linear dichroism

XMCD x-ray magnetic circular dichroism

XPS x-ray photoemission spectroscopy

XRD x-ray diffraction

List of contributions

Publications

- M. Liebhaber, B. Halbig, U. Bass, J. Geurts, S. Neufeld, S. Sanna, W. G. Schmidt, E. Speiser, J. Räthel, S. Chandola, and N. Esser
  Vibration eigenmodes of the Au-(5×2)/Si(111) surface studied by Raman spectroscopy and first-principles calculations
  Physical Review B, **94**, 235304 (2016)

- B. Halbig*, U. Bass, J. Geurts, M. Zinner*, and K. Fauth
  Study of crystal-field splitting in ultrathin $CePt_5$ films by Raman spectroscopy
  Physical Review B, **95**, 165115 (2017)
  * Both authors contributed equally.

- B. Halbig, M. Liebhaber, U. Bass, J. Geurts, E. Speiser, J. Räthel, S. Chandola, N. Esser, M. Krenz, S. Neufeld, W. G. Schmidt, and S. Sanna
  Vibrational properties of the Au-($\sqrt{3} \times \sqrt{3}$)/Si(111) surface reconstruction
  Physical Review B, **97**, 035412 (2018)

- E. Speiser, J. Plaickner, S. Chandola, N. Esser, B. Halbig, and J. Geurts
  Raman Spectroscopy on Surface Phonons of Si(hhk) Surfaces Modified by Au Submonolayers
  Physica Status Solidi B, **256**, 1800341 (2019)

- M. Zinner*, K. Fauth, B. Halbig*, U. Bass, and J. Geurts
  Raman study of the vibration eigenmodes of $CePt_5$ films on Pt(111)
  Materials Research Express, **6**, 026416 (2019)
  * Both authors contributed equally.

- B. Halbig, U. Bass, J. Geurts, and S. Sanna
  Vibrational signatures of the structural phase transition of Sn/Ge(111) compared to Sn/Si(111)
  Submitted for publication (2018)

- S. Schreyeck, B. Halbig, J. Geurts, G. Karczewski, K. Brunner, and L. W. Molenkamp
  Structural characterization of α-Sn grown on CdTe by molecular beam epitaxy
  In preparation

- E. Speiser, N. Esser, B. Halbig, J. Geurts, W. G. Schmidt, and S. Sanna
  Vibrational Raman Spectroscopy on Adsorbate-Induced Low-Dimensional Surface Structures
  In preparation (Review article for Surface Science Reports. Letter of agreement with Editor established.)

Conference contributions and talks

- Talk at the Leibniz-Institut für Analytische Wissenschaften - ISAS - e.V. in Berlin (Germany), 2015:
  - B. Halbig, U. Bass, J. Geurts, M. Zinner, C. Praetorius, and K. Fauth
    Raman spectroscopy of intermetallic surface compounds $CePt_5$/Pt(111) and $LaPt_5$/Pt(111)

- Poster at the Frühjahrstagung der Deutschen Physikalischen Gesellschaft (DPG) in Regensburg (Germany), 2016:
  - B. Halbig, U. Bass, M. Zinner, K. Fauth, and J. Geurts
    Raman spectroscopy of crystal field excitations and vibration modes in $CePt_5$ surface layers

- Posters at the ToCoTronics Conference in Würzburg (Germany), 2016:
  - B. Halbig, M. Liebhaber, U. Bass, J. Geurts, E. Speiser, J. Räthel, A. Baumann, S. Chandola, N. Esser, S. Neufeld, S. Sanna, and W. G. Schmidt
    Analysis of the vibration eigenmodes of the ordered adsorbate surface Au-(5×2)/Si(111) by Raman spectroscopy and first-principle calculations
  - B. Halbig, U. Bass, J. Geurts, M. Zinner, and K. Fauth
    Investigation of electronic crystal field excitations and vibrational modes in $CePt_5$ layers on Pt(111) by Raman spectroscopy

- Posters at the European Conference on Surface Science (ECOSS) in Grenoble (France), 2016:
  - B. Halbig, M. Liebhaber, U. Bass, J. Geurts, E. Speiser, J. Räthel, A. Baumann, S. Chandola, N. Esser, S. Neufeld, S. Sanna, and W. G. Schmidt
    Raman study of the vibration eigenmodes of the ordered adsorbate surface Au-(5×2)/Si(111)
  - B. Halbig, U. Bass, J. Geurts, M. Zinner, and K. Fauth
    Lattice dynamics and crystal field splitting in $CePt_5$ layers on Pt(111), determined by Raman spectroscopy

- Poster at the Frühjahrstagung der Deutschen Physikalischen Gesellschaft (DPG) in Dresden (Germany), 2017:
  - B. Halbig, M. Liebhaber, U. Bass, J. Geurts, E. Speiser, J. Räthel, S. Chandola, N. Esser, M. Krenz, S. Neufeld, W. G. Schmidt, and S. Sanna
    Vibrational eigenmodes of the Au-($\sqrt{3} \times \sqrt{3}$)/Si(111) surface reconstruction examined by Raman spectroscopy and first-principles calculations

- Posters at the International Conference on Optics of Surfaces and Interfaces (OSI) in Dublin (Ireland), 2017:
  - B. Halbig, U. Bass, and J. Geurts
    Temperature dependent surface Raman spectroscopy of the Sn-($\sqrt{3} \times \sqrt{3}$)/Si(111) reconstruction
  - B. Halbig, M. Liebhaber, U. Bass, J. Geurts, E. Speiser, J. Räthel, S. Chandola, N. Esser, M. Krenz, S. Neufeld, W. G. Schmidt, and S. Sanna
    Surface Raman spectroscopy and first-principles calculations of the vibrational modes of the Au-($\sqrt{3} \times \sqrt{3}$)/Si(111) reconstruction

- Poster at the Frühjahrstagung der Deutschen Physikalischen Gesellschaft (DPG) in Berlin (Germany), 2018:
  - B. Halbig, U. Bass, and J. Geurts
    Vibrational eigenmodes of the Sn-($\sqrt{3} \times \sqrt{3}$)/Si(111) reconstruction observed by surface Raman spectroscopy

- Poster at European Conference on Surface Science (ECOSS) in Aarhus (Denmark), 2018:
  - B. Halbig, U. Bass, and J. Geurts
    Surface vibrations of Sn/Si(111) and Sn/Ge(111) studied by temperature-dependent Raman spectroscopy

Bibliography

[1] F. J. Himpsel, K. N. Altmann, R. Bennewitz, J. N. Crain, A. Kirakosian, J.-L. Lin, and J. L. McChesney, Journal of Physics: Condensed Matter **13**, 11097 (2001).

[2] A. Tejeda, Y. Fagot-Révurat, R. Cortés, D. Malterre, E. G. Michel, and A. Mascaraque, physica status solidi (a) **209**, 614 (2012).

[3] D. V. Gruznev, A. V. Zotov, and A. A. Saranin, Japanese Journal of Applied Physics **56**, 08LA01 (2017).

[4] A. Trovarelli, Catalysis Reviews **38**, 439 (1996).

[5] P. Malacrida, M. Escudero-Escribano, A. Verdaguer-Casadevall, I. E. Stephens, and I. Chorkendorff, Journal of Materials Chemistry A **2**, 4234 (2014).

[6] M. Escudero-Escribano, P. Malacrida, M. H. Hansen, U. G. Vej-Hansen, A. Velázquez-Palenzuela, V. Tripkovic, J. Schiøtz, J. Rossmeisl, I. E. L. Stephens, and I. Chorkendorff, Science **352**, 73 (2016).

[7] F. J. Himpsel, A. Kirakosian, J. N. Crain, J.-L. Lin, and D. Y. Petrovykh, Solid State Communications **117**, 149 (2001).

[8] R. Bennewitz, J. N. Crain, A. Kirakosian, J.-L. Lin, J. L. McChesney, D. Y. Petrovykh, and F. J. Himpsel, Nanotechnology **13**, 499 (2002).

[9] F.-C. Chuang, C.-H. Hsu, H.-L. Chou, C. P. Crisostomo, Z.-Q. Huang, S.-Y. Wu, C.-C. Kuo, W.-C. V. Yeh, H. Lin, and A. Bansil, Physical Review B **93**, 035429 (2016).

[10] F. Bechstedt, *Principles of Surface Physics* (Springer, Berlin, 2003).

[11] G. P. Srivastava, *The Physics of Phonons* (Adam Hilger, Bristol, 1990).

[12] P. Yu and M. Cardona, *Fundamentals of Semiconductors*, 4th ed. (Springer, Berlin, 2010).

[13] W. Weber, Physical Review B **15**, 4789 (1977).

[14] M. Cardona, ed., *Light Scattering in Solids I: Introductory Concepts*, 2nd ed., Vol. 8 (Springer, Berlin, 1983).

[15] H. Lüth, *Solid Surfaces, Interfaces and Thin Films*, 6th ed. (Springer, Berlin, 2015).

[16] V. Wagner, J. Wagner, S. Gundel, L. Hansen, and J. Geurts, Physical Review Letters **89**, 166103 (2002).

[17] N. Esser and W. Richter, in *Light Scattering in Solids VIII: Fullerenes, Semiconductor Surfaces, Coherent Phonons*, Vol. 76, edited by M. Cardona and G. Güntherodt (Springer, Berlin, 2000) pp. 96–168.

[18] J. C. Vickerman and I. S. Gilmore, eds., *Surface Analysis - The Principal Techniques*, 2nd ed. (Wiley, West Sussex, 2009).

[19] C. Hogan, E. Ferraro, N. McAlinden, and J. F. McGilp, Physical Review Letters **111**, 087401 (2013).

[20] C. Hogan, E. Speiser, S. Chandola, S. Suchkova, J. Aulbach, J. Schäfer, S. Meyer, R. Claessen, and N. Esser, Physical Review Letters **120**, 166801 (2018).

[21] Y. Caudano, P. Thiry, and Y. Chabal, Surface Science **502**, 91 (2002).

[22] L. J. Webb, S. Rivillon, D. J. Michalak, Y. J. Chabal, and N. S. Lewis, The Journal of Physical Chemistry B **110**, 7349 (2006).

[23] G. Benedek and J. Toennies, Surface Science **299**, 587 (1994).

[24] W. Daum, H. Ibach, and J. E. Müller, Physical Review Letters **59**, 1593 (1987).

[25] G. Benedek, I. Sklyadneva, E. Chulkov, P. Echenique, R. Heid, K.-P. Bohnen, D. Schmicker, S. Schmidt, and J. Toennies, Surface Science **678**, 38 (2018).

[26] H. Asada, T. Toya, H. Motohashi, M. Sakamoto, and Y. Hamaguchi, The Journal of Chemical Physics **63**, 4078 (1975).

[27] H. Ibach and D. L. Mills, *Electron Energy Loss Spectroscopy and Surface Vibrations* (Academic Press, New York, 1982).

[28] H. Nienhaus and W. Mönch, Surface Science **328**, L561 (1995).

[29] H. Nienhaus, Physical Review B **56**, 13194 (1997).

[30] J. Lobo, D. Farías, E. Hulpke, J. P. Toennies, and E. G. Michel, Physical Review B **74**, 035303 (2006).

[31] K. L. Kostov, S. Polzin, S. K. Saha, O. Brovko, V. Stepanyuk, and W. Widdra, Physical Review B **87**, 235416 (2013).

[32] A. Groß, *Theoretical Surface Science - A Microscopic Perspective*, 3rd ed. (Springer, Berlin, 2009).

[33] B. Halbig, M. Liebhaber, U. Bass, J. Geurts, E. Speiser, J. Räthel, S. Chandola, N. Esser, M. Krenz, S. Neufeld, W. G. Schmidt, and S. Sanna, Physical Review B **97**, 035412 (2018).

[34] M. Liebhaber, B. Halbig, U. Bass, J. Geurts, S. Neufeld, S. Sanna, W. G. Schmidt, E. Speiser, J. Räthel, S. Chandola, and N. Esser, Physical Review B **94**, 235304 (2016).

[35] G. Czycholl, *Theoretische Festkörperphysik*, 3rd ed. (Springer, Berlin, 2008).

[36] W. Kohn and L. J. Sham, Physical Review **140**, A1133 (1965).

[37] D. M. Ceperley and B. J. Alder, Physical Review Letters **45**, 566 (1980).

[38] J. P. Perdew, J. A. Chevary, S. H. Vosko, K. A. Jackson, M. R. Pederson, D. J. Singh, and C. Fiolhais, Physical Review B **46**, 6671 (1992).

[39] J. P. Perdew, K. Burke, and M. Ernzerhof, Physical Review Letters **77**, 3865 (1996).

[40] P. G. Klemens, Physical Review **148**, 845 (1966).

[41] T. R. Hart, R. L. Aggarwal, and B. Lax, Physical Review B **1**, 638 (1970).

[42] G. Schaack, in *Light Scattering in Solids VII: Crystal-Field and Magnetic Excitations*, Vol. 75, edited by M. Cardona and G. Güntherodt (Springer, Berlin, 2000) pp. 24–173.

[43] R. C. Powell, *Symmetry, Group Theory, and the Physical Properties of Crystals* (Springer, New York, 2010).

[44] M. S. Dresselhaus, G. Dresselhaus, and A. Jorio, *Group Theory* (Springer, Berlin, 2008).

[45] M. J. Klein, American Journal of Physics **20**, 65 (1952).

[46] K. Ahrens, *Ramanspektroskopische Untersuchungen zu magnetoelastischen Wechselwirkung im* $Ce_cLa_{1-c}F_3$, Ph.D. thesis, Universität Würzburg (1978).

[47] N. Esser and J. Geurts, in *Optical Characterization of Epitaxial Semiconductor Layers*, edited by G. Bauer and W. Richter (Springer, Berlin, 1996) pp. 129–202.

[48] J. Geurts, Surface Science Reports **18**, 1 (1993).

[49] J. Geurts, Progress in Crystal Growth and Characterization of Materials **32**, 185 (1996).

[50] G. Placzek, in *Handbuch der Radiologie*, Vol. 6/II, edited by M. E. (Akademische Verlagsgesellschaft, Leipzig, 1934) pp. 205–374.

[51] B. R. Masters, Optics and Photonics News **20**, 40 (2009).

[52] A. Smekal, Naturwissenschaften **11**, 873 (1923).

[53] H. A. Kramers and W. Heisenberg, Zeitschrift für Physik **31**, 681 (1925).

[54] P. A. M. Dirac, Proceedings of the Royal Society of London A: Mathematical, Physical and Engineering Sciences **114**, 710 (1927).

[55] C. V. Raman, Indian Journal of Physics **2**, 387 (1928).

[56] C. V. Raman, Current Science **74**, 382 (1998).

[57] C. V. Raman and K. S. Krishnan, Nature **121**, 501 (1928).

[58] G. Landsberg and L. Mandelstam, Naturwissenschaften **16**, 557 (1928).

[59] R. Loudon, Advances in Physics **13**, 423 (1964).

[60] G. Bauer and W. Richter, eds., *Optical Characterization of Epitaxial Semiconductor Layers* (Springer, Berlin, 1996).

[61] M. Cardona and G. Güntherodt, eds., *Light Scattering in Solids II: Basic Concepts and Instrumentation*, Vol. 50 (Springer, Berlin, 1982).

[62] M. Veithen, X. Gonze, and P. Ghosez, Physical Review B **71**, 125107 (2005).

[63] C. Chen, E. Burstein, and S. Lundquist, Solid State Communications **32**, 63 (1979).

[64] R. Monreal, F. Flores, Y. Gao, and T. López-Ríos, EPL (Europhysics Letters) **4**, 115 (1987).

[65] N. Esser, Applied Physics A **69**, 507 (1999).

[66] A. Otto, Journal of Raman Spectroscopy **22**, 743 (1991).

[67] E. Speiser, K. Hinrichs, P. Prete, N. Lovergine, and N. Esser, physica status solidi (b) **252**, 11 (2015).

[68] G. F. Koster, J. O. Dimmock, R. G. Wheeler, and H. Statz, *Properties of the thirty-two point groups* (M.I.T. Press, Cambridge, Massachusetts, 1963).

[69] A. I. Bobrysheva, S. A. Moskalenko, and V. T. Zyukov, physica status solidi (b) **111**, K75 (1982).

[70] T. Terzibaschian and B. Enderlein, physica status solidi (b) **133**, 443 (1986).

[71] D. L. Rousseau, R. P. Bauman, and S. P. S. Porto, Journal of Raman Spectroscopy **10**, 253 (1981).

[72] E. Kroumova, M. Aroyo, J. Perez-Mato, A. Kirov, C. Capillas, S. Ivantchev, and H. Wondratschek, Phase Transitions **76**, 155 (2003).

[73] R. Elliott and R. Loudon, Physics Letters **3**, 189 (1963).

[74] G. Schaack, Zeitschrift für Physik B Condensed Matter **26**, 49 (1977).

[75] A. Kiel and S. Porto, Journal of Molecular Spectroscopy **32**, 458 (1969).

[76] I. Gregora, in *International Tables for Crystallography*, Vol. D, edited by A. Authier (Wiley, West Sussex, 2013) Chap. 2.3, pp. 334–348.

[77] N. C. Craig and I. W. Levin, Applied Spectroscopy **33**, 475 (1979).

[78] T. Sundius, Journal of Raman Spectroscopy **1**, 471 (1973).

[79] L. Ward, *The Optical Constants of Bulk Materials and Films*, 2nd ed. (Institute of Physics Publishing, Bristol, 1994).

[80] T. C. Damen, S. P. S. Porto, and B. Tell, Physical Review **142**, 570 (1966).

[81] T. Satō, Japanese Journal of Applied Physics **6**, 339 (1967).

[82] D. E. Aspnes and A. A. Studna, Physical Review B **27**, 985 (1983).

[83] P. Sprau, *Ultradünne magnetische Lagen aus seltenen Erden in Silizium*, Diploma thesis, Universität Würzburg (2012).

[84] E. A. Wood, Journal of Applied Physics **35**, 1306 (1964).

[85] K. Cho and E. Kaxiras, Surface Science **396**, L261 (1998).

[86] G. Kresse and J. Furthmüller, Computational Materials Science **6**, 15 (1996).

[87] G. Kresse and J. Furthmüller, Physical Review B **54**, 11169 (1996).

[88] E. Speiser, J. Plaickner, S. Chandola, N. Esser, B. Halbig, and J. Geurts, physica status solidi (b) **256**, 1800341 (2019).

[89] P. A. Temple and C. E. Hathaway, Physical Review B **7**, 3685 (1973).

[90] K. Uchinokura, T. Sekine, and E. Matsuura, Journal of Physics and Chemistry of Solids **35**, 171 (1974).

[91] B. A. Weinstein and M. Cardona, Physical Review B **7**, 2545 (1973).

[92] W. Zhang, S. Sang, C. Xue, and D. Papadimitriou, Journal of Raman Spectroscopy **36**, 777 (2005).

[93] A. Zwick and R. Carles, Physical Review B **48**, 6024 (1993).

[94] M. A. Renucci, J. B. Renucci, R. Zeyher, and M. Cardona, Physical Review B **10**, 4309 (1974).

[95] J. B. Renucci, R. N. Tyte, and M. Cardona, Physical Review B **11**, 3885 (1975).

[96] J. H. Parker, D. W. Feldman, and M. Ashkin, Physical Review **155**, 712 (1967).

[97] A. Compaan, M. C. Lee, and G. J. Trott, Physical Review B **32**, 6731 (1985).

[98] D. J. Chadi and C. Chiang, Physical Review B **23**, 1843 (1981).

[99] R. E. Schlier and H. E. Farnsworth, The Journal of Chemical Physics **30**, 917 (1959).

[100] M. Liebhaber, U. Bass, P. Bayersdorfer, J. Geurts, E. Speiser, J. Räthel, A. Baumann, S. Chandola, and N. Esser, Physical Review B **89**, 045313 (2014).

[101] P. Höpfner, *Two-Dimensional Electron Systems at Surfaces - Spin-Orbit Interaction and Electronic Correlations*, Ph.D. thesis, Universität Würzburg (2012).

[102] K. Takayanagi, Y. Tanishiro, S. Takahashi, and M. Takahashi, Surface Science **164**, 367 (1985).

[103] J. Ortega, F. Flores, and A. L. Yeyati, Physical Review B **58**, 4584 (1998).

[104] S. Modesti, H. Gutzmann, J. Wiebe, and R. Wiesendanger, Physical Review B **80**, 125326 (2009).

[105] I. Štich, J. Kohanoff, and K. Terakura, Physical Review B **54**, 2642 (1996).

[106] M. Smeu, H. Guo, W. Ji, and R. A. Wolkow, Physical Review B **85**, 195315 (2012).

[107] G. Lange, J. P. Toennies, P. Ruggerone, and G. Benedek, EPL (Europhysics Letters) **41**, 647 (1998).

[108] L. Liu, C. S. Jayanthi, and S.-Y. Wu, Physical Review B **68**, 201301(R) (2003).

[109] J. Kim, M.-L. Yeh, F. S. Khan, and J. W. Wilkins, Physical Review B **52**, 14709 (1995).

[110] J. Räthel, *Strukturcharakterisierung Gold-induzierter Germanium- und Siliziumoberflächenrekonstruktionen mit Raman-Spektroskopie*, Ph.D. thesis, Technische Universität Berlin (2015).

[111] R. S. Becker, J. A. Golovchenko, and B. S. Swartzentruber, Physical Review Letters **54**, 2678 (1985).

[112] R. S. Becker, B. S. Swartzentruber, J. S. Vickers, and T. Klitsner, Physical Review B **39**, 1633 (1989).

[113] N. Takeuchi, A. Selloni, and E. Tosatti, Physical Review B **51**, 10844 (1995).

[114] J. Räthel, E. Speiser, N. Esser, U. Bass, S. Meyer, J. Schäfer, and J. Geurts, Physical Review B **86**, 035312 (2012).

[115] P. Molinàs-Mata and J. Zegenhagen, Solid State Communications **84**, 393 (1992).

[116] N. Takeuchi, A. Selloni, and E. Tosatti, Physical Review Letters **69**, 648 (1992).

[117] L. Dobrzynski and D. Mills, Journal of Physics and Chemistry of Solids **30**, 1043 (1969).

[118] L. Dobrzynski and D. L. Mills, Physical Review B **7**, 1322 (1973).

[119] G. Nelin and G. Nilsson, Physical Review B **5**, 3151 (1972).

[120] J. Kautz, M. W. Copel, M. S. Gordon, R. M. Tromp, and S. J. van der Molen, Physical Review B **89**, 035416 (2014).

[121] D. Grozea, E. Landree, L. Marks, R. Feidenhans'l, M. Nielsen, and R. Johnson, Surface Science **418**, 32 (1998).

[122] D. Grozea, E. Bengu, and L. Marks, Surface Science **461**, 23 (2000).

[123] C. H. Patterson, Journal of Physics: Condensed Matter **27**, 475001 (2015).

[124] S. Sanna, T. Lichtenstein, Z. Mamiyev, C. Tegenkamp, and H. Pfnür, The Journal of Physical Chemistry C **122**, 25580 (2018).

[125] J. L. McChesney, J. N. Crain, V. Pérez-Dieste, F. Zheng, M. C. Gallagher, M. Bissen, C. Gundelach, and F. J. Himpsel, Physical Review B **70**, 195430 (2004).

[126] S. C. Erwin, I. Barke, and F. J. Himpsel, Physical Review B **80**, 155409 (2009).

[127] T. Abukawa and Y. Nishigaya, Physical Review Letters **110**, 036102 (2013).

[128] S. G. Kwon and M. H. Kang, Physical Review Letters **113**, 086101 (2014).

[129] K. Seino and F. Bechstedt, Physical Review B **90**, 165407 (2014).

[130] T. Shirasawa, W. Voegeli, T. Nojima, Y. Iwasawa, Y. Yamaguchi, and T. Takahashi, Physical Review Letters **113**, 165501 (2014).

[131] F. Hötzel, K. Seino, C. Huck, O. Skibbe, F. Bechstedt, and A. Pucci, Nano Letters **15**, 4155 (2015).

[132] C. H. Patterson, S. Banerjee, and J. F. McGilp, Physical Review B **94**, 165417 (2016).

[133] E. H. Do, S. G. Kwon, M. H. Kang, and H. W. Yeom, Scientific Reports **8**, 15537 (2018).

[134] M. Chester and T. Gustafsson, Physical Review B **42**, 9233 (1990).

[135] M. Chester and T. Gustafsson, Surface Science **256**, 135 (1991).

[136] Y. Ding, C. Chan, and K. Ho, Surface Science **275**, L691 (1992).

[137] H. M. Zhang, T. Balasubramanian, and R. I. G. Uhrberg, Physical Review B **66**, 165402 (2002).

[138] T. Kadohira, J. Nakamura, and S. Watanabe, e-Journal of Surface Science and Nanotechnology **2**, 146 (2004).

[139] J. Y. Lee and H. M. Kang, Journal of the Korean Physical Society **55**, 2460 (2009).

[140] A. Georges, AIP Conference Proceedings **715**, 3 (2004).

[141] C. Blumenstein, J. Schäfer, S. Mietke, and S. Meyer, Nature Physics **7**, 776 (2011).

[142] Y. Ōnuki, *Physics of Heavy Fermions* (World Scientific, New Jersey, 2018).

[143] K. Rossnagel, Journal of Physics: Condensed Matter **23**, 213001 (2011).

[144] P. C. Snijders and H. H. Weitering, Reviews of Modern Physics **82**, 307 (2010).

[145] K. N. Altmann, J. N. Crain, A. Kirakosian, J.-L. Lin, D. Y. Petrovykh, F. J. Himpsel, and R. Losio, Physical Review B **64**, 035406 (2001).

[146] S. G. Kwon and M. H. Kang, Physical Review B **92**, 195301 (2015).

[147] H. Lipson and K. E. Singer, Journal of Physics C: Solid State Physics **7**, 12 (1974).

[148] I. Barke, S. Polei, V. v. Oeynhausen, and K.-H. Meiwes-Broer, Physical Review Letters **109**, 066801 (2012).

[149] E. H. Do and H. W. Yeom, Physical Review Letters **115**, 266803 (2015).

[150] W. G. Schmidt, S. Glutsch, P. H. Hahn, and F. Bechstedt, Physical Review B **67**, 085307 (2003).

[151] D. Dornisch, W. Moritz, H. Schulz, R. Feidenhans'l, M. Nielsen, F. Grey, and R. L. Johnson, Physical Review B **44**, 11221 (1991).

[152] J. N. Crain, J. L. McChesney, F. Zheng, M. C. Gallagher, P. C. Snijders, M. Bissen, C. Gundelach, S. C. Erwin, and F. J. Himpsel, Physical Review B **69**, 125401 (2004).

[153] J. Viernow, J.-L. Lin, D. Y. Petrovykh, F. M. Leibsle, F. K. Men, and F. J. Himpsel, Applied Physics Letters **72**, 948 (1998).

[154] T. Ichikawa and S. Ino, Surface Science **105**, 395 (1981).

[155] T. Ichikawa, Surface Science **140**, 37 (1984).

[156] J. M. Carpinelli, H. H. Weitering, M. Bartkowiak, R. Stumpf, and E. W. Plummer, Physical Review Letters **79**, 2859 (1997).

[157] L. Floreano, D. Cvetko, G. Bavdek, M. Benes, and A. Morgante, Physical Review B **64**, 075405 (2001).

[158] H. Morikawa, I. Matsuda, and S. Hasegawa, Physical Review B **65**, 201308 (2002).

[159] A. Goldoni and S. Modesti, Physical Review Letters **79**, 3266 (1997).

[160] T. E. Kidd, T. Miller, and T.-C. Chiang, Physical Review Letters **83**, 2789 (1999).

[161] A. V. Melechko, J. Braun, H. H. Weitering, and E. W. Plummer, Physical Review B **61**, 2235 (2000).

[162] L. Petersen, Ismail, and E. W. Plummer, Physical Review B **65**, 020101 (2001).

[163] J. Avila, A. Mascaraque, E. G. Michel, M. C. Asensio, G. Le Lay, J. Ortega, R. Pérez, and F. Flores, Physical Review Letters **82**, 442 (1999).

[164] R. Pérez, J. Ortega, and F. Flores, Physical Review Letters **86**, 4891 (2001).

[165] M. E. Dávila, J. Avila, M. C. Asensio, and G. Le Lay, Surface Review and Letters **10**, 981 (2003).

[166] F. Ronci, S. Colonna, S. D. Thorpe, A. Cricenti, and G. Le Lay, Physical Review Letters **95**, 156101 (2005).

[167] S. Modesti, L. Petaccia, G. Ceballos, I. Vobornik, G. Panaccione, G. Rossi, L. Ottaviano, R. Larciprete, S. Lizzit, and A. Goldoni, Physical Review Letters **98**, 126401 (2007).

[168] R. Cortés, A. Tejeda, J. Lobo, C. Didiot, B. Kierren, D. Malterre, E. G. Michel, and A. Mascaraque, Physical Review Letters **96**, 126103 (2006).

[169] G. Profeta and E. Tosatti, Physical Review Letters **98**, 086401 (2007).

[170] S. Colonna, F. Ronci, A. Cricenti, and G. Le Lay, Physical Review Letters **101**, 186102 (2008).

[171] H. Morikawa, S. Jeong, and H. W. Yeom, Physical Review B **78**, 245307 (2008).

[172] T. Shirasawa, H. Tochihara, K. Kubo, W. Voegeli, and T. Takahashi, Physical Review B **81**, 081409 (2010).

[173] R. Cortés, A. Tejeda, J. Lobo-Checa, C. Didiot, B. Kierren, D. Malterre, J. Merino, F. Flores, E. G. Michel, and A. Mascaraque, Physical Review B **88**, 125113 (2013).

[174] G. Li, P. Höpfner, J. Schäfer, C. Blumenstein, S. Meyer, A. Bostwick, E. Rotenberg, R. Claessen, and W. Hanke, Nature Communications **4**, (2013).

[175] M. Jäger, C. Brand, A. P. Weber, M. Fanciulli, J. H. Dil, H. Pfnür, and C. Tegenkamp, Physical Review B **98**, 165422 (2018).

[176] J. M. Carpinelli, H. H. Weitering, E. W. Plummer, and R. Stumpf, Nature **381**, 398 (1996).

[177] I. Brihuega, O. Custance, R. Pérez, and J. M. Gómez-Rodríguez, Physical Review Letters **94**, 046101 (2005).

[178] E. Speiser, A. Baumann, S. Chandola, N. Esser, M. Zahedifar, P. Kratzer, and C. Tegenkamp, Physical Review B **98**, 195427 (2018).

[179] T.-L. Chan, C. Z. Wang, M. Hupalo, M. C. Tringides, Z.-Y. Lu, and K. M. Ho, Physical Review B **68**, 045410 (2003).

[180] E. Speiser, N. Esser, S. Wippermann, and W. G. Schmidt, Physical Review B **94**, 075417 (2016).

[181] H. W. Yeom, S. Takeda, E. Rotenberg, I. Matsuda, K. Horikoshi, J. Schaefer, C. M. Lee, S. D. Kevan, T. Ohta, T. Nagao, and S. Hasegawa, Physical Review Letters **82**, 4898 (1999).

[182] W. G. Schmidt, S. Wippermann, S. Sanna, M. Babilon, N. J. Vollmers, and U. Gerstmann, physica status solidi (b) **249**, 343 (2012).

[183] O. Bunk, J. H. Zeysing, G. Falkenberg, R. L. Johnson, M. Nielsen, M. M. Nielsen, and R. Feidenhans'l, Physical Review Letters **83**, 2226 (1999).

[184] A. A. Escuadro, D. M. Goodner, J. S. Okasinski, and M. J. Bedzyk, Physical Review B **70**, 235416 (2004).

[185] J. S. Okasinski, C.-Y. Kim, D. A. Walko, and M. J. Bedzyk, Physical Review B **69**, 041401 (2004).

[186] L. Petaccia, L. Floreano, M. Benes, D. Cvetko, A. Goldoni, L. Grill, A. Morgante, A. Verdini, and S. Modesti, Physical Review B **63**, 115406 (2001).

[187] O. Pulci, M. Marsili, P. Gori, M. Palummo, A. Cricenti, F. Bechstedt, and R. Del Sole, Applied Physics A **85**, 361 (2006).

[188] D. Farías, W. Kamiński, J. Lobo, J. Ortega, E. Hulpke, R. Pérez, F. Flores, and E. G. Michel, Physical Review Letters **91**, 016103 (2003).

[189] F. Ronci, S. Colonna, A. Cricenti, and G. Le Lay, Physical Review Letters **99**, 166103 (2007).

[190] D. Farías, W. Kamiński, J. Lobo, J. Ortega, E. Hulpke, R. Pérez, F. Flores, and E. G. Michel, Applied Surface Science **237**, 86 (2004).

[191] A. Cano, A. P. Levanyuk, and E. G. Michel, Nanotechnology **16**, 325 (2005).

[192] M. Balkanski, R. F. Wallis, and E. Haro, Physical Review B **28**, 1928 (1983).

[193] J. Lobo, D. Farías, E. Hulpke, and E. G. Michel, Physical Review B **71**, 205402 (2005).

[194] L. Petaccia, L. Floreano, A. Goldoni, D. Cvetko, A. Morgante, L. Grill, A. Verdini, G. Comelli, G. Paolucci, and S. Modesti, Physical Review B **64**, 193410 (2001).

[195] J. Ortega, R. Pérez, and F. Flores, Journal of Physics: Condensed Matter **14**, 5979 (2002).

[196] C. J. Buchenauer, M. Cardona, and F. H. Pollak, Physical Review B **3**, 1243 (1971).

[197] K. Conway, J. Macdonald, C. Norris, E. Vlieg, and J. van der Veen, Surface Science **215**, 555 (1989).

[198] C. Törnevik, M. Hammar, N. G. Nilsson, and S. A. Flodström, Physical Review B **44**, 13144 (1991).

[199] D. Wang, N. Esser, M. Cardona, and J. Zegenhagen, Surface Science **343**, 31 (1995).

[200] S. Yi, F. Ming, Y.-T. Huang, T. S. Smith, X. Peng, W. Tu, D. Mulugeta, R. D. Diehl, P. C. Snijders, J.-H. Cho, and H. H. Weitering, Physical Review B **97**, 195402 (2018).

[201] F. Ming, D. Mulugeta, W. Tu, T. S. Smith, P. Vilmercati, G. Lee, Y.-T. Huang, R. D. Diehl, P. C. Snijders, and H. H. Weitering, Nature Communications **8**, (2017).

[202] P. E. J. Eriksson, J. R. Osiecki, K. Sakamoto, and R. I. G. Uhrberg, Physical Review B **81**, 235410 (2010).

[203] J. Menéndez and H. Höchst, Thin Solid Films **111**, 375 (1984).

[204] M. A. Herman and H. Sitter, *Molecular Beam Epitaxy: Fundamentals and Current Status*, 2nd ed. (Springer, Berlin, 1996).

[205] D. R. T. Zahn, K. J. Mackey, R. H. Williams, H. Münder, J. Geurts, and W. Richter, Applied Physics Letters **50**, 742 (1987).

[206] M. Iliev, M. Sinyukov, and M. Cardona, Physical Review B **16**, 5350 (1977).

[207] S. S. Islam, S. Rath, K. P. Jain, S. C. Abbi, C. Julien, and M. Balkanski, Physical Review B **46**, 4982 (1992).

[208] P. Carroll and J. Lannin, Solid State Communications **40**, 81 (1981).

[209] H. R. Chandrasekhar, R. G. Humphreys, U. Zwick, and M. Cardona, Physical Review B **15**, 2177 (1977).

[210] J. Geurts, S. Rau, W. Richter, and F. J. Schmitte, Thin Solid Films **121**, 217 (1984).

[211] J. M. Rowe, Phys. Rev. **163**, 547 (1967).

[212] H. Olijnyk, Physical Review B **46**, 6589 (1992).

[213] H. Richter, Z. Wang, and L. Ley, Solid State Communications **39**, 625 (1981).

[214] I. Campbell and P. Fauchet, Solid State Communications **58**, 739 (1986).

[215] B. P. Falcão, J. P. Leitão, H. Águas, and R. N. Pereira, Physical Review B **98**, 195406 (2018).

[216] D. T. Wang, A. Göbel, J. Zegenhagen, and M. Cardona, Physical Review B **56**, 13167 (1997).

[217] H. D. Fuchs, P. Etchegoin, M. Cardona, K. Itoh, and E. E. Haller, Physical Review Letters **70**, 1715 (1993).

[218] W. Pfeiler, ed., *Alloy Physics* (Wiley-VCH, Weinheim, 2007).

[219] C. Praetorius, *Ce $M_{4,5}$ XAS and XMCD as Local Probes for Kondo and Heavy Fermion Materials: a Study of $CePt_5$/Pt(111) Surface Intermetallics*, Ph.D. thesis, Universität Würzburg (2015).

[220] A. Janghorban, M. Lomello-Tafin, J. Moreau, and P. Galez, Intermetallics **18**, 2208 (2010).

[221] J. Tang, J. M. Lawrence, and J. C. Hemminger, Physical Review B **48**, 15342 (1993).

[222] C. J. Baddeley, A. W. Stephenson, C. Hardacre, M. Tikhov, and R. M. Lambert, Physical Review B **56**, 12589 (1997).

[223] U. Berner and K.-D. Schierbaum, Physical Review B **65**, 235404 (2002).

[224] S. Reimann and H.-J. Schaller, Journal of Alloys and Compounds **419**, 133 (2006).

[225] A. Ramstad and S. Raaen, Physical Review B **59**, 15935 (1999).

[226] A. Ramstad, S. Raaen, and N. Barrett, Surface Science **448**, 179 (2000).

[227] G. Güntherodt, A. Jayaraman, B. Batlogg, M. Croft, and E. Melczer, Physical Review Letters **51**, 2330 (1983).

[228] E. Zirngiebl, B. Hillebrands, S. Blumenröder, G. Güntherodt, M. Loewenhaupt, J. M. Carpenter, K. Winzer, and Z. Fisk, Physical Review B **30**, 4052 (1984).

[229] G. Güntherodt, E. Zirngiebl, S. Blumenröder, A. Jayaraman, B. Batlogg, M. Croft, and E. Melczer, Journal of Magnetism and Magnetic Materials **47**, 315 (1985).

[230] S. L. Cooper, M. V. Klein, Z. Fisk, and J. L. Smith, Physical Review B **34**, 6235 (1986).

[231] R. Hölldobler, *Ramanspektroskopie an Seltenerd-Platin-Verbindungen*, B.Sc. thesis, Universität Leipzig (2015).

[232] B. Halbig, U. Bass, J. Geurts, M. Zinner, and K. Fauth, Physical Review B **95**, 165115 (2017).

[233] M. Zinner, K. Fauth, B. Halbig, U. Bass, and J. Geurts, Materials Research Express **6**, 026416 (2019).

[234] N. Grewe and F. Steglich, in *Handbook on the Physics and Chemistry of Rare Earths*, Vol. 14, edited by K. A. Gschneider, Jr. and L. Eyring (Elsevier, Amsterdam, 1991) Chap. 97, pp. 343–474.

[235] D. Pines, Reports on Progress in Physics **79**, 092501 (2016).

[236] K. Kopitzki and P. Herzog, *Einführung in die Festkörperphysik*, 6th ed. (Vieweg+Teubner, Wiesbaden, 2007).

[237] A. C. Hewson, *The Kondo Problem to Heavy Fermions*, 2nd ed. (Cambridge University Press, Cambridge, U.K., 1993).

[238] S. Doniach, Physica B+C **91**, 231 (1977).

[239] K. S. D. Beach and F. F. Assaad, Physical Review B **77**, 205123 (2008).

[240] M. Klein, A. Nuber, H. Schwab, C. Albers, N. Tobita, M. Higashiguchi, J. Jiang, S. Fukuda, K. Tanaka, K. Shimada, M. Mulazzi, F. F. Assaad, and F. Reinert, Physical Review Letters **106**, 186407 (2011).

[241] C. Praetorius, M. Zinner, A. Köhl, H. Kießling, S. Brück, B. Muenzing, M. Kamp, T. Kachel, F. Choueikani, P. Ohresser, F. Wilhelm, A. Rogalev, and K. Fauth, Physical Review B **92**, 045116 (2015).

[242] C. Praetorius and K. Fauth, Physical Review B **95**, 115113 (2017).

[243] H. Lueken, M. Meier, G. Klessen, W. Bronger, and J. Fleischhauer, Journal of the Less Common Metals **63**, 35 (1979).

[244] C. Praetorius, M. Zinner, P. Hansmann, M. W. Haverkort, and K. Fauth, Physical Review B **93**, 165107 (2016).

[245] B. Predel, in *The Landolt-Börnstein Database*, Vol. 5c, edited by O. Madelung (SpringerMaterials, Berlin, 1993).

[246] C. Praetorius, M. Zinner, G. Held, and K. Fauth, Physical Review B **92**, 195427 (2015).

[247] P. Tereshchuk, M. J. Piotrowski, and J. L. F. Da Silva, RCS Advances **5**, 521 (2015).

[248] J. Kemmer, C. Praetorius, A. Krönlein, P.-J. Hsu, K. Fauth, and M. Bode, Physical Review B **90**, 195401 (2014).

[249] A. P. Murani, Z. A. Bowden, A. D. Taylor, R. Osborn, and W. G. Marshall, Physical Review B **48**, 13981 (1993).

[250] T. Willers, Z. Hu, N. Hollmann, P. O. Korner, J. Gegner, T. Burnus, H. Fujiwara, A. Tanaka, D. Schmitz, H. H. Hsieh, H.-J. Lin, C. T. Chen, E. D. Bauer, J. L. Sarrao, E. Goremychkin, M. Koza, L. H. Tjeng, and A. Severing, Physical Review B **81**, 195114 (2010).

[251] M. Loewenhaupt, U. Witte, S. Kramp, M. Braden, and P. Svoboda, Physica B: Condensed Matter **312-313**, 181 (2002).

[252] R. Schedler, U. Witte, M. Loewenhaupt, and J. Kulda, Physica B: Condensed Matter **335**, 41 (2003).

[253] H.-H. Kung, M. Salehi, I. Boulares, A. F. Kemper, N. Koirala, M. Brahlek, P. Lošťák, C. Uher, R. Merlin, X. Wang, S.-W. Cheong, S. Oh, and G. Blumberg, Physical Review B **95**, 245406 (2017).

[254] J. Zi, H. Büscher, C. Falter, W. Ludwig, K. Zhang, and X. Xie, Applied Physics Letters **69**, 200 (1996).

[255] K. Ahrens and G. Schaack, Physical Review Letters **42**, 1488 (1979).

[256] J. R. Cullen and A. E. Clark, Physical Review B **15**, 4510 (1977).

[257] W. Reichardt and N. Nucker, Journal of Physics F: Metal Physics **14**, L135 (1984).

[258] F. Cerdeira, W. Dreybrodt, and M. Cardona, Solid State Communications **10**, 591 (1972).

Danksagung

An dieser Stelle möchte ich allen danken, die mich während meiner Promotion auf verschiedenste Art und Weise unterstützt haben. Mein ganz besonderer Dank geht hierbei an:

- Prof. Dr. Jean Geurts für die überaus gute Betreuung als Doktorvater. Dies beinhaltet sowohl zahlreiche hilfreiche Erklärungen und Diskussionen bei physikalischen Fragestellungen als auch die Sorge für eine produktive, kollegiale und angenehme Arbeitsumgebung.
- Prof. Dr. Laurens W. Molenkamp für die Aufnahme am Lehrstuhl für Experimentelle Physik III.
- Dr. Utz Bass für die kompetente Unterstützung bei technischen Fragestellungen im Labor, aber auch für geteilte Interessen und Unternehmungen außerhalb der Arbeitszeit.
- die weiteren Mitglieder der Arbeitsgruppe Sebastian Elsässer und Alexander Knapp, sowie an die ehemaligen Mitglieder Dr. Martin Liebhaber und Kim-Mario Wolf, für die gute Zusammenarbeit und gegenseitige Hilfe.
- Rebecca Hölldobler für ihre Mitarbeit in der Arbeitsgruppe im Rahmen ihrer Bachelorarbeit und eines Praktikums. Vielen Dank für die tatkräftige Unterstützung.
- alle Kollegen von der Experimentellen Physik III, insbesondere Carmen Bundschuh, Petra Wolf-Müller, Volkmar Hock und Martin Zipf für ihre technische Hilfe, Lukas Lunczer für die gute Zusammenarbeit bei der Übungsvorbereitung, Angelika Berger für ihre Hilfe bei administrativen Fragen sowie Johannes Brehm, Jan Hajer, Mirko Trabel und Martin Winnerlein. Weiterhin danke ich Dr. Steffen Schreyeck für die Präparation und Überlassung von α-Sn-Proben. Und ebenfalls danke ich Prof. Dr. Karl Brunner und allen anderen Mitspielern (u.a. Peter Pisniak) für viele erfolgreiche Teilnahmen am Volleyballturnier der Fachschaft
- die Kooperationspartner Martin Zinner und PD Dr. Kai Fauth von der Experimentellen Physik II. Insbesondere danke ich Martin Zinner für die Probenpräparation der $CePt_5$/Pt(111)- und $LaPt_5$/Pt(111)-Proben und die intensive Zusammenarbeit (insbesondere auch an langen Messtagen).

- die Kooperationspartner Prof. Dr. Norbert Esser, Dr. Eugen Speiser, Dr. Sandhya Chandola und Julian Plaickner von der Abteilung Nanostrukturen des Leibniz-Instituts für Analytische Wissenschaften - ISAS - e.V. in Berlin. Besonders bedanke ich mich für die Ermöglichung eines Forschungsaufenthalts am ISAS-Institut und die damit verbundenen Erfahrungen.

- den Kooperationspartner Prof. Dr. Simone Sanna vom Institut für Theoretische Physik der Justus-Liebig-Universität Gießen für die durchgeführten Berechnungen und die intensiven Diskussionen der theoretischen und experimentellen Ergebnisse. Ebenfalls bedanke ich mich bei Prof. Dr. Wolf Gero Schmidt und Sergej Neufeld vom Department Physik der Universität Paderborn.

- die Mitarbeiter der wissenschaftlichen Werkstatt für Reparaturen und Neuanfertigungen, insbesondere an Dr. Utz Bass, Rainer Brauner, Peter Pisniak und Thomas Grünebaum. Ebenfalls danke ich Roland Ebert und Cornelius Ziga von der Tieftemperaturtechnik.

- Sabine Stahl, Prof. Dr. Karl Brunner und Prof. Dr. Dr. h.c. Wolfgang Kiefer für die leihweise Überlassung von Laborkomponenten und -ausstattung.

- die Diskussionsrunde mit Holger Suchomel, Andreas Hausoel und Christoph Wick, in der nicht nur wissenschaftliche Fragen Thema waren.

- meine Familie, meine Freunde und besonders an Eve für die Unterstützung während der Anfertigung dieser Arbeit.

Finanzielle Unterstützung bei der Durchführung der Experimente wurde von der Deutschen Forschungsgemeinschaft im Rahmen der Forschergruppe FOR1162 (Projekte Ge1855/10-1 und Ge1855/10-2) zur Verfügung gestellt.